学位論文

Small-scale density perturbations as a probe of the nature of dark matter

(小スケール密度揺らぎで探る暗黒物質の性質)

平成25年12月博士（理学）申請

東京大学大学院理学系研究科物理学専攻

鎌田　歩樹

Small-scale density perturbations as a probe of the nature of dark matter

by

Ayuki Kamada

A Thesis Presented
in Partial Fulfillment of the Requirements
for the Degree of
Doctor of Philosophy in Science

Department of Physics, The University of Tokyo

December 2013

Abstract

The existence of dark matter in the Universe has been established by numerous cosmological and astrophysical observations on a wide range of scales. Its nature, however, has remained unknown for almost eighty years since its first postulation, and hence, the identification of dark matter is arguably the most important challenge in cosmology, astrophysics, and particle physics.

We investigate imprints of dark matter properties on small-scale density perturbations. Although cold dark matter (CDM) model is currently popular, particle physics candidates of dark matter are not completely cold and dark. In the structure formation with realistic candidates, the large-scale density perturbations are almost the same with CDM, but small-scale ones are not. Therefore, the deviation in the matter power spectra from CDM contains information of properties of dark matter.

Not only does the imprint on the matter power spectrum give us valuable information about the nature of dark matter, but also it may resolve the problems in the formation of small-scale structure (SSS) in ΛCDM model ("small scale crisis"). The hierarchical structure formation in ΛCDM model predicts an order of hundred gravitationally-bounded objects in Milky Way-sized halos, while only a few tens of satellite galaxies are observed in Milky Way. This mismatch is called "missing satellite problem" and is an example of "small scale crisis". One possible solution to "small scale crisis" is warm dark matter (WDM). The thermal velocity of WDM behaves like effective "pressure" of dark matter fluid and suppresses the gravitational growth of small-scale matter density fluctuations. Several WDM candidates are suggested in the well-motivated particle physics models (e.g. light gravitino, sterile neutrino). In these models, the WDM particles are produced in different ways. On the other hand, the astrophysical/cosmological constraints (e.g. by the Lyα absorption lines in emission spectra from high-redshift quasars) on WDM is usually reported in terms of the light gravitino mass. It should be clarified how the WDM matter power spectra in different WDM models can be related. To this end, we introduced two quantities, the fraction of warm dark matter $r_{\rm warm}$ and the Jeans scale at the matter-radiation equality $k_{\rm J}$. We follow the time evolution of density perturbations in WDM models. From the simulation results, we confirm that the halo and the subhalo abundances and the radial distributions of subhalos are indeed similar between the different WDM models. The radial distribution of subhalos in Milky Way-size halos is consistent with the observed distribution for $k_{\rm J} \sim 20 - 260\,h\,{\rm Mpc}^{-1}$; such models resolve the so-called "missing satellite problem".

We also study how "warm" the wino dark matter is when it is non-thermally produced by the decays of the gravitino in the early Universe. The wino, which is the supersymmetric partner of the weak boson, is well-motivated candidate of dark matter after the discovery of the Higgs boson with a mass around 126 GeV. The "warmness" of the wino dark matter leaves imprints on the matter power spectra and may provide further insights on the origin of dark matter via the future 21 cm line survey. In addition, we perform similar analysis to the bino-wino co-annihilation scenario in high-scale supersymmetry breaking models. Although the collider experiment can not search the bino dark matter directly, the imprints on the matter power spectra can be a direct probe.

Finally, we explore the discovery potential of light gravitino mass $m_{3/2}$ by combining future cosmology surveys and collider experiments. The gravitino mass is one of the fundamental parameters in SUSY theory that is directly related to the SUSY breaking energy scale. We focus on the gauge-mediated supersymmetry breaking model that generically predicts the existence of light gravitinos with $m_{3/2} \sim$ eV-keV. We show that the light gravitino mass can be determined with an accuracy of $m_{3/2} = 4 \pm 1\,\mathrm{eV}$ by a combination of the Hyper Suprime Cam survey and cosmic microwave background anisotropy data obtained by Planck satellite. Data from experiments at Large Hadron Collider at 14 TeV will provide constraint at $m_{3/2} \simeq 5\,\mathrm{eV}$ in the minimal framework of gauge-mediated supersymmetry breaking (GMSB) model. We conclude that a large class of the GMSB model can be tested by combining the cosmological observations and the collider experiments.

Contents

List of Figures

Chapter 1

Introduction

The existence of dark matter in the Universe has been established by numerous cosmological and astrophysical observations on a wide range of scales. Its nature, however, has remained unknown for almost eighty years since its first postulation, and hence, the identification of dark matter is arguably the most important challenge in cosmology, astrophysics, and particle physics [4, 5]. In particular, recent observations of the cosmic microwave background anisotropy [6, 7] determine the relic density of dark matter almost at the several percent level,

$$\Omega_{\rm dm} h^2 \simeq 0.12\,. \tag{1.1}$$

Although we know little of the origin of dark matter, we are (almost) certain that dark matter is not a part of the standard model. One of noteworthy properties of DM particle is the long lifetime. A lifetime of DM should be comparable or beyond the age of the Universe ($t_0 \simeq 13.7 \times 10^9\,{\rm yr}$), while the typical lifetime $\tau_{\rm DM}$ of a particle with a mass $m_{\rm DM}\,(\sim 100\,{\rm GeV})$ via an exchange of a heavy particle with a mass $m_{\rm ex}\,(\sim 1\,{\rm TeV})$, and a coupling with a coupling constant λ is much shorter,

$$\tau_{\rm DM} \sim 2 \times 10^{-34}\,{\rm yr} \times \left(\frac{0.1}{\lambda}\right)^4 \left(\frac{100\,{\rm GeV}}{m_{\rm DM}}\right)^5 \left(\frac{m_{\rm ex}}{1\,{\rm TeV}}\right)^4 . \tag{1.2}$$

Another important property of DM particle is the present energy density (abundance), which is severely constrained by recent astronomical measurements such as precise measurements of the cosmic microwave background anisotropy. The production mechanisms are different between the two classes; [1]

class. 1 Interactions between WIMP DM and SM particles are efficient when the reheating of the Universe ends . Then, as the Universe cools down, DM particles become non-relativistic and the inverse annihilation process of DM particles become suppressed by the Boltzmann factor. The annihilation process reduces the number density, but stops at some temperature at which DM particles cannot find each other to annihilate. The relic abundance of WIMP DM is proportional to the annihilation cross section $\langle \sigma_{\rm ann} v \rangle$,

$$\Omega_{\rm WIMP} h^2 \simeq 0.1 \times \left(\frac{3 \times 10^{-26}\,{\rm cm^3\,s^{-1}}}{\langle \sigma_{\rm ann} v \rangle}\right) . \tag{1.3}$$

The canonical value of annihilation cross section $\langle \sigma_{\rm ann,\,can} v \rangle = 3 \times 10^{-26}\,{\rm cm^3\,s^{-1}} (\simeq 3 \times 10^{-9}\,{\rm GeV^{-2}})$ is almost the same as the annihilation cross section of DM particles with a mass of the electroweak

[1] This classification is very rough. In general, production mechanism differs for each model.

scale through the weak interaction. The so-called "WIMP-miracle" makes WIMP a well-motivated DM candidate.

class. 2a DM particles are produced in the thermal background and thermairized in the early Universe. The super-weak interaction decouples DM from the thermal background when DM is relativistic like SM neutrino.

class. 2b DM particles do not enter into the equilibrium with SM particles since only super-weak interactions are available. Therefore, DM particles are produced via non-thermal processes (decay, inelastic scattering, ...). In the case of a non-thermal inelastic scattering, the resultant density is proportional to the inelastic scattering cross section, the DM mass and the reheating temperature of the Universe,

$$\Omega_{\rm NT}h^2 \simeq 0.06 \times \left(\frac{\langle\sigma_{\rm ine}v\rangle}{10^{-47}\,{\rm cm}^3\,{\rm s}^{-1}}\right)\left(\frac{m_{\rm DM}}{\rm keV}\right)\left(\frac{T_{\rm R}}{10^{12}\,{\rm GeV}}\right) . \tag{1.4}$$

class. 2c Scalar particles, such as modulus and QCD axions, can form a homogeneous condensate (or, field) $\phi(t)$. If the scalar filed takes a value displaced from the minimum of the potential at $H \simeq m_\phi$, where m_ϕ is the mass of the scalar particle and H is the Hubble parameter, the scalar begins to oscillate coherently and the energy density of the scalar field can scales as $\rho_\phi \propto a^{-3}$ for the scale factor a like a matter energy density. The present energy density is proportional to the mass of the scalar field and the initial amplitude of the scalar filed at $H \simeq m_\phi$,

$$\Omega_\phi h^2 \simeq 0.6 \times \left(\frac{m_\phi}{\rm keV}\right)^{1/2}\left(\frac{\phi_0}{10^{11}\,{\rm GeV}}\right)^2\left(\frac{g_*}{100}\right)^{-1/4} . \tag{1.5}$$

As the relic abundance of DM, the search strategy of DM depends on the strength of interactions between DM and SM particles. Therefore, the method of DM search differs between the two classes;

class. 1 Weak interaction with SM particles makes WIMP subject to the underground direct direction experiments. The annihilation of WIPMs in the galactic center and the dwarf spheroidal yield high-energy cosmic rays. The indirect signals may exceed the astrophysical backgrounds. The electroweak scale mass of WIMP allow even terrestrial colliders to produce DM particles, which can be detected as missing energies.

class. 2 Super-weak interaction with SM particles make it very challenging to detect DM signals in the direct detection experiments. In the same way, terrestrial collider experiments are not promising. The almost only way is to detect the signals of rare DM reactions in the astrophysical objects. The rich abundance of DM can compensate the small reaction rate to leave distinguishable indirect signals.

In Table 1.1, we summarize this section. WIMP (class. 1) is a well-motivated candidate and a main target of the on-going DM searches. On the other hand, for super-weakly interacting DM candidates, we have a chance to hunt DM signals only in the indirect searches in the astronomical observations.

Therefore, it is highly motivated to relate the identity of dark matter with physics beyond the standard model [8]. In particular, the supersymmetric standard model [9, 10, 11] is one of the most viable candidates of new physics which contains a good candidate for dark matter, i.e. LSP. Supersymmetry (SUSY) is attractive since it allows the vast separation of low energy scales from

class	example	interaction	production	direct	indirect	collider
1	(LSP, LKP) WIMP	weak	thermal	◯	◯	◯
2a	gravitino	super-weak	thermal	×	◯	×
2b	sterile neutrino	super-weak	non-thermal	×	◯	×
2c	moduli, QCD axion	super-weak	coherent oscillation	×	◯	×

Table 1.1: Rough classification of DM candidates and prospect of DM searches

high energy scales such as the Planck scale or the scale of GUT. The supersymmetric standard model is also supported by the precise unification of three gauge coupling constants of the standard model at the GUT scale.

Cold dark matter model with cosmological constant (ΛCDM model) is in excellent agreement with observations of large scale structure (LSS) of the Universe. (e.g. cosmic microwave background (CMB) anisotropy measurement, cluster/galaxy survey [12, 13, 14]). The recent CMB anisotropy measurement by the Planck satellite determines the ΛCDM model parameters at the level of several percent. CDM is a hypothetical particle that does not have any thermal velocity or interaction except for the gravitational interaction. On the other hand, particle physics candidates of dark matter may have finite thermal velocity and interactions. The deviation from CDM leaves its imprints on density perturbations at small-scales. In the followings, we investigated the small-scale imprints considering some relaistc particle physics models.

The rest of the thesis is organised as follows. In Chapter 2, we summarize the evolution equations of the structure of the Universe. In Chapter 3, we studied the structure formation in warm dark matter models and in models with long-lived charged massive particles. We follow the evolution of the density perturbations both in the linear regime and in the nonlinear regime. We compare the radial distributions of subhalos in simulated Milky Way-size halos with the observed distribution. This part is based on our published paper [15]. In Chapter 4, we study how "warm" the wino dark matter is when it is non-thermally produced by the decays of the gravitino in the early Universe. We clarify the energy distribution of the wino at the decay of the gravitino and the energy loss process after their production. This part is based on our published paper [16]. In Chapter 5, we describe phenomenological aspects of the bino-wino co-annihilation scenario in high-scale supersymmetry breaking models. We study imprints on the small-scale matter power spectrum when the bino dark matter is produced by the decay of the gravitino. This part is based on our published paper [17]. In Chapter 6, we explore the discovery potential of light gravitino mass $m_{3/2}$ by combining future cosmology surveys and collider experiments. This part is based on our published paper [18]. Finally, Chapter 7 is devoted to the concluding remarks.

Chapter 2

Evolution of the structure of the Universe

In this chapter we summarize the basic formulas of modern cosmology. We start with the Einstein equations and the Boltzmann equations. Finally we derive the evolution equations of background and perturbed distribution functions of collision less particle. The derived formulas are applied to realistic dark matter models and solved numerically in subsequent chapters.

2.1 Mutual evolution of the spacetime and the matter and energy of the Universe

2.1.1 Basics of the general relativity

The coordinate distance dx^μ ($x^\mu = (t, x^i)$, $\mu = 0, 1, 2, 3$, $i = 1, 2, 3$) and the line element ds are related by the metric $g_{\mu\nu}(x)$ such that

$$ds^2 = g_{\mu\nu}(x) dx^\mu dx^\nu \,. \tag{2.1}$$

The metric also characterizes the local geometry of spacetime. The curvature of the spacetime is equivalent to the gravity. In a curved spacetime, the equation of motion for a free falling test particle is modified from the Newton's law $d^2x^i/dt^2 = 0$. It follows the so-called geodesic equation,

$$\frac{d^2x^\mu}{d\lambda^2} + \Gamma^\mu_{\ \nu\lambda} \frac{dx^\nu}{d\lambda} \frac{dx^\lambda}{d\lambda} = 0 \,, \tag{2.2}$$

with the affine parameter λ and the affine connection

$$\Gamma^\mu_{\ \nu\lambda} = \frac{1}{2} g^{\mu\kappa} \left[\frac{\partial g_{\nu\kappa}}{\partial x^\lambda} + \frac{\partial g_{\kappa\lambda}}{\partial x^\nu} - \frac{\partial g_{\nu\lambda}}{\partial x^\kappa} \right] . \tag{2.3}$$

It should be noted that the Newton's law is recovered in the Minkowsky spacetime,

$$g_{\mu\nu}(x) = \eta_{\mu\nu} \equiv \mathrm{diag}[-1, 1, 1, 1] \,. \tag{2.4}$$

Moreover, the Mach's principle ensures that we can take a frame where the test particle motion can be described by the Newton's law in the vicinity of some spacetime point P, i.e. $g_{\mu\nu}(\mathrm{P}) = \eta_{\mu\nu}$ and $\Gamma^\mu_{\ \nu\lambda}(\mathrm{P}) = 0$. Such a frame is called the local inertia frame. This is why the curvature of spacetime does not affect the terrestrial experiments.

The Einstein's equation describes the time evolution of the metric with the matter and energy,

$$G_{\mu\nu} = 8\pi G\, T_{\mu\nu} \tag{2.5}$$

with the Newton's gravitational constant G. The Einstein tensor $G_{\mu\nu}$ is a divergenceless linear combination of the Ricci tensor $R_{\mu\nu}$ and the Ricci scholar $R(= g^{\mu\nu}R_{\mu\nu})$, $G_{\mu\nu} = R_{\mu\nu} - 1/2 g_{\mu\nu}R$ and $\nabla_\nu G^{\mu\nu} = 0$ where ∇_μ denotes the covariant derivative with respect to x^μ. The Ricci tensor $R_{\mu\nu}$ is defined by $R_{\mu\nu} = R^\lambda{}_{\mu\lambda\nu}$ with the Riemann curvature tensor $R^\mu{}_{\nu\lambda\kappa}$. The Riemann curvature tensor involves (up to second order) time derivatives of the metric $g_{\mu\nu}$,

$$R^\mu{}_{\nu\lambda\kappa} = \frac{\partial \Gamma^\mu{}_{\nu\kappa}}{\partial x^\lambda} - \frac{\partial \Gamma^\mu{}_{\nu\lambda}}{\partial x^\kappa} + \Gamma^\mu{}_{\rho\lambda}\Gamma^\rho{}_{\nu\kappa} - \Gamma^\mu{}_{\rho\kappa}\Gamma^\rho{}_{\nu\lambda}\,. \tag{2.6}$$

The matter and energy couples with the gravity only through the energy-momentum tensor $T_{\mu\nu}$. The energy-momentum tensor is defined by the variation of the matter and energy action S_m with respect to the metric,

$$\delta S_m = \frac{1}{2}\int d^4x\,(-g)^{1/2}\,\delta g_{\mu\nu}T^{\mu\nu}\,, \tag{2.7}$$

where g is the determinant of the metric. The conservation of the energy momentum tensor $\nabla_\nu T^{\mu\nu} = 0$ does not generically describe the evolution of all the (10) components of the energy-momentum tensor. In order to obtain a closed form of evolution equation, we should specify the matter and energy contents of the Universe.

2.1.2 General relativistic Boltzmann equation

In the general relativity, the one particle action is called the world-line action. It takes a form of

$$S = -m\int d\lambda\,\frac{d\tau}{d\lambda}\,, \tag{2.8}$$

where τ is the proper time, $d\tau = \sqrt{-g_{\mu\nu}dx^\mu dx^\nu}$. The variation of the world-line action with respect to $x^\mu(\lambda)$ leads to the geodesic equation (Eq. (2.2)). The geodesic equation conserves the proper time $d\tau/d\lambda = \text{const}$. This allows us to set the affine parameter such that $P^\mu = dx^\mu/d\lambda$ where P_μ is the canonical momentum, $P^2 = P_\mu P_\mu = -m^2$. The energy-momentum tensor can be evaluated as,

$$\begin{aligned}
T^{\mu\nu} &= \frac{1}{(-g)^{1/2}}\int d\lambda\,\delta^4(x^\mu - x^\mu(\lambda))P^\mu P^\nu && (2.9)\\
&= \frac{1}{(-g)^{1/2}}\delta^3(x^i - x^i(t))\frac{P^\mu P^\nu}{P^0} && (2.10)\\
&= \int \frac{d^3P_k}{(2\pi)^3P^0}\,(-g)^{-1/2}\,P^\mu P^\nu\left[\delta^3(x^i - x^i(t))\,(2\pi)^3\delta^3(P_j - P_j(t))\right]\,. && (2.11)
\end{aligned}$$

This can be easily generalised to the ensemble average (denoted by the angle brackets $\langle\rangle_{\rm en}$) of a many body system with N particles (labeled by $r = 1, \ldots, N$),

$$\begin{aligned}
T^{\mu\nu} &= \sum_{r=1}^{N}\int \frac{d^3P_k}{(2\pi)^3P^0}\,(-g)^{-1/2}\,P^\mu P^\nu\langle\delta^3(x^i - x_r^i(t))\,(2\pi)^3\delta^3(P_j - P_{r\,j}(t))\rangle_{\rm en} && (2.12)\\
&= \int \frac{d^3P_k}{(2\pi)^3P^0}\,(-g)^{-1/2}f(x^i, P_j, t)P^\mu P^\nu\,. && (2.13)
\end{aligned}$$

In the second line, we introduce the phase-space distribution $f(x^i, P_j, t) = \sum_{r=1}^{N} \langle \delta^3(x^i - x_r^i(t))\, (2\pi)^3 \delta^3(P_j - P_{r\,j}(t)) \rangle_{\rm en}$. The phase-space distribution is a scalar under a coordinate transformation. This can be seen manifestly in the following way,

$$\delta(P^2 + m^2) f(x^i, P_j, t) \tag{2.14}$$

$$= \delta(P^2 + m^2) \int d\lambda \sum_{r=1}^{N} \langle \delta^4(x^\mu - x^\mu(\lambda))\, P^0 (2\pi)^3 \delta^3(P_j - P_{r\,j}) \rangle_{\rm en} \tag{2.15}$$

$$= \frac{(2\pi)^3}{2} \int d\lambda \sum_{r=1}^{N} \langle \delta^4(x^\mu - x^\mu(\lambda))\, \delta^4(P_\mu - P_{r\,\mu}) \rangle_{\rm en}\,, \tag{2.16}$$

where λ is the affine parameter. From the above discussions, we can find that the evolution of the phase-space distribution of a free falling particle is governed by the Boltzmann equation,

$$\frac{D}{D\lambda} f = \frac{dx^\mu}{d\lambda} \frac{\partial}{\partial x^\mu} f + \frac{dP^\mu}{d\lambda} \frac{\partial}{\partial P^\mu} f = 0\,, \tag{2.17}$$

$$\frac{dx^\mu}{d\lambda} = P^\mu\,, \tag{2.18}$$

$$\frac{dP^\mu}{d\lambda} = -\Gamma^\mu{}_{\nu\lambda} P^\nu P^\lambda\,. \tag{2.19}$$

In the third line, we have used the geodesic equation (Eq. (2.2)).

2.1.3 Expansion of the Universe

The modern cosmology is based on the assumption that there is no special point or direction in the global structure of the Universe, i.e. the Universe is homogeneous and isotropic after smoothing out individual stars, galaxies, and clusters. The unique choice of the metric (up to a coordinate transformation) is called the Robertson-Walker metric,

$$ds^2 = -dt^2 + a^2(t) \left[dx^i dx^i + K \frac{(x^i dx^i)^2}{1 - K x^i x^i} \right] \tag{2.20}$$

where $a(t)$ is called the scale factor and $K = 0, \pm 1$ is the spatial curvature. Hereafter, we consider only the case of zero spacial curvature $K = 0$ (the spatially flat Universe), which is favored by the recent data from the cosmic microwave background anisotropies [6, 7]. We also take the conformal time τ that is defined by $d\tau = dt/a(t)$. The Robertson-Walker metric is now written by

$$ds^2 = a^2(\tau) \left[-d\tau^2 + dx^i dx^i \right]\,. \tag{2.21}$$

In the homogeneous and isotropic Universe, the energy-momentum tensor is restricted to the one of the perfect fluid,

$$T^{\mu\nu} = P g^{\mu\nu} + (\rho + P) u^\mu u^\nu\,, \tag{2.22}$$

where ρ and P denote the energy density and the pressure of the perfect fluid, respectively. We define the fluid velocity u^μ in the same way as in Ref. [19],

$$u^2 = u^\mu u_\mu = -1\,, \tag{2.23}$$

$$u_\nu T^{\mu\nu} = -\rho u^\mu\,. \tag{2.24}$$

In the homogeneous and isotropic Universe, $u^\mu = (1/a, 0, 0, 0)$. From the energy-momentum conservation, we obtain a evolution equation of the energy density,

$$\dot{\rho} = 3\frac{\dot{a}}{a}(\rho + P)\,, \tag{2.25}$$

where the dots denote derivative with respect to τ. By substituting Eq. (2.21) and Eq. (2.22) to the Einstein's equation (Eq. (2.5)), we obtain two independent equations,

$$\left(\frac{\dot{a}}{a}\right)^2 = \frac{8\pi G}{3}a^2\rho\,, \tag{2.26}$$

$$\frac{d}{d\tau}\left(\frac{\dot{a}}{a}\right) = -\frac{4\pi G}{3}a^2\left(\rho + 3P\right)\,. \tag{2.27}$$

The first equation governs the expansion of the Universe and the second determines acceleration/deceleration of the Universe. The above evolution equations do not from a closed set. To this end, we should specify an equation of state of the matter and energy $P = w\rho$. For a given w, the scale factor dependence of the energy density is $\rho \propto a^{-3(1+w)}$.

The homogeneity and isotropy implies that the phase-space distribution depends only on $\sqrt{P_iP_i}$ and τ, $f(x^i, P_j, \tau) = f(\sqrt{P_iP_i}, \tau)$ The geodesic equation (Eq. (2.2)) leads to the evolution equation of $d(\sqrt{P_iP_i})/d\tau = 0$. The canonical momentum is constant and thus it is often refereed to the comoving momentum q,

$$\frac{d}{d\tau}q = 0 \tag{2.28}$$

The proper momentum $p = \sqrt{g^{ij}P_iP_j}$ scales inverse-proportionally to the scale factor, $p = q/a$. The Boltzmann equation (Eq. (2.17)) takes a form of

$$\frac{\partial}{\partial\tau}f(q,\tau) = 0\,. \tag{2.29}$$

Therefore, the comoving momentum distribution is conserved. [1] The energy-momentum tensor (Eq. (2.13)) can be evaluated,

$$\rho = -T^0{}_0 = a^{-4}\int\frac{4\pi q^2 dq}{(2\pi)^3}\,\epsilon\, f(q,\tau)\,, \tag{2.33}$$

$$P = 3T^i{}_i = a^{-4}\int\frac{4\pi q^2 dq}{(2\pi)^3}\,\frac{q^2}{\epsilon}\,f(q,\tau)\,, \tag{2.34}$$

[1] For example, if free falling particles with g_s internal degrees of freedom follow the thermal distribution at the beginning $\tau = \tau_i$,

$$f(q,\tau_i) = g_s\left[\exp\left\{(\sqrt{p^2(\tau_i)+m^2} - \mu)/T\right\} \mp 1\right]^{-1} \tag{2.30}$$

$$= g_s\left[\exp\left\{(\sqrt{q^2+a^2(\tau_i)m^2} - a(\tau_i)\mu)/a(\tau_i)T\right\} \mp 1\right]^{-1}\,, \tag{2.31}$$

then at any time τ the distribution function is given by

$$f(q,\tau) = g_s\left[\exp\left(\frac{\sqrt{p^2(\tau)+(a(\tau_i)/a(\tau))^2m^2} - (a(\tau_i)/a(\tau))\mu}{(a(\tau_i)/a(\tau))T}\right) \mp 1\right]^{-1}\,. \tag{2.32}$$

Here, signs $-$ and $+$ correspond to the Bose-Einstein distribution and the Fermi-Dirac distribution, respectively. We can see that the mass m, chemical potential μ, and temperature T effectively scale inverse-proportionally to the scale factor, $m, \mu, T \propto 1/a$.

with the comoving energy $\epsilon = \sqrt{q^2 + a^2 m^2}$. The evolution equation of the energy density (Eq. (2.25)) follows from

$$\frac{d}{d\tau}\left(\frac{\epsilon}{a^4}\right) = -\left(\frac{\dot{a}}{a}\right)\left(3\frac{\epsilon}{a^4} + \frac{q^2}{a^4}\right) . \tag{2.35}$$

If the particles are relativistic (non-relativistic), the equation of state is given by $w = 1/3$ ($w = 0$). From the evolution equation of the energy density, the energy density decreases as $\rho \propto a^{-4}$ (a^{-3}).

2.1.4 Evolution of cosmological perturbations (general formulation)

Even if the global structure of the Universe is homogeneous and isotropic, local structures of the Universe are not homogeneous or isotropic. There are many small/large-scale structures such as stars, galaxies, and clusters. In the current understanding, these structures are formed through the evolution of small primordial perturbations e.g. produced during inflation. In order to take into account cosmological perturbations, we expand physical quantities Qs such that $Q = \bar{Q} + \delta Q$ where $\bar{Q}$ is a homogeneous and isotropic background and δQ is a small perturbation. Since the background does not break the spatial isometry invariance, perturbations can be decomposed into Fourier and spin components [20].

We expand the metric such that

$$g_{\mu\nu} = a^2(\tau)\left[\eta_{\mu\nu} + h_{\mu\nu}(x^i, \tau)\right] . \tag{2.36}$$

The small perturbation $h_{\mu\nu}(x^i, \tau)$ consists of 4 scalar, 4 vector, and 2 tensor degrees of freedom. On the other hand, a coordinate transformation has 2 scalar and 2 vector degrees of freedom. Therefore, 2 scalar, 2 vector and 2 tensor degrees of freedom are physical. It should be noted that only gauge invariant quantities (e.g. Bardeen potential [21] and Mukhanov-Sasaki variable [22, 23]) are observable. Hereafter we focus on scalar degrees of freedom and adopt two popular gauge fixings, the synchronous gauge [24] and the conformal Newtonian gauge [25]. The metric now takes a form of [2]

— *Synchronous gauge* —

$$ds^2 = a^2(\tau)\left[-d\tau^2 + (\delta_{ij} + h_{ij})dx^i dx^j\right] . \tag{2.37}$$

— *Conformal Newtonian gauge* —

$$ds^2 = a^2(\tau)\left[-(1+2\psi)d\tau^2 + (1-2\phi)dx^i dx^j\right] . \tag{2.38}$$

Here, h_{ij} is defined by

$$h_{ij}(k_l, \tau) = \frac{1}{3}\delta_{ij} h(k_l, \tau) + \left(\hat{k}_i\hat{k}_j - \frac{1}{3}\delta_{ij}\right)\left(h(k_l, \tau) + 6\eta(k_l, \tau)\right) \tag{2.39}$$

in the Fourier space ($k_i = k\hat{k}_i,\ \hat{k}_i\hat{k}_i = 1$). The metrics are related such that [26]

$$\psi(k_i, \tau) = \frac{1}{2k^2}\left\{\ddot{h}(k_i, \tau) + 6\ddot{\eta}(k_i, \tau) + \frac{\dot{a}}{a}\left[\dot{h}(k_i, \tau) + 6\dot{\eta}(k_i, \tau)\right]\right\} , \tag{2.40}$$

$$\phi(k_i, \tau) = \eta(k_i, \tau) - \frac{1}{2k^2}\frac{\dot{a}}{a}\left[\dot{h}(k_i, \tau) + 6\dot{\eta}(k_i, \tau)\right] . \tag{2.41}$$

[2] Here, we define the Kronecker delta δ_{ij} such that $\delta_{ij}dx^i dx^j = dx^i dx^i$

through the coordinate transformation of

$$x^\mu(\mathrm{Con}) = x^\mu(\mathrm{Syn}) - \xi^\mu(x)\,, \tag{2.42}$$

$$\xi^0(k_i,\tau) = \frac{1}{2k^2}\left[\dot{h}(k_i,\tau) + 6\dot{\eta}(k_i,\tau)\right]\,, \tag{2.43}$$

$$\xi^i(k_i,\tau) = i\hat{k}_i\frac{1}{2k}\left[h(k_i,\tau) + 6\eta(k_i,\tau)\right]\,. \tag{2.44}$$

Here "Con" and "Syn" represent the conformal newtonian gauge and the synchronous gauge, respectively.

The perturbed energy-momentum tensor can be written by $T^{\mu\nu} = \bar{T}^{\mu\nu} + \delta T^{\mu\nu}$, where $\bar{T}^{\mu\nu} = \bar{P}\bar{g}^{\mu\nu} + (\bar{\rho}+\bar{P})\bar{u}^\mu\bar{u}^\nu$ is the same as in Eq. (2.22). Here the fluid velocity is also perturbed, $u^\mu = \bar{u}^\mu + \delta u^\mu$. The normalization condition $u^\mu u_\mu = -1$ requires $h_{\mu\nu}\bar{u}^\mu\bar{u}^\nu + 2\bar{g}_{\mu\nu}\bar{u}^\mu\delta u^\nu = 0$, i.e. $\delta u^0 = -h_{00}/2a$. We decompose $\delta T^{\mu\nu}$ into perturbations to the perfect fluid and the other,

$$\delta T^{\mu\nu} = \delta P\bar{g}^{\mu\nu} + \bar{P}a^2h^{\mu\nu} + (\delta\rho+\delta P)\bar{u}^\mu\bar{u}^\nu + (\bar{\rho}+\bar{P})(\delta u^\mu\bar{u}^\nu + \bar{u}^\mu\delta u^\nu) + \Sigma^{\mu\nu} \tag{2.45}$$

where the imperfect fluid perturbation $\Sigma^{\mu\nu}$ is traceless $\bar{g}_{\mu\nu}\Sigma^{\mu\nu} = 0$. The energy flow condition $u_\nu T^{\mu\nu} = -\rho u^\mu$ requires $\bar{u}_\nu\Sigma^{\mu\nu} = 0$. This implies that only the spatial component is non-zero $\Sigma^{ij} \neq 0$, but it is traceless $\delta_{ij}\Sigma^{ij} = 0$. By introducing the density perturbation δ, the divergence of the fluid velocity θ, and the anisotropic stress perturbation σ, we summarize the above discussion about the perturbed energy-momentum tensor in the Fourier space,

$$\bar{\rho}\,\delta = \delta\rho = -\delta T^0_{\ 0}\,, \tag{2.46}$$

$$(\bar{\rho}+\bar{P})\theta = (\bar{\rho}+\bar{P})ik_ia\delta u^i = ik_i\delta T^0_{\ i}\,, \tag{2.47}$$

$$\delta P = \frac{1}{3}\delta T^i_{\ i}\,, \tag{2.48}$$

$$(\bar{\rho}+\bar{P})\sigma = -(\bar{\rho}+\bar{P})\hat{k}_i\hat{k}_j\Sigma^i_{\ j} = -\left(\hat{k}_i\hat{k}_j - \frac{1}{3}\delta_{ij}\right)\delta T^i_{\ j}\,. \tag{2.49}$$

The above variables are gauge dependent. Through the gauge transformation of Eq. (2.42), they are related as

$$\delta(\mathrm{Syn}) = \delta(\mathrm{Con}) - \alpha\,\dot{\rho}/\bar{\rho}\,, \tag{2.50}$$

$$\theta(\mathrm{Syn}) = \theta(\mathrm{Con}) - \alpha k^2\,, \tag{2.51}$$

$$P(\mathrm{Syn}) = P(\mathrm{Con}) - \alpha\,\dot{P}\,, \tag{2.52}$$

$$\sigma(\mathrm{Syn}) = \sigma(\mathrm{Con})\,, \tag{2.53}$$

with $\alpha = (\dot{h}+6\dot{\eta})/2k^2$.

The energy-momentum conservation leads to

— *Synchronous gauge* —

$$\dot{\delta} = -(1+w)\left(\theta + \frac{1}{2}\dot{h}\right) - 3\frac{\dot{a}}{a}\left(\frac{\delta P}{\delta\rho} - w\right)\delta\,, \tag{2.54}$$

$$\dot{\theta} = -\frac{\dot{a}}{a}(1-3w)\theta - \frac{\dot{w}}{1+w}\theta + \frac{\delta P/\delta\rho}{1+w}k^2\delta - k^2\sigma\,. \tag{2.55}$$

— *Conformal Newtonian gauge* —

$$\dot{\delta} = -(1+w)\left(\theta - 3\dot{\phi}\right) - 3\frac{\dot{a}}{a}\left(\frac{\delta P}{\delta\rho} - w\right)\delta\,, \tag{2.56}$$

$$\dot{\theta} = -\frac{\dot{a}}{a}(1-3w)\theta - \frac{\dot{w}}{1+w}\theta + \frac{\delta P/\delta\rho}{1+w}k^2\delta - k^2\sigma + k^2\psi\,. \tag{2.57}$$

The first equation represents the "continuous equation" in fluid dynamics, while the second corresponds to the "Euler equation". It should be noted that the evolution equations of δP and σ as well as $w = \bar{P}/\bar{\rho}$ and $\delta P/\delta\rho$ are obtained only from the Boltzmann equation. By perturbing the Einstein's equation (Eq. (2.5)), we obtain the following equations:
— *Synchronous gauge* —

$$
\begin{aligned}
k^2\eta - \frac{1}{2}\frac{\dot{a}}{a}\dot{h} &= 4\pi G a^2 \delta T^0{}_0 = -4\pi G a^2 \delta\rho\,, && (2.58)\\
k^2\dot{\eta} &= 4\pi G a^2 i k_i \delta T^0{}_i = 4\pi G a^2(\bar{\rho}+\bar{P})\theta\,, && (2.59)\\
\ddot{\eta} + 2\frac{\dot{a}}{a}\dot{h} - 2k^2\eta &= -8\pi G a^2 \delta T^i{}_i = -24\pi G a^2 \delta P\,, && (2.60)\\
\ddot{h} + 6\ddot{\eta} + 2\frac{\dot{a}}{a}(\dot{h}+6\dot{\eta}) - 2k^2\eta &= 24\pi G a^2 \left(\hat{k}_i\hat{k}_j - \frac{1}{3}\delta_{ij}\right)\delta T^i{}_j \\
&= -24\pi G a^2(\bar{\rho}+\bar{P})\sigma\,. && (2.61)
\end{aligned}
$$

— *Conformal Newtonian gauge* —

$$
\begin{aligned}
k^2\phi + 3\frac{\dot{a}}{a}\left(\dot{\phi} + \frac{\dot{a}}{a}\psi\right) &= 4\pi G a^2 \delta T^0{}_0 = -4\pi G a^2\delta\rho\,, && (2.62)\\
k^2\left(\dot{\phi} + \frac{\dot{a}}{a}\psi\right) &= 4\pi G a^2 i k_i \delta T^0_i \\
&= 4\pi G a^2(\bar{\rho}+\bar{P})\theta\,, && (2.63)\\
\ddot{\phi} + \frac{\dot{a}}{a}(\dot{\psi}+2\dot{\phi}) + \left\{2\frac{\ddot{a}}{a} - \left(\frac{\dot{a}}{a}\right)^2\right\}\psi + \frac{k^2}{3}(\phi-\psi) &= \frac{4\pi G}{3}a^2\delta T^i{}_i = 4\pi G a^2\delta P\,, && (2.64)\\
k^2(\phi-\psi) &= -12\pi G a^2\left(\hat{k}_i\hat{k}_j - \frac{1}{3}\delta_{ij}\right)\delta T^i{}_j \\
&= 12\pi G a^2(\bar{\rho}+\bar{P})\sigma\,. && (2.65)
\end{aligned}
$$

The final task in this subection is to derive the Boltzmann equation of the perturbed phase-space density $\delta f(x^i, P_j, \tau)$ and clarify its relation to the fluid dynamical variables $\delta\rho$, θ, δP, and σ. First, we change the momentum variables from P_i to $(q, \hat{q}_i)$ defined such that
— *Synchronous gauge* —

$$P_\mu = (-\epsilon, (\delta_{ij} + h_{ij}/2)q_j)\,, \tag{2.66}$$

— *Conformal Newtonian gauge* —

$$P_\mu = (-(1+\psi)\epsilon, (1-\phi)q_i)\,, \tag{2.67}$$

where q_i is the comoving momentum, $q_i = q\hat{q}_i$, $\hat{q}_i\hat{q}_i = 1$, and ϵ is the comoving energy $\epsilon = \sqrt{q^2 + a^2m^2}$. By substituting
— *Synchronous gauge* —

$$(-g)^{-1/2} = a^{-4}(1 - h/2)\,, \quad d^3P_i = (1+h/2)\,q^2 dq d^2\hat{q}\,, \tag{2.68}$$

— *Conformal Newtonian gauge* —

$$(-g)^{-1/2} = a^{-4}(1 - \psi + 3\phi)\,, \quad d^3P_i = (1-3\phi)\,q^2 dq d^2\hat{q}\,, \tag{2.69}$$

to Eq. (2.13) and noting that $\bar{f}$ is homogenous and isotropic, we obtain
— *Synchronous gauge* —

$$\delta\rho = -\delta T^0{}_0 = a^{-4}\int \frac{q^2 dq d^2\hat{q}}{(2\pi)^3}\,\epsilon\,\delta f\,, \tag{2.70}$$

$$(\bar{\rho}+\bar{P})\theta = ik_i\delta T^0{}_i = a^{-4}\int \frac{q^2 dq d^2\hat{q}}{(2\pi)^3}\,qk\,i\hat{k}_i\hat{q}_j\left[\frac{1}{2}h_{ij}\,\bar{f}+\delta_{ij}\,\delta f\right]$$
$$= a^{-4}\int \frac{q^2 dq d^2\hat{q}}{(2\pi)^3}\,qk\,iP_1(\hat{k}_i\hat{q}_i)\,\delta f\,, \tag{2.71}$$

$$\delta P = \frac{1}{3}\delta T^i{}_i = a^{-4}\int \frac{q^2 dq d^2\hat{q}}{(2\pi)^3}\,\frac{q^2}{3\epsilon}\,\delta f\,, \tag{2.72}$$

$$(\bar{\rho}+\bar{P})\sigma = -\left(\hat{k}_i\hat{k}_j-\frac{1}{3}\delta_{ij}\right)\delta T^i{}_j = a^{-4}\int \frac{q^2 dq d^2\hat{q}}{(2\pi)^3}\,\frac{q^2}{3\epsilon}2i^2P_2(\hat{k}_i\hat{q}_i)\,\delta f\,, \tag{2.73}$$

— *Conformal Newtonian gauge* —

$$\delta\rho = -\delta T^0{}_0 = a^{-4}\int \frac{q^2 dq d^2\hat{q}}{(2\pi)^3}\,\epsilon\,P_0(\hat{k}_i\hat{q}_i)\,\delta f\,, \tag{2.74}$$

$$(\bar{\rho}+\bar{P})\theta = ik_i\delta T^0{}_i = a^{-4}\int \frac{q^2 dq d^2\hat{q}}{(2\pi)^3}\,qk\,i\hat{k}_i\hat{q}_i\left[-(\phi+\psi)\,\bar{f}+\delta f\right]$$
$$= a^{-4}\int \frac{q^2 dq d^2\hat{q}}{(2\pi)^3}\,qk\,iP_1(\hat{k}_i\hat{q}_i)\,\delta f\,, \tag{2.75}$$

$$\delta P = \frac{1}{3}\delta T^i{}_i = a^{-4}\int \frac{q^2 dq d^2\hat{q}}{(2\pi)^3}\,\frac{q^2}{3\epsilon}\,P_0(\hat{k}_i\hat{q}_i)\,\delta f\,, \tag{2.76}$$

$$(\bar{\rho}+\bar{P})\sigma = -\left(\hat{k}_i\hat{k}_j-\frac{1}{3}\delta_{ij}\right)\delta T^i{}_j = a^{-4}\int \frac{q^2 dq d^2\hat{q}}{(2\pi)^3}\,\frac{q^2}{3\epsilon}2i^2P_2(\hat{k}_i\hat{q}_i)\,\delta f\,, \tag{2.77}$$

where we have introduced the Legendre polynomial $P_l(x)$, e.g. $P_0(x)=1$, $P_1(x)=x$, and $P_2(x)=(3x^2-1)/2$. It should be noted that the fluid dynamical variables are composed of the up to second momenta of the phase-space distribution ($P_l(x),\ l\le 2$). Since only the fluid dynamical variables couple to the gravity directly, higher momenta ($l\ge 3$) of the phase-space distribution affects only the evolution of the fluid dynamical variables. The relations between the perturbed phase-space density and the fluid dynamical variables result in the same form in both gauges. The geodesic equation (Eq. (2.2)) leads to
— *Synchronous gauge* —

$$\frac{dq}{d\tau} = -\frac{1}{2}q\dot{h}_{ij}\hat{q}_i\hat{q}_j = -\frac{1}{6}q\left[P_0(\hat{k}_i\hat{q}_i)\,\dot{h}+2P_2(\hat{k}_i\hat{q}_i)\,(\dot{h}+6\dot{\eta})\right]\,. \tag{2.78}$$

— *Conformal Newtonian gauge* —

$$\frac{dq}{d\tau} = q\dot{\phi}-\epsilon\,\hat{q}_i\,ik_i\,\psi = q\left[P_0(\hat{k}_i\hat{q}_i)\,\dot{\phi}-\frac{\epsilon}{q}\,iP_1(\hat{k}_i\hat{q}_i)\,\psi\right]\,. \tag{2.79}$$

Consequently, we obtain the Boltzmann equation of $\delta f(k_i,P_j,\tau)$ (see Eq. (2.17)),
— *Synchronous gauge* —

$$\frac{\partial}{\partial\tau}\delta f+\frac{q}{\epsilon}\,i\hat{k}_i\hat{q}_i\,\delta f-\frac{1}{6}\frac{d\bar{f}}{d\ln q}\left[P_0(\hat{k}_i\hat{q}_i)\,\dot{h}+2P_2(\hat{k}_i\hat{q}_i)\,(\dot{h}+6\dot{\eta})\right]=0\,. \tag{2.80}$$

— *Conformal Newtonian gauge* —

$$\frac{\partial}{\partial\tau}\delta f + \frac{q}{\epsilon}\, i\hat{k}_i\hat{q}_i\, \delta f + \frac{d\bar{f}}{d\ln q}\left[P_0(\hat{k}_i\hat{q}_i)\,\dot{\phi} - \frac{\epsilon}{q}\, iP_1(\hat{k}_i\hat{q}_i)\,\psi\right] = 0\,. \tag{2.81}$$

We can easily check Eq. (2.70)-(2.77) satisfy the energy-momentum conservation (Eq. (2.54)-(2.57)) with the help of Eq. (2.80)-(2.81).

2.1.5 Cosmological perturbations of free-streaming dark matter

We can apply the general formulation derived in subsection 2.1.4 to free-streaming dark matter. Dark matter is often assumed to be cold. In the hypothesis of cold dark matter (CDM), dark matter particles compose the pressure-less perfect fluids, while they are collisionless (freely streaming). This implies that only ρ_c ($= \bar{\rho}_c + \delta\rho_c$) and θ_c are non-zero while the other quantities (e.g. P_c, σ_c) are set to be zero. [3] The unperturbed energy (number) density of CDM is diluted by the cosmic expansion, $\bar{\rho}_c \propto a^{-3}$. The resultant evolution equations of perturbations are
— *Synchronous gauge* —

$$\dot{\delta}_c = -\theta_c - \frac{1}{2}\dot{h}\,, \quad \dot{\theta}_c = -\frac{\dot{a}}{a}\theta_c\,. \tag{2.83}$$

— *Conformal Newtonian gauge* —

$$\dot{\delta}_c = -\theta_c + 3\dot{\phi}\,, \quad \dot{\theta}_c = -\frac{\dot{a}}{a}\theta_c + k^2\psi\,. \tag{2.84}$$

It should be noted that the above evolution equations form a closed set. As we can see from the second equation in the synchronous gauge, if $\theta_c(\mathrm{Syn})$ is zero at some time, it is zero at any time. We can set $\theta_c(\mathrm{Syn}) = 0$ by using the residual gauge degrees of freedom. Conversely, we often fix the residual gauge degrees of freedom in the synchronous gauge by setting $\theta_c(\mathrm{Syn}) = 0$.

The realistic candidates of dark matter have finite thermal velocity (finite q) and its fluid dynamical description breaks down. As the Universe expands, the comoving energy $\epsilon = \sqrt{q^2 + a^2m^2}$ shifts from the relativistic one $\epsilon \simeq q$ to the non-relativistic one $\epsilon \simeq am$ and thus, the unperturbed fluid of dark matter (see Eq. (2.33)-(2.34)) shifts from the relativistic one (radiation), $\bar{\rho}_c \simeq 3\bar{P}_c$ ($\propto a^{-4}$) to the non-relativistic one (CDM), $\bar{\rho}_c$ ($\propto a^{-3}$), $\bar{P}_c \simeq 0$. Since the evolution equations of the fluid dynamical variables do not form a closed set, we should solve the Boltzmann equation (Eq. (2.80)-(2.81)). However, it is very challenging to solve the Boltzmann equation numerically even with state-of-art computing clusters [27]. Therefore, we should develop an approximation method. Here, it is a key observation that the gravity couples only to the up to second momenta ($l \leq 2$) of the phase-space distribution. We decompose the perturbed phase-space distribution $\delta f(k_i, q_j, \tau)$ into the angular momentum eigenstates,

$$\delta f = \bar{f}\sum_l (-i)^l(2l+1)P_l(\hat{k}_i\hat{q}_i)\Psi_l\,. \tag{2.85}$$

[3] We can realize CDM by considering a massive particle with a zero-temperature thermal distribution,

$$f_c = g_s \exp\left(\frac{P_\mu u_c^\mu + \mu_c}{T_c}\right)\Big|_{T_c\to 0}\,. \tag{2.82}$$

Here, the chemical potential is set to reproduce a given CDM mass density. From this observation, we often say that CDM particles do not have any thermal velocity.

In terms of Ψ_l, the fluid dynamical variables are rewritten as

$$\delta\rho = a^{-4}\int \frac{4\pi q^2 dq}{(2\pi)^3}\,\epsilon\,\bar{f}\,\Psi_0\,, \tag{2.86}$$

$$(\bar{\rho}+\bar{P})\theta = a^{-4}\int \frac{q^2 dq}{(2\pi)^3}\,qk\,\bar{f}\,\Psi_1\,, \tag{2.87}$$

$$\delta P = a^{-4}\int \frac{q^2 dq}{(2\pi)^3}\,\frac{q^2}{3\epsilon}\,\bar{f}\,\Psi_0\,, \tag{2.88}$$

$$(\bar{\rho}+\bar{P})\sigma = a^{-4}\int \frac{q^2 dq}{(2\pi)^3}\,\frac{2q^2}{3\epsilon}\bar{f}\,\Psi_2\,, \tag{2.89}$$

in both two gauges. The Boltzmann equation leads to
— *Synchronous gauge* —

$$\dot{\Psi}_0 = -\frac{qk}{\epsilon}\Psi_1 + \frac{1}{6}\dot{h}\,\frac{d\ln\bar{f}}{d\ln q}\,, \tag{2.90}$$

$$\dot{\Psi}_1 = \frac{qk}{3\epsilon}(\Psi_0 - 2\Psi_2)\,, \tag{2.91}$$

$$\dot{\Psi}_2 = \frac{qk}{5\epsilon}(2\Psi_1 - 3\Psi_3) - \frac{1}{15}(\dot{h}+6\dot{\eta})\,\frac{d\ln\bar{f}}{d\ln q}\,, \tag{2.92}$$

$$\dot{\Psi}_l = \frac{qk}{(2l+1)\epsilon}\left[l\Psi_{l-1} - (l+1)\Psi_{l+1}\right] \quad (l\geq 3). \tag{2.93}$$

— *Conformal Newtonian gauge* —

$$\dot{\Psi}_0 = -\frac{qk}{\epsilon}\Psi_1 - \dot{\phi}\,\frac{d\ln\bar{f}}{d\ln q}\,, \tag{2.94}$$

$$\dot{\Psi}_1 = \frac{qk}{3\epsilon}(\Psi_0 - 2\Psi_2) - \frac{\epsilon k}{3q}\psi\,\frac{d\ln\bar{f}}{d\ln q}\,, \tag{2.95}$$

$$\dot{\Psi}_l = \frac{qk}{(2l+1)\epsilon}\left[l\Psi_{l-1} - (l+1)\Psi_{l+1}\right] \quad (l\geq 2). \tag{2.96}$$

We have derived the above formulas, assuming only that the particles are free-streaming. Therefore, the above formulas can be applied to not only dark matter, but also more general particles, e.g. massive neutrinos. Furthermore, massless particles follow the same equations with $\epsilon = q$ unless they are collisionless. In this case, q-dependence appears only as $d\ln\bar{f}/d\ln q$ in the Boltzmann hierarchy (Eq. (2.90)-(2.96)). Even this residual q-dependence can be eliminated when we define the new perturbed variables F_l such that

$$\left(\int q^2 dq\, q\,\bar{f}\right) F_l = \int q^2 dq\, q\,\bar{f}\,\Psi_l\,. \tag{2.97}$$

In terms of F_l, the fluid dynamical variables are written by

$$\delta = F_0\,, \quad \theta = \frac{3}{4}kF_1\,, \quad \delta P = \frac{1}{3}\bar{\rho}\,F_0\,, \quad \sigma = \frac{1}{2}F_2, \tag{2.98}$$

and the Boltzmann hierarchy takes a form of

— *Synchronous gauge* —

$$\dot{\delta} = -\frac{4}{3}\theta - \frac{2}{3}\dot{h}\,, \tag{2.99}$$

$$\dot{\theta} = k^2\left(\frac{1}{4}\delta - \sigma\right)\,, \tag{2.100}$$

$$\dot{F}_2 = 2\dot{\sigma} = \frac{8}{15}\theta - \frac{3}{5}kF_3 + \frac{4}{15}(\dot{h} + 6\dot{\eta})\,, \tag{2.101}$$

$$\dot{F}_l = \frac{k}{(2l+1)}\left[lF_{l-1} - (l+1)F_{l+1}\right] \quad (l \geq 3). \tag{2.102}$$

— *Conformal Newtonian gauge* —

$$\dot{\delta} = -\frac{4}{3}\theta + 4\dot{\phi}\,, \tag{2.103}$$

$$\dot{\theta} = k^2\left(\frac{1}{4}\delta - \sigma\right) + k^2\psi\,, \tag{2.104}$$

$$\dot{\Psi}_l = \frac{k}{(2l+1)}\left[lF_{l-1} - (l+1)F_{l+1}\right] \quad (l \geq 2). \tag{2.105}$$

This reformulation drastically reduces the computational cost in the case of massless particles, e.g. massless neutrinos. Let us compare the Boltzmann hierarchies for massive particles (Eq. (2.90)-(2.96)) and massless particles (Eq. (2.99)-(2.105)). The evolution of perturbed phase-space distribution depends on the shape of unperturbed phase-space distribution for massive particles. On the other hand, that is not the case for massless particles.

Chapter 3

Structure of Dark Matter Halos in Warm Dark Matter models and in models with Long-Lived Charged Massive Particles

The precise measurement of the CMB anisotropies established the standard ΛCDM cosmology [28]. Observations of the large-scale structure of the Universe, such as the galaxy power spectra from the Sloan Digital Sky Survey (SDSS) also confirmed its success in predicting the large scale structures of the Universe (e.g. [12, 13, 14]).

The validity of the ΛCDM model on the galactic and the subgalactic scales has long been caught up in debate. Moore et al. [29] argue that the number of dark matter subhalos is $10-100$ times larger than the number of satellites observed around the Milky Way [30]. The so-called "missing satellite problem" has been revisited in a somewhat quantitative context [31, 32, 33]. For example, Boylan-Kolchin et al. [31] argue that, in the ΛCDM model, ~ 10 most massive subhalos in a galactic halo are too concentrated to be consistent with the kinematic data for the bright Milky Way satellites. Also, observations of the rotation velocities of galaxies using the 21 cm line by Papastergis et al. [34] show that the abundance of galaxies with observed velocity width $w = 50\,\mathrm{km\,s^{-1}}$ is ~ 8 times lower than predicted in the ΛCDM model.

It is often suggested that WDM models resolve the apparent problems on subgalactic scales [35]. WDM particles have non-negligible velocity dispersions, which act as an effective "pressure" of the WDM fluid. Essentially, the subgalactic-scale density fluctuations are suppressed. The resultant matter power spectrum is quickly reduced around the cut-off scale that is determined by the velocity dispersion. Motivated by the recent interest in this problem, several authors study the structure formation in WDM models [36, 37, 38, 39, 40, 41, 42, 43, 44, 45, 46].

Constraints on WDM models can be obtained from astronomical observations. Observations of Lyman-α forests are often used for the purpose [47, 48]. Absorption features in quasar spectra reflect the number density of neutral hydrogen, from which we can estimate the matter power spectrum along the line of sight, even at large wavenumbers $k \sim 10\,h\,\mathrm{Mpc^{-1}}$. WDM models have also interesting implications for the cosmic reionization [49, 50, 51]. The formation of the first objects, and hence the production of ionizing photons, are delayed in WDM models. On the other hand, WDM models could help the completion of the cosmic reionization. Yue & Chen [52] suggest that the reduced number of subhalos in WDM models makes the recombination of ionized hydrogens inefficient and results in earlier completion of the cosmic reionization. It is clearly important to

study the clustering properties in WDM models in both linear and non-linear evolution regimes.

There are also renewed interest in particle physics. Several candidates for WDM are suggested in particle physics models beyond the Standard Model, such as light gravitinos [53], sterile neutrinos (see Ref. [54] for a review and references) and superWIMPs [55]. It is important to notice that WDM particles can be produced via different mechanisms. Nevertheless, the above constraints from astronomical observations are focused on a single quantity, e.g., the mass of WDM particle in a specific model. It is unclear if such constraints can be applied to WDM models with different production mechanisms. Detailed comparisons of a wide class of models are clearly needed.

In this chapter, we also consider a Long-Lived CHAMP model. Throughout this chapter, we assume that CHAMPs have an elementary charge, either positive or negative. CHAMPs are generally realized in models beyond the Standard Model of particle physics. One such example is a slepton, a superpartner of leptons in supersymmetric models. Sleptons as the lightest supersymmetry particles (LSPs) are stable when R-parity is conserved. The abundance of such stable CHAMPs, however, is severely constrained by the searches in deep sea water (see Ref. [56] for a review and references). CHAMPs can also be unstable; a CHAMP decay into neutral dark matter and other decay products including at least one charged particle. For example, the stau can be the next lightest supersymmetric particle (NLSP) when the gravitino is the LSP [57]. It is well-known that CHAMPs could affect the big bang nucleosynthesis (BBN) reaction rates and thus change the abundance of light elements [58, 59, 60, 61, 62, 63, 64, 65, 66, 67]. Several authors [68, 69] suggest the possibility that CHAMPs with a lifetime about 1 yr can act effectively as WDM through acoustic oscillations in the thermal background. We study the effect of the oscillations on the matter power spectrum.

We calculate the linear evolution of the matter density fluctuations for the three WDM models and the Long-Lived CHAMP model. We show that the comoving Jeans scale at the matter-radiation equality characterises the linear matter power spectra in the three WDM models well. We use the obtained linear matter power spectra as initial conditions of N-body simulations to follow the non-linear evolution of the matter distribution. We compare the halo mass functions, the subhalo mass functions, and the radial distributions of subhalos in Milky Way-size halos to discuss the clustering properties in the WDM models and in the Long-Lived CHAMP model. We show that these statistics are similar when the cut-off scale is kept the same. We find that the WDM models and the Long-Lived CHAMP model with the characteristic cut-off scale $k_{\rm cut} \sim 20 - 260\,h\,{\rm Mpc}^{-1}$ resolve the so-called "missing satellite problem".

The rest of this chapter is organised as follows. In Sec. 3.1, we summarize three WDM models and a Long-Lived CHAMP model we consider. Then, we introduce the common cut-off scale $k_{\rm cut}$ which characterises the linear matter power spectra in these models. In Sec. 3.2, after describing the details of N-body simulations, we show simulation results and discuss their implications. Specifically, we mention the similarity of these models with the same cut-off and the possibility that CHAMPs behave like WDMs and resolve the "missing satellite problem". Finally, in Sec. 5.4, concluding remarks are given.

Throughout this chapter, we take the cosmological parameters that are given in Ref. [28] as the *WMAP*+BAO+H_0 Mean; $100\Omega_b h^2 = 2.255$, $\Omega_{\rm CDM} h^2 = 0.1126$, $\Omega_\Lambda = 0.725$, $n_s = 0.968$, $\tau = 0.088$ and $\Delta^2_R(k_0) = 2.430 \times 10^{-9}$, while we replace the energy density of CDM $\Omega_{\rm CDM} h^2$ by the energy density of WDM $\Omega_{\rm WDM} h^2$ for the WDM models and by the energy density of neutral dark matter produced by the CHAMP decay for the Long-Lived CHAMP model.

3.1 WDM models and Long-Lived CHAMP model

In this section, we summarize three WDM models and a Long-Lived CHAMP model we consider in this chapter. We describe production mechanisms of WDM particles in each model and show the exact shapes of the velocity distribution. In the following subsections, we focus on three WDM models to specify our discussion, although our results can be applied to any WDM models with the same shape of the velocity distribution. Then, we introduce the Jeans scale at the matter-radiation equality. The matter power spectra in the three WDM models with the same Jeans scale at the matter-radiation equality are very similar. Their initial velocity distributions affect the damping tail of the matter power spectra. We also describe the evolution of the linear matter density fluctuations in a Long-Lived CHAMP model. The matter power spectrum is truncated around the horizon scale at the time when CHAMPs decay. Interestingly, the resulting power spectrum appears similar to those in WDM models.

3.1.1 Thermal WDM

In this type of models, fermionic WDM particles are produced in the thermal background. They are decoupled from the thermal background as the Universe expands and cools. At the time of the decoupling, their momentum obeys the thermal distribution, that is, the Fermi-Dirac distribution. We consider the generalized Fermi-Dirac distribution,

$$f(p) = \frac{\beta}{e^{p/T_{\rm WDM}} + 1} \,. \tag{3.1}$$

Here and in the following, p denotes the comoving momentum of WDM particles, and $T_{\rm WDM}$ is the effective temperature that characterises the comoving momentum of WDM particles. In the case of the light gravitino [70] and the thermally produced sterile neutrino [71], $T_{\rm WDM}$ relates to the temperature of the left-handed neutrino T_ν through the conservation of the entropy, $T_{\rm WDM} = \left(\frac{43/4}{g_{\rm dec}}\right)^{1/3} T_\nu$ where $g_{\rm dec}$ is the effective number of the massless degrees of freedom at the decoupling from the thermal background. Note that β determines the overall normalization of the momentum distribution and $\beta = 1$ in the case of the gravitino and the thermally produced sterile neutrino. Dodelson and Widrow [72] propose the sterile neutrino dark matter produced via active-sterile neutrino oscillations. In this case, the active neutrinos in the thermal background turn into the sterile neutrino via the coherent forward scattering [73]. The resultant momentum distribution of the sterile neutrino is given by the generalized Fermi-Dirac distribution (see Eq. (3.1)) with $T_{\rm WDM} \simeq T_\nu$ and $\beta \propto \theta_{\rm m}^2 M$ where $\theta_{\rm m}$ is the active-sterile mixing angle and M is the mass of the sterile neutrino.

3.1.2 WDM produced by the thermal boson decay

There are models in which the Majorana mass of the sterile neutrino arises from the Yukawa coupling Y with a singlet boson [74, 75]. In these models, the singlet boson couples to the Standard Model Higgs boson through an extension of the Standard Models Higgs sector. The singlet Higgs boson has a vacuum expectation value (VEV) of the order of the electroweak scale when the electroweak symmetry breaks down. When the sterile neutrino is assumed to be WDM with a mass of an order of keV, the Yukawa coupling should be very small $Y \sim O(10^{-8})$. This small Yukawa coupling makes the singlet boson decay to the two sterile neutrinos when the singlet boson is relativistic and is in equilibrium with the thermal background. Here, it should be noted that the sterile neutrino model is one specific example. In WDM models, where relativistic bosonic particles

in equilibrium with the thermal background decay into fermionic WDM particles through the Yukawa interaction, WDM particles have the same resultant momentum distribution (see Eq. (3.2) below). The resultant momentum distribution is obtained by solving the Boltzmann equation [76],

$$f(p) = \frac{\beta}{(p/T_{\rm WDM})^{1/2}} g_{5/2}(p/T_{\rm WDM}) \tag{3.2}$$

where

$$g_\nu(x) = \sum_{n=1}^{\infty} \frac{e^{-nx}}{n^\nu} \,. \tag{3.3}$$

Here, we have ignored the low momentum cut-off that ensures the Pauli blocking, while it does not change our results. The effective temperature is given by $T_{\rm WDM} = \left(\frac{43/4}{g_{\rm pro}}\right)^{1/3} T_\nu$ with the effective number of massless degrees of freedom at the production of the sterile neutrino $g_{\rm pro} \sim 100$. The normalization factor β is determined by the Yukawa coupling Y and the mass of the singlet Higgs boson M, $\beta \propto Y^2 M^{-1}$. The velocity distribution have an enhancement $f_{\rm B} \propto p^{-1/2}$ at the low momentum $p/T_{\rm WDM} \ll 1$, since the sterile neutrinos with lower momenta are produced by the less boosted singlet boson, the decay rate of which is larger due to the absence of the time dilation. This enhancement indicates the "colder" (than the thermal WDM) property of the sterile neutrino dark matter produced by the decay of the singlet heavy boson.

3.1.3 WDM produced by the non-relativistic particle decay

In this type of models, a non-relativistic heavy particle decays into two particles, one or both of which become WDM. Supersymmetric theories realize this type of scenarios e.g. when the LSP is the gravitino and the NLSP is a neutralino. The relic abundance of the NLSP neutralino is determined at the time of chemical decoupling by the standard argument [77, 78]. Eventually, the non-relativistic neutralinos decay into LSP gravitinos that become WDM. The particles produced by the decay of the moduli fields and of the inflaton fields are another candidates of this type of WDM [79, 80, 81, 82, 83]. When we assume the heavy particle decays in the radiation dominated era, the momentum distribution of the decay products is given by [84, 85, 86],

$$f(p) = \frac{\beta}{(p/T_{\rm WDM})} \exp(-p^2/T_{\rm WDM}^2) \,, \tag{3.4}$$

where $T_{\rm WDM}$ is given by $T_{\rm WDM} = P_{\rm cm} a(t_d)/a(t_0)$ with the physical canter-of-mass momentum $P_{\rm cm}$, the scale factor $a(t)$ at the decay time t_d and at the present time t_0. We have defined t_d as $H(t = t_d) = 1/2\tau$ where $H(t)$ is the Hubble parameter and τ is the lifetime of the heavy particle.

3.1.4 Jeans scale at the matter-radiation equality

Now, we introduce two quantities to characterise the property of WDM. One is the present energy density of WDM, $\Omega_{\rm WDM} \equiv \frac{\rho_{\rm WDM}}{\rho_{\rm crit}}\big|_{t=t_0}$. Throughout this chapter, we assume WDM particles account for all of the dark matter, letting $\Omega_{\rm WDM} h^2 = 0.1126$. Another important physical scale is the comoving Jeans scale at the matter radiation equality $t_{\rm eq}$,

$$k_{\rm J} = a \sqrt{\frac{4\pi G \rho_{\rm M}}{\sigma^2}}\bigg|_{t=t_{\rm eq}} \tag{3.5}$$

with the gravitational constant G. Here, $\rho_{\rm M}$ is the matter density and σ^2 is the mean square of the velocity of the dark matter particles (see Eq. (3.8) below). Dark matter particles with $k_{\rm J} \sim 100 - 1000\,{\rm Mpc}^{-1}$ are usually called WDM and expected to resolve the "missing satellite problem".

We note that, in the present chapter, we do not consider whether or not a particular set of $\Omega_{\rm WDM}$ and $k_{\rm J}$ is in a viable region of the respective model. One such example is the gravitino WDM, a representative of the Thermal WDM model (see subsection 3.1.1). This model has only two parameters, the effective number of the massless degrees of freedom at the decoupling $g_{\rm dec}$ and the gravitino mass $m_{3/2}$, to set $\Omega_{\rm WDM}$ and $k_{\rm J}$. When we assume $k_{\rm J} \simeq 30\,{\rm Mpc}^{-1}$, these two parameters are determined as $g_{\rm dec} \simeq 1000$ and $m_{3/2} \simeq 1\,{\rm keV}$. The effective number of the massless degrees of freedom at the decoupling of the gravitino is at most $g_{\rm dec} \sim 200$ in the Minimal Supersymmetric Standard Model (MSSM), and hence, another mechanism such as entropy production is needed to explain the gravitino WDM [87, 88].

3.1.5 Linear matter power spectra and Normalized velocity distribution

We follow the evolution of the primordial adiabatic fluctuations for the three WDM models by modifying suitably the public software, `CAMB` [89]. We adopt the covariant multipole perturbation approach for the massive neutrino [26, 90]. We replace the Fermi-Dirac distribution of the massive neutrino by the momentum distributions of the WDM models discussed above. Our approach is valid when the WDM particles are kinematically decoupled at the cosmic time of interest. The Jeans scale of interest is around $k_{\rm J} \sim O(100)\,{\rm Mpc}^{-1}$. The primordial fluctuation of this wavenumber enters the horizon at $T \sim O(10)\,{\rm keV}$. In a large class of WDM models, WDM particles are kinematically decoupled before the QCD phase transition, $T_{\rm QCD} \sim 100\,{\rm MeV}$, and thus our calculation is valid. [1]

For comparison, we calculate the normalized velocity distributions for the WDM models and the linear matter power spectra extrapolated to the present time $z = 0$. The results are shown in Fig. 3.1 for $k_{\rm J} = 16\,{\rm Mpc}^{-1}$, which correspond to $m_{3/2} \simeq 1\,{\rm keV}$ for the thermally-produced gravitino WDM. Here, we have defined the dimensionless matter power spectra as,

$$\Delta(k) \equiv \frac{1}{2\pi^2} k^3 P(k) \tag{3.6}$$

with the matter power spectra $P(k)$.

The velocity distribution $g(v)$ is normalized as follows:

$$\int_0^\infty dv\, g(v) = 1\,, \tag{3.7}$$

$$\int_0^\infty dv\, v^2 g(v) = \sigma^2 \tag{3.8}$$

with the variance (second moment) of the velocity σ^2. Note that the first equation is normalized with respect to the present energy density of WDM, $\Omega_{\rm WDM}$, whereas the second equation relates the velocity variance to the comoving Jeans scale at the matter radiation equality $k_{\rm J}$ given by

[1] There are variants of WDM models in which WDM particles are produced by the non-relativistic particle decay at late epochs. The matter power spectrum could be affected if the parent particles decay around the matter-radiation equality. In this case, the matter density during the radiation-dominated era is mostly contributed by the parent (cold) particles, rather than by the decay products, and then the density fluctuations of the cold, neutral parent particles can grow logarithmically. Note that the effect is more pronounced if the parent particles are charged (see subsection 3.1.6).

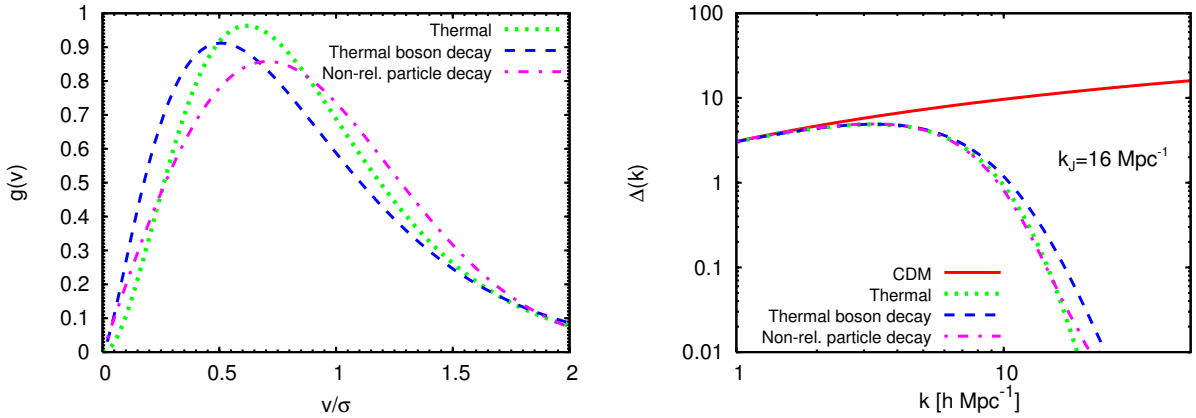

Figure 3.1: *The normalized velocity distributions (left panel) and the dimensionless linear matter power spectra (right panel) for the standard CDM model and the three WDM models with* $k_{\rm J} = 16\,{\rm Mpc}^{-1}$.

Eq. (3.5). One can then expect that the power spectra for the WDM models with the same $\Omega_{\rm WDM}$ and $k_{\rm J}$ are very similar, as seen in Fig. 3.1. There, we see differences between the WDM models only in the damping tail of the power spectra at $k > 10\,h\,{\rm Mpc}^{-1}$.

3.1.6 Long-Lived CHAMP and Cut-off scale

Sigurdson & Kamionkowski [68] formulate the linearized evolution equations for fluctuations in a Long-Lived CHAMP model. They show that the subgalactic-scale matter density fluctuations are damped via a mechanism called "acoustic damping". The comoving horizon scale at which CHAMP decays determines the cut-off scale of the matter power spectrum, which is defined by [91, 69]

$$k_{\rm Ch} = aH|_{t=\tau_{\rm Ch}}, \tag{3.9}$$

where H is the Hubble parameter and $\tau_{\rm Ch}$ is the lifetime of CHAMP. Smaller-scale density fluctuations with $k > k_{\rm Ch}$ enter the horizon before CHAMP decays and can not grow due to the acoustic oscillations of CHAMP in the thermal background. On the other hand, larger-scale density fluctuations with $k < k_{\rm Ch}$ grow logarithmically even after entering the horizon due to the gravitational instability as the density fluctuations of CDM. We assume CHAMPs decay in the radiation dominated era. Then the comoving horizon scale at $t = \tau_{\rm Ch}$ is evaluated as,

$$k_{\rm Ch} = 2.2\,{\rm Mpc}^{-1} \times \left(\frac{\tau_{\rm Ch}}{\rm yr}\right)^{-1/2} \left(\frac{g_{\rm Ch}}{3.363}\right)^{1/4} \tag{3.10}$$

where $g_{\rm Ch}$ is the effective number of massless degrees of freedom when CHAMP decays.

We need to consider three physical processes for the CHAMP model. First, we describe the neutralization of CHAMP. A positively charged particle may become neutral by forming a bound state with an electron e. Its binding energy is, however, almost the same as the hydrogen, $E_{{\rm b}\,e} \simeq 13.6\,{\rm eV}$. Hence, the positively charged particle keeps charged until its decay, since we assume CHAMP decays in the radiation dominated era. A negatively charged particle may become neutral by forming a bound state with a proton p. Its binding energy $E_{{\rm b}\,p} \simeq 25\,{\rm keV}$ is almost $m_{^4{\rm He}}/m_p \sim 2000$ times larger than $E_{{\rm b}\,e}$ and hence is expected to make the negatively charged particle neutral at $T \sim 1\,{\rm keV}$. However, Helium ^{4}He is produced through BBN, with which a negatively charged particle may form a binding state. Its binding energy $E_{{\rm b}\,^4{\rm He}} \simeq 337\,{\rm keV}$ is almost $(Z_{^4{\rm He}}/Z_p)^2 \times m_{^4{\rm He}}/m_p \simeq 16$ times larger than $E_{{\rm b}\,p}$. It should be noted that even a negatively charged particle

bound with a proton is wrested by ^{4}He through a charge-exchange reaction [92]. Therefore, when the yield of CHAMP $Y_{\rm Ch}$ ($Y \equiv n/s$ with the number density n and the entropy density s) is smaller than the yield of the Helium $Y_{^4{\rm He}}$, almost every negatively charged particle forms a binding state with a helium nuclei, which has one positive elementary charge [69].

Second, the decay products of CHAMP may lead to energy injection to the thermal background. The resulting injection energy density is constrained from the photodissociation of BBN [93] and CMB y- and $\mu-$ parameters [94]. However, models with CHAMP with almost the same mass with neutral dark matter are not severely constrained by BBN nor by CMB. We focus on such an "unconstrained" model. Note that the small mass splitting ensures the relatively long lifetime of CHAMP and the "coldness" of neutral dark matter.

Finally, CHAMPs are tightly coupled with baryons before its decay. Sigurdson & Kamionkowski [68] assume $\theta_{\rm baryon} = \theta_{\rm Ch}$ where θ is the divergence of the fluid velocity. This approximation is valid when the Coulomb scattering between baryons and CHAMPs is efficient, i.e., CHAMPs and baryons are tightly coupled. However, the constraints from the Catalyzed BBN essentially allow only heavy CHAMP with $m_{\rm Ch} \gtrsim 10^6\,{\rm GeV}$ for $\tau_{\rm Ch} \gtrsim 10^3{\rm sec}$. It is unclear if the Coulomb scattering between baryons and such heavy CHAMPs is efficient. We have calculated the scattering efficiency and found that the tightly coupled approximation is indeed valid through the epoch of interest for $m_{\rm Ch} \lesssim 10^8\,{\rm GeV}$. In the following, we adopt the formulation given by Sigurdson & Kamionkowski [68] using the tightly coupled approximation between baryons and CHAMPs. The evolution of energy density of CHAMP is given by,

$$\dot{\bar\rho}_{\rm Ch} = -3\frac{\dot a}{a}\bar\rho_{\rm Ch} - \frac{a}{\tau_{\rm Ch}}\bar\rho_{\rm Ch}\,, \tag{3.11}$$

where dot denotes the derivative in When CHAMP decays, the most of energy density of CHAMP turns into the energy of the neutral dark matter, since we assume that the mass difference between CHAMP and neutral dark matter is tiny. This allows us to write the evolution equation of energy density of dark matter such that,

$$\dot{\bar\rho}_{\rm dm} = -3\frac{\dot a}{a}\bar\rho_{\rm dm} + \frac{a}{\tau_{\rm Ch}}\bar\rho_{\rm Ch}\,. \tag{3.12}$$

Next, we see the effect of CHAMP decay on the evolution of cosmological perturbations (see Chapter 2). We adopt the Synchronous gauge here. The evolution equations of perturbations of CHAMP-baryon fluid is similar to those of baryon fluid in standard ΛCDM cosmology,

$$\dot\delta_\beta = -\theta_\beta - \frac{1}{2}\dot h\,, \tag{3.13}$$

$$\dot\theta_\beta = -\frac{\dot a}{a}\theta_\beta + c^2_{s,\,\beta}k^2\delta_\beta + \frac{4\bar\rho_\gamma}{3\bar\rho_\beta}an_e\sigma_T(\theta_\gamma - \theta_\beta), \tag{3.14}$$

where subscripts γs denote photon. The square of sound speed of CHAMP-baryon fluid $c^2_{s,\,\beta}$ is given by

$$c^2_{s,\,\beta} = \frac{n_\beta T_\beta}{\rho_\beta}\left(1 - \frac{1}{3}\frac{d\ln T_\beta}{d\ln a}\right)\,. \tag{3.15}$$

The CHAMP decay introduce additional terms in the evolution equations of perturbations of neutral dark matter,

$$\dot\delta_{\rm dm} = -\theta_{\rm dm} - \frac{1}{2}\dot h + \frac{\rho_{Ch}}{\rho_{\rm dm}}\frac{a}{\tau_{\rm Ch}}(\delta_\beta - \delta_{\rm dm})\,, \tag{3.16}$$

$$\dot\theta_{\rm dm} = -\frac{\dot a}{a}\theta_{\rm dm} + \frac{\rho_{\rm Ch}}{\rho_{\rm dm}}\frac{a}{\tau_{\rm Ch}}(\theta_\beta - \theta_{\rm dm})\,. \tag{3.17}$$

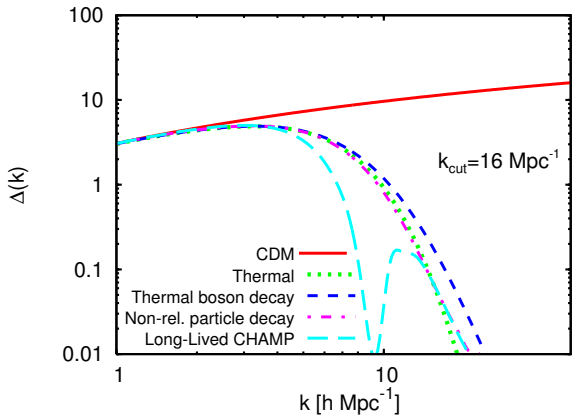

Figure 3.2: *We plot the dimensionless linear matter power spectrum in Long-Lived CHAMP model ($\tau \simeq 2.5$yr). We compare it with the same dimensionless linear matter power spectra in the WDM models as in Fig. 3.1. The oscillation around $k \sim 9\,h\,\mathrm{Mpc}^{-1}$ is the imprint of the "acoustic damping".*

Before CHAMP decays ($\rho_{\rm Ch}/\rho_{\rm dm} \cdot a/\tau_{\rm Ch} \gg \dot{a}/a$), decay terms are dominant and force perturbations of dark matter follow those of CHAMP-baryon fluid, $\delta_\beta = \delta_{\rm dm}$ and $\theta_\beta = \theta_{\rm dm}$. After the decay of CHAMP, decay terms can be ignored and perturbations of dark matter evolve similarly to those in standard ΛCDM cosmology.

We modify `CAMB` [89] to follow the evolution of density fluctuations in the Long-Lived CHAMP model. The basic equations are given in Sigurdson & Kamionkowski [68]. We obtain the power spectra for several $\tau_{\rm Ch}$s (see Eq. (3.10)). We find that the CHAMP matter power spectrum is very similar to the WDM models, as seen in Fig. 3.2, when $k_{\rm Ch}$ is set such that

$$k_{\rm cut} \equiv k_{\rm J} \simeq 11\,k_{\rm Ch}\,. \tag{3.18}$$

Hereafter, we use $k_{\rm cut}$ defined in the above as a characteristic parameter of the models we consider. The corresponding lifetime of CHAMP is $\tau_{\rm Ch} \simeq 2.5\,$yr in the figure. The imprint of the CHAMP "acoustic damping" on the linear matter power spectra is clearly seen. One can naively guess that structures in the Long-Lived CHAMP model would be similar to those in the WDM models. It is important to study the non-linear growth of the matter distributions in the Long-Lived CHAMP model. We use large cosmological N-body simulations to this end.

3.2 Numerical simulations

Our simulation code is the parallel Tree-Particle Mesh code, `GADGET-2` [95]. We use $N = 512^3$ particles in a comoving volume of $L = 10\,h^{-1}\,$Mpc on a side. The mass of a simulation particle is $5.67 \times 10^5\,h^{-1}\,M_{\rm sun}$ and the gravitational softening length is $1\,h^{-1}\,$kpc. We run a friends-of-friends (FoF) group finder [96] to locate groups of galaxies. We also identify substructures (subhalos) in each FoF group using SUB-FIND algorithm developed by Springel et al. [97]. We do not assign any thermal velocity to simulation particles because it can lead to formation of spurious objects [98]. We start our simulation from relatively low redshift $z = 19$, at which the thermal motion of WDM is redshifted and negligible. It should be noted that the heavy, neutral dark matter produced by the CHAMP decay is assumed to have negligible thermal velocities.

In Fig. 3.3, we plot the projected matter distribution in the CDM model (left panel), in the Thermal WDM model (see subsection 3.1.1) (middle panel) and in the Long-Lived CHAMP model

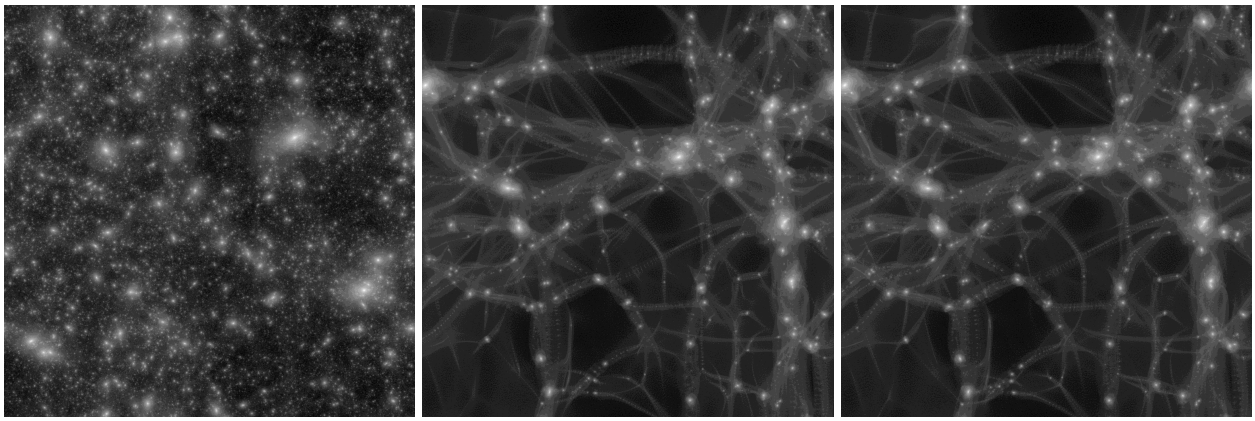

Figure 3.3: *The projected matter distribution in the CDM model (left panel), in the Thermal WDM model (middle panel) and in the Long-Lived CHAMP model (right panel). For the Thermal WDM model and for the Long-Lived CHAMP model, we take the same cut-off scale* $k_{\rm cut} = 16\,{\rm Mpc}^{-1}$ *as in Fig. 3.2. One side of the plotted region is* $L = 10\,h^{-1}\,{\rm Mpc}$*. Brighter regions denote higher matter densities.*

(right panel). For the Thermal WDM model and for the Long-Lived CHAMP model, we set the same cut-off scale $k_{\rm cut} = 16\,{\rm Mpc}^{-1}$ as in Fig. 3.2. One side of the plotted region is $10\,h^{-1}\,{\rm Mpc}$. Regions with high matter densities appear bright in the plot. We see that many small objects, i.e., halos and subhalos, have formed in the CDM model. Contrastingly, in the Thermal WDM model and in the Long-Lived CHAMP model, the matter distribution is much smoother and appears more filamentary. The abundance of small objects is much reduced. Overall, the matter distributions in the Thermal WDM model and in the Long-Lived CHAMP model look similar. Note that numerous small objects along the filaments in the Thermal WDM model and in the Long-Lived CHAMP model could be numerical artifacts; this is a long-standing problem of hot/warm dark matter simulations due to discreteness effects [99, 100]. Earlier studies propose a simple formula for the critical halo mass,

$$M_{\rm c} = 10.1 \times \rho_{\rm M}\, d_{\rm mean}\, k_{\rm peak}^{-2}\,. \tag{3.19}$$

below which the abundance of halos is unreliable. Here, $d_{\rm mean} = L/N^{1/3}$ is the mean comoving distance between simulation particles and $k_{\rm peak}$ is the wavenumber at the maximum of the $\Delta(k)$. We will discuss this point further in the following section.

We compare the halo mass functions in the models we consider in Fig. 3.4. The fiducial cut-off scale is $k_{\rm cut} = 16\,{\rm Mpc}^{-1}$ (left panel) as in Fig. 3.2, but we also show the results for $k_{\rm cut} = 130\,{\rm Mpc}^{-1}$ (right panel). The latter corresponds to $m_{3/2} \simeq 4\,{\rm keV}$ for the thermally-produced gravitino WDM (see subsection 3.1.1) and $\tau_{\rm Ch} \simeq 0.04\,{\rm yr}$ for the Long-Lived CHAMP model. The halo mass M corresponding to $k_{\rm cut}$ is given by

$$M = \frac{4\pi\rho_{\rm M}}{3}\left(\frac{2\pi}{k_{\rm cut}}\right)^3 \simeq 7 \times 10^{10}\,h^{-1}\,M_{\rm sun} \times \left(\frac{16\,{\rm Mpc}^{-1}}{k_{\rm cut}}\right)^3\,. \tag{3.20}$$

It is important to examine if the halo abundance is compromised by the above-mentioned numerical artifacts. For $k_{\rm cut} = 16\,{\rm Mpc}^{-1}$, we see upturns in the mass functions at $M \sim 2 \times 10^9\,h^{-1}\,M_{\rm sun}$. This is owing to peculiar discreteness effects in hot/warm dark matter simulations [99, 100]. The critical halo mass (see Eq. (3.19)) is $M_{\rm c} \simeq 2 \times 10^9\,h^{-1}\,M_{\rm sun}$ for our simulation parameters $L = 10\,h^{-1}\,{\rm Mpc}$, $N = 512^3$ and $k_{\rm peak} \simeq 3\,{\rm Mpc}^{-1}$ (see Fig. 3.2). The estimated mass limit is indeed consistent with the upturn seen in the left panel of Fig. 3.4.

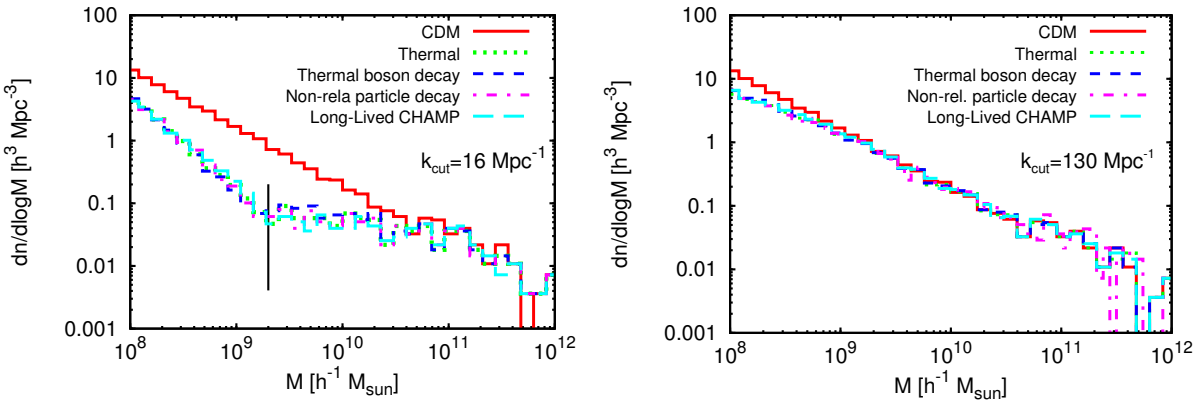

Figure 3.4: *The halo mass functions in the CDM model, in the three WDM models and in the Long-Lived CHAMP model with* $k_{\rm cut} = 16\,{\rm Mpc}^{-1}$ *(left panel) and with* $k_{\rm cut} = 130\,{\rm Mpc}^{-1}$ *(right panel). The upturn at the halo mass* $M \sim 2 \times 10^9\,h^{-1}\,M_{\rm sun}$ *(vertical line) in the left panel may be owing to the artificial objects due to the discreteness effects.*

distance from the center	$0-50$	$50-100$	$100-150$	$150-200$
number of satellites	19.7	15.62	8.08	14.16

Table 3.1: *The number of observed satellites in each* 50 kpc *from the center of our Milky Way. According to Polisensky and Ricotti [100], we count observed satellites known before the SDSS as one and those found by the SDSS as 3.54 due to the limited sky coverage of SDSS.*

Therefore, we conservatively restrict our discussion to halos with masses $M > M_{\rm c} = 2 \times 10^9\,h^{-1}\,M_{\rm sun}$ for $k_{\rm cut} = 16\,{\rm Mpc}^{-1}$. The number of halos at $M \sim M_{\rm c}$ in the three WDM models and in the Long-Lived CHAMP model is ~ 10 times smaller than that in the CDM model. Note the similarity of the halo abundances in the three WDM models and in the Long-Lived CHAMP model, as naively expected from the similarity in the linear matter power spectra.

In order to see if the WDM models and the Long-Lived CHAMP model resolve the "missing satellite problem", we select Milky Way-size halos with masses of $0.5 \times 10^{12}\,h^{-1}\,M_{\rm sun} < M_{\rm halo} < 1.5 \times 10^{12}\,h^{-1}\,M_{\rm sun}$ in our simulations. Although the halo mass of Milky Way itself is in debate (e.g. Ref. [101] and references therein), we take a relatively lower mass among suggested values. For a (slightly) small value of $M_{\rm halo}$, the relative mass ratio $M_{\rm satellite}/M_{\rm halo}$ becomes larger. Then the apparent discrepancy between the number of observed satellites and the simulated subhalo abundance at a given mass scale becomes smaller. We thus choose the small Milky Way mass as a "conservative" one.

We compare the cumulative subhalo mass functions averaged over the Milky Way-size halos in our five models in Fig. 3.5. Note that we see again an upturn for $k_{\rm cut} = 16\,{\rm Mpc}^{-1}$ around $M_{\rm sub}/M_{\rm host} \simeq 2 \times 10^{-3}$. Above the mass scale, where we can measure the mass function robustly, the subhalo abundance is suppressed by a factor of ~ 10 in the models with $k_{\rm cut} = 16\,{\rm Mpc}^{-1}$ (left panel) compared with the CDM model. For the models with $k_{\rm cut} = 130\,{\rm Mpc}^{-1}$ (right panel), the subhalo abundance is suppressed at most by a factor of ~ 2.

Let us now examine the radial distribution of the subhalos in our simulated Milky Way-size halos. We adopt the abundance of observed satellites in our Milky Way listed in Table 3.1. We account for the sky coverage of SDSS as follows. We count the number of the observed satellites in each 50 kpc bin such that each satellite known before the Sloan Digital Sky Survey (SDSS) is

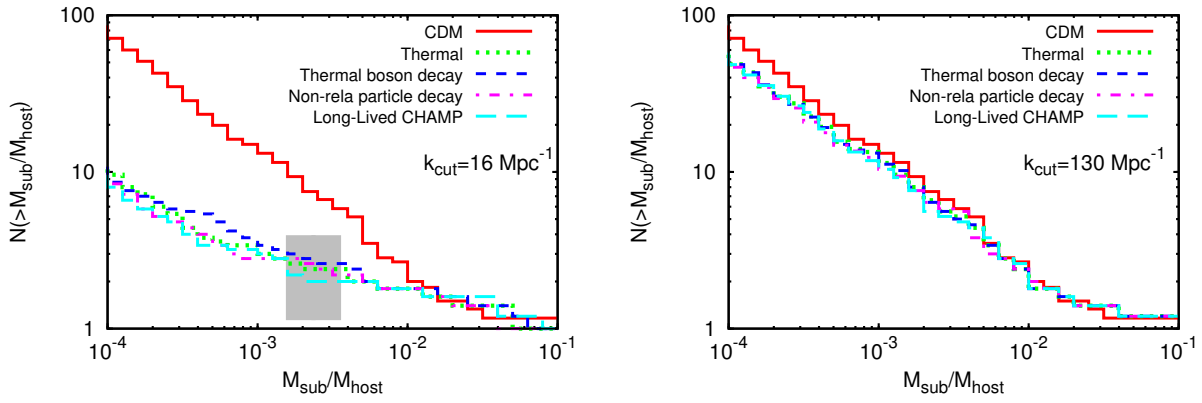

Figure 3.5: *The cumulative subhalo mass functions averaged over Milky Way-size halos in the CDM model, in the three WDM models and in the Long-Lived CHAMP model with* $k_{\rm cut} = 16\,{\rm Mpc}^{-1}$ *(left panel) and with* $k_{\rm cut} = 130\,{\rm Mpc}^{-1}$ *(right panel). The shaded region corresponds to the mass of nonlinear objects at which the upturn (numerical artifacts) occurs in halo mass function (see the vertical line in the left panel of Fig. 3.4).*

weighted as one whereas each satellite discovered by the SDSS is weighted as 3.54 [100].

In Fig. 3.6, we compare the averaged radial distributions of the subhalos in the Milky Way-size halos. The left panel shows the radial distribution in the CDM model and the right panel shows the radial distribution in the Thermal WDM model with $k_{\rm cut} \simeq 260\,{\rm Mpc}^{-1}$, which corresponds to $m_{3/2} \simeq 7\,{\rm keV}$ for the thermally-produced gravitino WDM. We include all the subhalos with $M > 2 \times 10^7\,h^{-1}\,M_{\rm sun}$. We also show variation of the radial distribution by thin solid lines. It should be noted that we set the gravitational softening length to be $1\,h^{-1}\,{\rm kpc}$. The subhalo count in the innermost bin could have been affected by the spatial resolution. We can see the CDM model predicts a larger number of subhalos by a factor of $2-10$ in each radial bin than observed. Note also that the number of satellites roughly scales with the host halo mass. Among the five Milky Way-size halos we selected, which have masses of $0.5\times10^{12}\,h^{-1}\,M_{\rm sun} < M_{\rm halo} < 1.5\times10^{12}\,h^{-1}\,M_{\rm sun}$, the total number of subhalos differs by a factor of ~ 3. By comparing the two panels in Fig. 3.6, we find that the radial distribution of subhalos in the Thermal WDM model with $k_{\rm cut} \simeq 260\,{\rm Mpc}^{-1}$ is similar to the one in CDM model and hence, the Thermal WDM model with $k_{\rm cut} \simeq 260\,{\rm Mpc}^{-1}$ does not seem to resolve the "missing satellite problem".

We plot the subhalo radial distribution in the Thermal WDM model with $k_{\rm cut} \simeq 16\,{\rm Mpc}^{-1}$ in Fig. 3.7. For this model, where the suppression of the subgalactic-scale structure is most significant, a sizeable fraction of subhalos have masses smaller than $M_{\rm c}$ (see Eq. (3.19)). Thus the number count in the radial distribution is likely unreliable. Note however that, even without discarding the small mass subhalos ($M_{\rm sub} < M_{\rm c}$), the subhalo abundance is slightly smaller than the observed satellites.

We plot the radial distributions of subhalos with masses $M > M_{\rm c} \simeq 10^8\,h^{-1}\,M_{\rm sun}$ in the Thermal WDM model with $k_{\rm cut} \simeq 130\,{\rm Mpc}^{-1}$ in Fig. 3.8. For this model, discarding small subhalos ($M_{\rm sub} < M_{\rm c} \simeq 10^8\,h^{-1}\,M_{\rm sun}$) reduces the subhalo abundance by a factor of ~ 2. Overall, the radial distribution of subhalos (after discarding) appears to reproduce the observed distribution.

Let us now examine closely the similarity of the three WDM models and the Long-Lived CHAMP model when the characteristic cut-off scale $k_{\rm cut}$ is kept the same. We compare the averaged radial distributions of the subhalos in these models for $k_{\rm cut} \simeq 130\,{\rm Mpc}^{-1}$ (again after discarding small subhalos) and for $k_{\rm cut} \simeq 260\,{\rm Mpc}^{-1}$ in Fig. 3.9. From Fig. 3.4, Fig. 3.5 and Fig. 3.9, we conclude that the similar cut-off scale in the linear matter power spectra yields also similar halo and

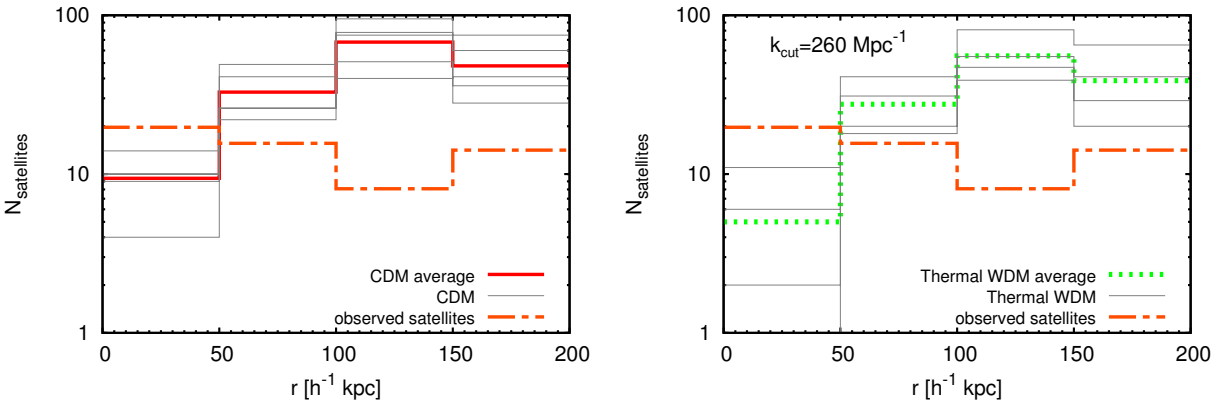

Figure 3.6: *The radial distributions of subhalos in Milky Way-size halos in the CDM model (left panel) and in the Thermal WDM models (right panel) with* $k_{\rm cut} \simeq 260\,{\rm Mpc}^{-1}$. *We divide the distance from the center of host halo in* 50 kpc *bins. Each thin line corresponds to the radial distribution in each Milky Way-size halo. Thick lines represent the average over the Milky Way-size halos. For comparison, we also plot the radial distribution of the observed satellites listed in Table 3.1.*

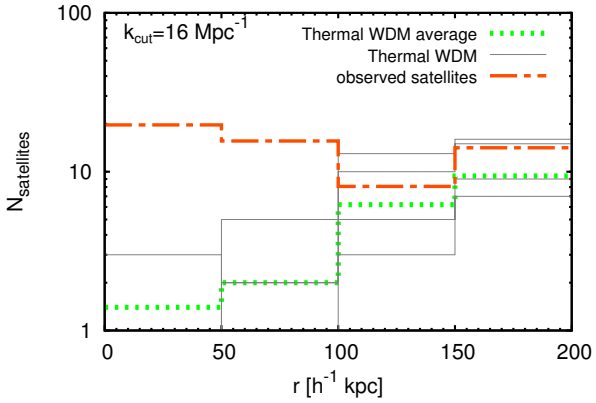

Figure 3.7: *The radial distribution of subhalos in Milky Way-size halo in the Thermal WDM model with* $k_{\rm cut} = 16\,{\rm Mpc}^{-1}$. *This subhalos may include the artificial small objects due to the discreteness effects.*

subhalo abundances and radial distributions.

3.3 Summary

In this chapter, we study the formation of non-linear objects in three WDM models and in a Long-Lived CHAMP model. We calculate the time evolution of the matter density fluctuations in the linear evolution regime by suitably modifying the public software `CAMB`. By using the obtained linear matter power spectra as initial conditions, we also perform large cosmological N-body simulations. The results are summarized as follows.

First, the comoving Jeans scale at the matter-radiation equality characterizes the linear matter power spectra of WDM models well. In the three WDM models motivated by particle physics, WDM particles are produced in different ways, but the linear matter power spectra with the same Jeans scale are very similar except for some difference at the damping tail at large k. We also

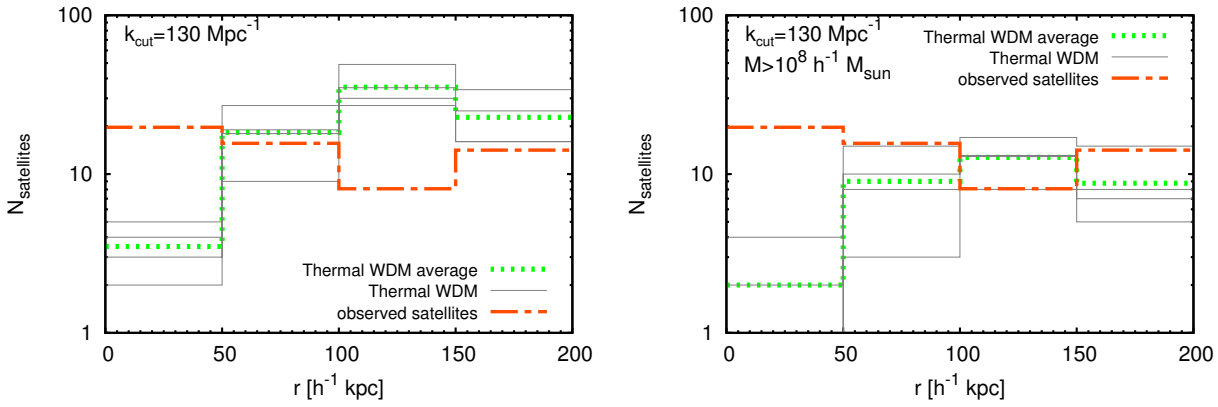

Figure 3.8: *The same plot as Fig. 3.7 in the Thermal WDM model with* $k_{\rm cut} = 130\,{\rm Mpc}^{-1}$. *After discarding small subhalos* ($M_{\rm sub} < M_{\rm c} \simeq 10^8\,h^{-1}\,M_{\rm sun}$), *the subhalo abundance is reduced by a factor of* ~ 2 *(right panel).*

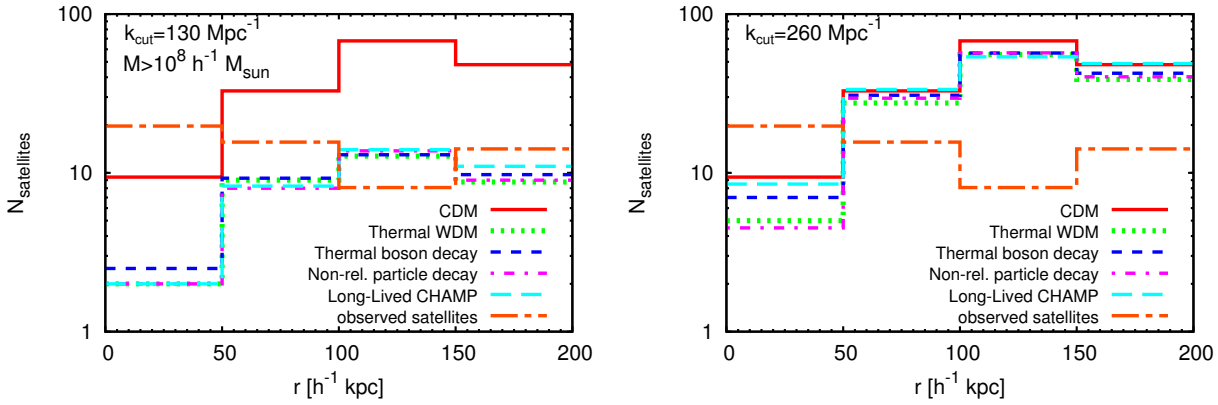

Figure 3.9: *Comparison of the averaged radial distributions in the CDM model, in the three WDM models and in the Long-Lived CHAMP model for* $k_{\rm cut} \simeq 130\,{\rm Mpc}^{-1}$ *(left panel) and for* $k_{\rm cut} \simeq 260\,{\rm Mpc}^{-1}$ *(right panel). For* $k_{\rm cut} \simeq 130\,{\rm Mpc}^{-1}$ *(left panel), we have discarded small subhalos* ($M_{\rm sub} < M_{\rm c} \simeq 10^8\,h^{-1}\,M_{\rm sun}$) *as in Fig. 3.8.*

consider a Long-Lived CHAMP model which has been suggested to yield a cut-off of the matter power spectrum through the "acoustic damping". The cut-off scale of the matter power spectrum in the Long-Lived CHAMP model is determined by the comoving horizon scale when CHAMP decays. We empirically find the correspondence of the cut-off scales $k_{\rm cut}$ (see Eq. (3.18)) between the three WDM models and the Long-Lived CHAMP model.

By performing large cosmological N-body simulations, we compare the abundances of nonlinear halos and subhalos and the radial distributions of the subhalos in Milky Way-size halos. The three WDM models and the Long-Lived CHAMP model produce very similar halo and subhalo mass functions and radial distributions if $k_{\rm cut}$ is kept the same. Therefore, we conclude that $k_{\rm cut}$ determines the clustering property of WDM and Long-Lived CHAMP well in both linear and non-linear growth of the matter density.

One might naively guess that our simulation results for small non-linear objects may be compromised by numerical effects. However, our conclusions are drawn after discarding small objects that are likely numerical artifacts. We also compare the subhalo radial distributions in Milky Way-

size halos with that of the observed satellites. We find that the WDM models and the Long-Lived CHAMP model are broadly consistent with the observation when they have $k_{\rm cut} \sim 20 - 260\,{\rm Mpc}^{-1}$. This cut-off scale corresponds to $m_{3/2} \sim 1 - 7\,{\rm keV}$ for the thermally-produced gravitino WDM and $\tau_{\rm Ch} \sim 0.01 - 2.5\,{\rm yr}$ for the Long-Lived CHAMP. Because there is significant variation of the subhalo abundance among host halos with different masses, as reported by Ishiyama et al. [102], it would be important to use a large sample of halos in order to address the validity of the models in a statistically complete manner.

Our results have a further implication for particles physics. We clarified how to put constraints on a few parameters of particles physics models which provide a WDM candidate. By calculating and comparing two quantities, the relic density of dark matter and the comoving Jeans scale at the matter-radiation equality, one can apply the reported constraints in a specific particle physics model (e.g. the mass of thermally-produced gravitino WDM or sterile neutrino WDM produced through the Dedelson & Widrow mechanism [72]) to virtually any model parameters of interest.

Finally, we note that the so-called astrophysical feedback processes are also thought to affect the abundance of luminous satellite galaxies [103]. Unfortunately, whether or not and how the baryonic processes changes our simple understanding based on the cut-off scale $k_{\rm cut} \sim 20 - 260\,{\rm Mpc}^{-1}$ is unclear due to the complexity of the baryonic processes. Regarding "missing satellite problem", both WDM and Long-Lived CHAMP models and the baryon feedback may explain the small number of the observed luminous satellites. The degeneracy can be resolved, in principle, by the direct probes of non-luminous small objects, by, for instance, future submillilensing surveys [91].

Chapter 4

Imprints of Non-thermal Wino Dark Matter on Small-Scale Structure

In this chapter, we consider the wino LSP dark matter scenario where the relic density of the wino is provided by the late time decays of the heavy gravitino [104, 105, 106, 107]. Due to the large mass hierarchy between the gravitino and the wino, the produced wino is more energetic than the thermal background. Thus, the wino LSP can be "warmer" than the conventional cold dark matter and leaves imprints on the small-scale structure if it does not lose its energy via the scattering processes with the thermal background. As we will show, a sizable fraction of the wino dark matter can be "warm" for the wino mass $m_{\tilde{w}} \simeq 100 - 500\,\mathrm{GeV}$. The imprints on the matter power spectra may provide further insights on the origin of dark matter via the future 21cm line survey [108, 109].

Here, we mention that the wino LSP scenario is now highly motivated after the discovery of a Higgs-like particle with a mass around 125 GeV at the LHC experiments [110, 111]. As is well known, the lightest Higgs boson mass is strongly interrelated to the sfermion masses [112, 113, 114, 115, 116] in the minimal supersymmetric standard model (MSSM). The observed Higgs boson mass around 125 GeV, then, suggests that the sfermion masses are in the tens to hundreds TeV range [112]. In the simplest supersymmetry breaking mediation mechanism, i.e. gravity mediation [117, 118, 119, 120, 121], such heavy sfermions are realized when the gravitino mass is in the tens to hundreds TeV range. The gaugino masses are, on the other hand, in a TeV range even for such a heavy gravitino when they are generated radiatively, which is expected when there is no singlet supersymmetry breaking field, i.e. the Polonyi field. The Polonyi field is disfavored from cosmology, since it causes the so-called Polonyi problem [122, 123]. Finally, the higgsino can be as heavy as the gravitino in "pure gravity mediation model" [124, 125, 126], where the so-called μ-term of the order of the gravitino mass is generated without use of the Polonyi field. Therefore, by assuming the simplest model based on the supergravity without the Polonyi field, the Higgs boson mass around 125 GeV naturally leads to the wino LSP scenario in the hundreds GeV range (see Refs. [125, 126] for details).

The organization of the chapter is as follows. In section 4.1, we summarize the wino LSP scenario mainly assuming the pure gravity mediation model, although our discussion can be applied for generic wino LSP scenarios. In section 4.2, we discuss the imprints on the small-scale structure of the wino dark matter produced non-thermally by the decays of the gravitino. The final section is devoted to conclusions.

4.1 The Wino LSP Scenario

4.1.1 Summary of the model

First, let us summarize the wino LSP scenario. To be specific, we base our arguments on the pure gravity mediation model [124, 125, 126], although the most of the following discussions can be applied to generic wino LSP scenarios with the heavy sfermions and higgsinos. [1]

In our setup, scalar fields in the MSSM obtain soft supersymmetry breaking masses via tree-level interactions in supergravity. With a generic Kähler potential, all the supersymmetry breaking masses of the scalar bosons are expected to be of the order of the gravitino mass, $m_{3/2}$. For simplicity, we assume that all the sfermions have the gravitino mass,

$$m_{\rm sfermion}^2 \simeq m_{3/2}^2 \ , \tag{4.1}$$

in the following discussions, although the details of the sfermion mass spectra do not change the discussions significantly. To account for a recently observed Higgs boson mass around 125 GeV, we take $m_{3/2}$ in tens to hundreds TeV range (see Refs. [125, 126] for example).

The higgsino mass, it is also generated through tree-level interactions in the pure gravity mediation model using the mechanism in Ref. [135]. As a result, the higgsino masses as well as the heavy Higgs boson masses are again of the order of the gravitino mass. It should be noted that a linear combination of the Higgs doublet bosons,

$$h \simeq \sin\beta\, H_u - \cos\beta\, H_d^* \ , \tag{4.2}$$

should be light so that it can play a role of the standard model Higgs boson, which requires fine-tuning between the Higgs mass parameters to some extent.

The gaugino masses are, on the other hand, dominated by loop suppressed contributions; the anomaly mediated contributions [136, 137, 138], and the contributions from the heavy higgsino threshold effect [104, 124, 136]. For $m_{3/2} = O(10-100)$ TeV, the resultant physical gaugino masses are given by,

$$m_{\tilde g} \simeq 2.5 \times (1 - 0.13\,\delta_{32} - 0.04\,\delta_{\rm SUSY}) \times 10^{-2}\, m_{3/2}, \tag{4.3}$$

$$m_{\tilde w} \simeq 3.0 \times (1 - 0.04\,\delta_{32} + 0.02\,\delta_{\rm SUSY}) \times 10^{-3}\, (m_{3/2} + L), \tag{4.4}$$

$$m_{\tilde b} \simeq 9.6 \times (1 + 0.01\,\delta_{\rm SUSY}) \times 10^{-3}\, (m_{3/2} + L/11), \tag{4.5}$$

where the subscripts $\tilde g$, $\tilde w$ and $\tilde b$ denote the gluino, the wino and the bino, respectively. Here, $\delta_{\rm SUSY} = \log[m_{\rm sfermion}/100\,{\rm TeV}]$, $\delta_{32} = \log[m_{3/2}/100\,{\rm TeV}]$ for the gluino mass, and $\delta_{32} = \log[(m_{3/2}+L)/100\,{\rm TeV}]$ for the wino mass. The terms proportional to $m_{3/2}$ in above formulae represent the anomaly mediated contributions, while those proportional to L are the higgsino threshold contributions. As discussed in Ref. [125, 126], the parameter L is of the order of the gravitino mass in the pure gravity mediation model, while L is expected to be small in the conventional anomaly mediation models. The above formulae show that the wino is the LSP for $|L| \lesssim 3m_{3/2}$.

[1] The pure gravity mediation model summarized below has many common features with the PeV-scale Supersymmetry [127], the G_2–MSSM [128], the Spread Supersymmetry [129], and the model with strong moduli stabilization [130]. The model also has a certain resemblance to the Split Supersymmetry [131, 132, 133], where the higgsino is assumed to be in the TeV scale. (See also [134] for discussions on the origin of the μ-term.) It should be noted that these models with heavy scalars require fine-tuning to some extent so that the weak scale is generated from the heavy scalar mass scales. In spite of this drawback, these models are now considered to be serious candidates of the MSSM, since they can explain the observed mass of the Higgs boson around 125 GeV and they provide a good candidate of dark matter, while they greatly ameliorate the flavor-changing neutral current problems and the CP-problems in the conventional MSSM at the TeV scale.

Before closing this section, we here summarize the important properties of the wino LSP which are relevant for the later discussion. First, the mass of the neutral component (the neutral wino LSP $\tilde{w}^0$) is degenerated with the one of its charged component (the charged wino $\tilde{w}^\pm$) due to the approximate custodial symmetry. The dominant mass splitting between the charged and the neutral winos comes from one-loop gauge boson contributions [139], which is given by

$$\Delta m_{\tilde{w}} = m_{\tilde{w}^\pm} - m_{\tilde{w}^0} = \frac{g_2^2}{16\pi^2} m_{\tilde{w}} \left[f(r_W) - \cos^2\theta_W f(r_Z) - \sin^2\theta_W f(0) \right], \tag{4.6}$$

where $f(r) = \int_0^1 dx (2+2x^2) \ln[x^2 + (1-x)r^2]$ and $r_{W,Z} = m_{W,Z}/m_{\tilde{w}}$. For the wino mass in the hundreds GeV range, the splitting is $\Delta m_{\tilde{w}} \simeq 160 - 170$ MeV. Due to the mass degeneracy, the dominant decay mode of the charged wino is the one into a neutral wino and a charged pion, $\tilde{w}^\pm \to \tilde{w}^0 + \pi^\pm$. Therefore, the charged wino has a rather long lifetime,

$$\tau_{w^\pm} \simeq 1.2 \times 10^{-10} \text{sec} \left(\frac{160\,\text{MeV}}{\Delta m_{\tilde{w}}} \right)^3 \left(1 - \frac{m_\pi^2}{\Delta m_{\tilde{w}}^2} \right)^{-1/2}. \tag{4.7}$$

As we will see in the following section, the charged wino produced by the gravitino decays loses most of its energy before it decays due to this long lifetime.

4.1.2 Relic density of the wino LSP

Both the self-annihilation and the co-annihilation with the charged winos are efficient at the freeze-out of the wino LSP. Due to its large annihilation cross section, the thermal relic number density of the wino LSP is suppressed, and hence, the wino mass consistent with the observed dark matter density is rather high. In fact, the thermal relic density, $\Omega^{(TH)}h^2$, in Ref. [140] shows that the observed dark matter density $\Omega^{(TH)}h^2 \simeq 0.11$ [28] is obtained for $m_{\tilde{w}} \simeq 2.7\,\text{TeV}$, while it is quickly decreasing for the lighter wino.

In the present scenario, we have another source of the wino LSP, the late time decays of the gravitino. After inflation, the gravitino is copiously produced from the thermal background and the resultant yield before its decay is roughly given by [141],

$$Y_{3/2} \simeq 1.9 \times 10^{-12} \left(\frac{T_R}{10^{10}\,\text{GeV}} \right), \tag{4.8}$$

where T_R is the reheating temperature of the Universe after inflation. The produced gravitino eventually decays into gauginos at a late time with a decay rate,

$$\begin{aligned} \Gamma_{3/2} &\simeq \frac{1}{32\pi}(8+3+1)\frac{m_{3/2}^3}{M_{\rm Pl}^2}, \\ &\simeq 1.8 \times 10^{-23}\,\text{GeV} \times \left(\frac{m_{3/2}}{100\,\text{TeV}} \right)^3, \end{aligned} \tag{4.9}$$

which corresponds to the cosmic temperature around

$$T_d \simeq 3.8\,\text{MeV} \times \left(\frac{m_{3/2}}{100\,\text{TeV}} \right)^{3/2}. \tag{4.10}$$

Here, $M_{\rm Pl} \simeq 2.44 \times 10^{18}$ GeV is the reduced Planck scale and we have defined the decay temperature by,

$$T_d = \left(\frac{10}{\pi^2 g_*} M_{\rm Pl}^2 \Gamma_{3/2}^2 \right)^{1/4}. \tag{4.11}$$

Here, $g_* \simeq 10.75$ is the effective number of the massless degrees of freedom at around the decay time. In the above decay width in Eq. (4.9), we have assumed that the gravitino decays into gauginos and all the other modes are closed. If there are additional decay modes into the squarks, the gravitino decay width becomes slightly larger, although it is in the same order of magnitude. It should be noted that the decay temperature of the gravitino is high enough not to spoil the success of the Big-Bang Nucleosynthesis for $m_{3/2} \gtrsim 30\,\mathrm{TeV}$ [142, 143, 144].

As the result of the late time decays of the gravitino, the wino LSP is non-thermally produced at around T_d which is lower than the freeze-out temperature of the wino LSP, and the resultant relic density is given by,

$$\Omega^{(NT)}h^2 \simeq 0.16 \times \left(\frac{m_{\tilde{w}}}{300\,\mathrm{GeV}}\right)\left(\frac{T_R}{10^{10}\,\mathrm{GeV}}\right) \ . \tag{4.12}$$

Altogether, the total relic density of the wino LSP is given by,

$$\Omega h^2 = \Omega^{(TH)}h^2 + \Omega^{(NT)}h^2 \ . \tag{4.13}$$

Thus, for $m_{\tilde{w}} \ll 2.7\,\mathrm{TeV}$, the observed dark matter density can be explained by the non-thermally produced wino for

$$T_R \simeq 7 \times 10^9\,\mathrm{GeV} \times \left(\frac{300\,\mathrm{GeV}}{m_{\tilde{w}}}\right)\left(\frac{\Omega h^2}{0.11}\right) \ . \tag{4.14}$$

Interestingly, the required reheating temperature is consistent with the successful leptogenesis [145, 146, 147], $T_R \gtrsim 2 \times 10^9\,\mathrm{GeV}$, for $m_{\tilde{w}} \lesssim 1\,\mathrm{TeV}$. In the following analysis, we focus on the wino mass below a TeV where the non-thermally produced wino is the dominant component of dark matter.

Several comments are in order. First, it should be noted that the entropy produced by the decay of the gravitino is negligible since the energy density of the gravitino at the decay time is subdominant.[2] Second, it should be also noted that the annihilation of the wino after the non-thermal production is negligible, since the yield of the non-thermally produced wino is small enough, i.e.

$$Y_{\tilde{w}}^{(NT)} = Y_{3/2} \ll \sqrt{\frac{45}{8\pi^2 g_*}}\frac{1}{\langle\sigma v\rangle M_{\mathrm{Pl}} T_d} \simeq 2.9 \times 10^{-10} \times \left(\frac{10^{-24}\mathrm{cm}^3/\mathrm{s}}{\langle\sigma v\rangle}\right)\left(\frac{4\,\mathrm{MeV}}{T_d}\right) \ . \tag{4.15}$$

4.1.3 Collider/Indirect dark matter search constraints

The gluino and the wino masses in the pure gravity mediation model are constrained by the collider experiments and indirect dark matter searches. Currently, the most severe limit on the gluino mass is obtained from an inclusive SUSY search at the LHC experiment with use of multi-jets plus missing transverse energy events. According to the search, the gluino mass is constrained to be $m_{\tilde{g}} > 1.2\,(1.0)\,\mathrm{TeV}$ for the wino mass of $100\,(500)\,\mathrm{GeV}$ [148], as shown in Fig. 4.1. In near future, the limit will be increased up to about 2 TeV when the LHC experiment succeeds to accumulate $300\,\mathrm{fb}^{-1}$ data at the 14 TeV running. Furthermore, with utilizing disappearing charged tracks caused by the long-lived charged winos, the limit will be increased up to about 2.3 TeV if standard model backgrounds against the signal are efficiently reduced [149]. The search of the displaced vertex made by the gluino decay can also provide significant hints on the models with heavy scalars

[2] In the non-thermal wino production scenario via the decay of moduli fields, a large amount of entropy is produced, and hence, the baryon asymmetry is highly diluted. Therefore, those scenarios require baryogenesis below the decay temperature of the moduli fields.

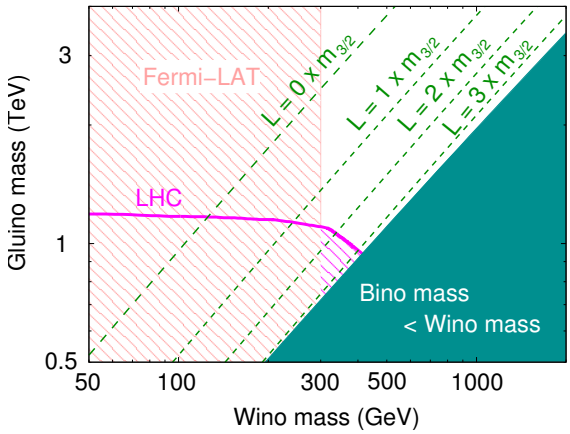

Figure 4.1: *Constraints on the gluino and the wino masses in the pure gravity mediation model. Limits on the gluino mass obtained from the LHC experiment (8 TeV & 6 fb^{-1} data) and on the wino mass from the Fermi-LAT experiment (observation of γ-rays from dwarf spheroidal galaxies) are shown as hatched regions. The shaded region is not favored because the LSP is the bino which leads to the over-closure of the Universe.*

where the gluino decay rate is strongly suppressed by the mass of the heavy scalars [150, 151, 152]. In the simplest models such as the pure gravity mediation models, for example, the ratio between the gluino mass and the squark masses are fixed by the anomaly mediation relation, with which the scalar masses are not heavy enough to suppress the gluino decay rate down to the one which allows the displaced vertex search. In more relaxed models such as the ones in Refs. [129, 131, 132, 133], on the other hand, the scalar masses can be much heavier than the gravitino mass with which the gluino decay is highly suppressed. Therefore, we might be able to distinguish heavy scalar scenarios through the search of the displaced vertex of the gluino decay.

The most severe limit on the wino mass is obtained from the indirect detection measurement of dark matter using gamma-rays from dwarf spheroidal galaxies (Milky-way satellites) at the Fermi-LAT experiment [153]. At present, the limit is $m_{\tilde{w}} > 300\,\mathrm{GeV}$, which is also shown in Fig. 4.1. Very recently, it has also been suggested that the observation of gamma-rays from our galactic center gives a more stringent limit on the annihilation cross section of dark matter with use of the Fermi-LAT data [154]. According to this analysis, the wino mass will be constrained as $m_{\tilde{w}} > 500\,\mathrm{GeV}$, while this results depend on the assumed background model. In future, the indirect detection measurement of dark matter using cosmic-ray anti-protons at the AMS-02 experiment will give a stringent limit on the wino mass. With a few years of data taking, the limit will be increased, at least, up to 1 TeV [155]. The LHC experiment will also provide an opportunity to directly search for the wino dark matter in near future. Using the pair production of the wino associated with a jet through electroweak interactions and utilizing the disappearing track of the charged wino [124, 139, 156], the limit on the wino mass is expected to be increased up to 500 GeV, though the limit is currently very mild as $m_{\tilde{w}} > 100\,\mathrm{GeV}$, as reported in reference [157].

4.2 Imprints on the Small-Scale Structure

Now, let us discuss possible imprints on the small-scale structure of the non-thermally produced wino dark matter. For that purpose, we discuss the energy distribution of the neutral wino in detail. As we will see, a sizable fraction of the neutral wino keeps its energy from the scattering process with the thermal background, which leads to a rather small free-streaming scale of the wino

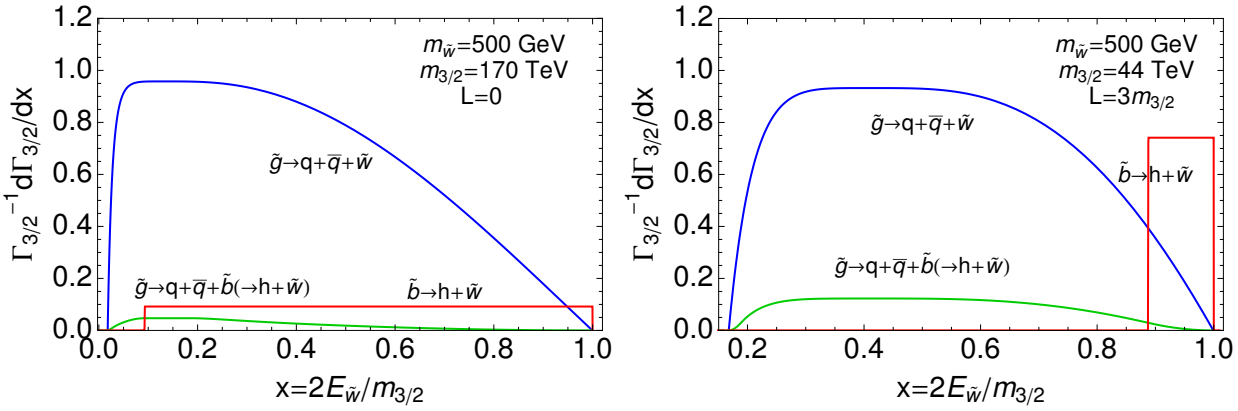

Figure 4.2: *The energy distribution of the wino produced by the cascade decays of the gravitino for given $m_{\tilde{w}}$ and L. We have taken $m_{\tilde{w}} = 500\,\mathrm{GeV}$, $L = 0$ (left panel) and $L = 3m_{3/2}$ (right panel), $\arg[m_{\tilde{w}}/m_{\tilde{g}}] = \pi$ and $\arg[m_{\tilde{b}}/m_{\tilde{g}}] = \pi$.*

dark matter which can be observed in the future 21cm line survey.

4.2.1 The wino energy distribution at the gravitino decay

First, let us calculate the energy distribution of the wino produced by the decays of the gravitino. The gravitino decays into the wino through two-body decay modes. In addition, the gravitino decays into the wino through the modes into heavier gauginos, i.e. the gluino and the bino.[3] The wino has a line spectrum at the energy $E_{\tilde{w}} \simeq m_{3/2}/2$ from the two-body decay and continuous spectra from the cascade decays which lead to the energy distribution,

$$\begin{aligned}\frac{1}{\Gamma_{3/2}}\frac{d\Gamma_{3/2}}{dE_{\tilde{w}}} &= \frac{8}{12}\left\{\frac{Br_{\tilde{g}\to\tilde{w}}}{\Gamma_{\tilde{g}\to\tilde{w}}}\frac{d\Gamma_{\tilde{g}\to\tilde{w}}}{dE_{\tilde{w}}} + \int dE_{\tilde{b}}\,\frac{Br_{\tilde{g}\to\tilde{b}}}{\Gamma_{\tilde{g}\to\tilde{b}}}\frac{d\Gamma_{\tilde{g}\to\tilde{b}}}{dE_{\tilde{b}}}\frac{1}{\Gamma_{\tilde{b}\to\tilde{w}}}\frac{d\Gamma_{\tilde{b}\to\tilde{w}}}{dE_{\tilde{w}}}\right\} \\ &\quad + \frac{1}{12}\left\{\frac{1}{\Gamma_{\tilde{b}\to\tilde{w}}}\frac{d\Gamma_{\tilde{b}\to\tilde{w}}}{dE_{\tilde{w}}}\right\} + \frac{3}{12}\delta(E_{\tilde{w}} - m_{3/2}/2)\ . \end{aligned} \tag{4.16}$$

Here, Γ's and Br's denote the decay rates and the branching ratios of the gauginos which are given in appendix B. The first and the third terms are the spectra from the cascade decays of $\tilde{G} \to \tilde{g} \to \tilde{w}$ and $\tilde{G} \to \tilde{b} \to \tilde{w}$ respectively, and the second term is the spectrum from a cascade decay of $\tilde{G} \to \tilde{g} \to \tilde{b} \to \tilde{w}$.

In Fig. 4.2, we show the energy distribution of the wino produced by the cascade decays of the gravitino for given $m_{\tilde{w}}$ and L. In the figure, we have taken $m_{\tilde{w}} = 500\,\mathrm{GeV}$ and $L = 0$ (left panel) and $L = 3m_{3/2}$ (right panel). Here, we have taken $\arg[m_{\tilde{w}}/m_{\tilde{g}}] = \pi$ and $\arg[m_{\tilde{b}}/m_{\tilde{g}}] = \pi$, although the effects of the relative phases to our estimation of possible imprints on the small-scale structure of the non-thermally produced wino dark matter are negligible (see the following discussions). The figure shows that the peak of the wino energy distribution can be much smaller than the $m_{3/2}/2$ and has a low energy tail.

Notice that the peak position is higher for $L = 3m_{3/2}$ for a given gravitino mass. This is because the wino mass is closer to the gluino mass for $L = 3m_{3/2}$ than in the case of $L = 0$, and hence, the wino carries away most of the gluino energy. For a given wino mass, on the contrary, the energy of the wino is softer for $L = 3m_{3/2}$ than the one for $L = 0$, since the gravitino mass is smaller for a larger L.

[3] As we have mentioned above, we assume that all the decay modes of the gravitino into the sfermions and the higgsinos are closed.

4.2.2 Scattering processes with the thermal background

The energetic winos produced by the decays of the gravitinos lose their energy through interactions with the thermal background, which consists of the electrons and positrons (e) and the neutrinos (ν_l, $l = e, \mu, \tau$) at the cosmic temperature of interest, $T \sim 0.5 - 100\mathrm{MeV}$. In Refs. [80, 158], they study the interaction rates of the winos with the thermal background in detail. In this subsection, we summarize the relevant interactions for our purpose.

The charged winos mainly lose their energy via the Coulomb scattering with electrons and positrons in the thermal background. The energy loss rate at the cosmic temperature T takes the form [159],

$$-\frac{dE_{\tilde{w}^\pm}}{dt} = \frac{\pi\alpha^2 T^2}{3}\Lambda\left(1 - \frac{m_{\tilde{w}}^2}{2E_{\tilde{w}^\pm}^2}\ln\left(\frac{E_{\tilde{w}^\pm} + p_{\tilde{w}^\pm}}{E_{\tilde{w}^\pm} - p_{\tilde{w}^\pm}}\right)\right) \tag{4.17}$$

with the fine-structure constant α and the Coulomb logarithm $\Lambda \sim O(1)$. Here, $E_{\tilde{w}^\pm}$ and $p_{\tilde{w}^\pm}$ are the physical energy and the physical momentum of the charged wino. The charged winos also turn into neutral winos by the decay of $\tilde{w}^\pm \to \tilde{w}^0 + \pi^\pm$ and the inelastic scattering of $\tilde{w}^\pm + e\,(\nu_e) \to \tilde{w}^0 + \nu_e\,(e)$. The decay is dominant [158] at the cosmic temperature of interest, and we neglect the inelastic scattering in the following. The average ratio of energy lost within one lifetime is given by,

$$\begin{aligned}\frac{\Delta E_{\tilde{w}^\pm}}{E_{\tilde{w}^\pm}}\Big|_{1-\mathrm{lifetime}} \simeq \quad & 97\Lambda\left(1 - \frac{m_\pi^2}{\Delta m_{\tilde{w}}^2}\right)^{-1/2}\left(\frac{T}{1\,\mathrm{MeV}}\right)^2\left(\frac{160\,\mathrm{MeV}}{\Delta m_{\tilde{w}}}\right)^3\left(\frac{100\,\mathrm{GeV}}{m_{\tilde{w}}}\right) \\ & \times\left(1 - \frac{m_{\tilde{w}}^2}{2E_{\tilde{w}^\pm}^2}\ln\left(\frac{E_{\tilde{w}^\pm} + p_{\tilde{w}^\pm}}{E_{\tilde{w}^\pm} - p_{\tilde{w}^\pm}}\right)\right)\,.\end{aligned} \tag{4.18}$$

The charged winos lose most of their energy within one lifetime due to their long lifetime. Thus, the neutral winos produced via the decay of the charged winos are "cold". Since the gravitino decays into the neutral and charged wino equally, at least two-thirds of dark matter particles are "cold".

The neutral wino does not have any elastic energy loss process at the tree level since we assume the $\mu-$parameter, the $B-$parameter and the sfermion masses are as large as the gravitino mass. Thus, the neutral winos can lose their energy via the elastic scattering at loop level and the inelastic scattering of $\tilde{w}^0 + e\,(\nu_e) \to \tilde{w}^\pm + \nu_e\,(e)$. We consider the elastic scattering at the one-loop level and study it in detail in appendix B.3. The rates of these processes are given by,

$$\Gamma_{\tilde{w}^0,\,\mathrm{elastic}} = \frac{135}{\pi^3}\zeta(5)g_{\mathrm{loop}}^2\left(\frac{m_W^2}{m_{\tilde{w}}^2}\right)G_F^4 T^5 m_W^4\frac{E_{\tilde{w}^0}^2}{m_{\tilde{w}}^2}\left(1 + \frac{p_{\tilde{w}^0}^2}{E_{\tilde{w}^0}^2}\right)\,, \tag{4.19}$$

$$\begin{aligned}\Gamma_{\tilde{w}^0,\,\mathrm{inelastic}} = & \frac{8}{\pi^3}G_F^2 T^5\frac{(E_{\tilde{w}^0} + p_{\tilde{w}^0})^4}{m_{\tilde{w}}^2 E_{\tilde{w}^0} p_{\tilde{w}^0}}\left(6 + 2\frac{m_{\tilde{w}}}{E_{\tilde{w}^0} + p_{\tilde{w}^0}}\frac{\Delta m_{\tilde{w}}}{T}\right) \\ & \times\exp\left(-\frac{m_{\tilde{w}}}{E_{\tilde{w}^0} + p_{\tilde{w}^0}}\frac{\Delta m_{\tilde{w}}}{T}\right)\end{aligned} \tag{4.20}$$

with the Riemann zeta function $\zeta(x)$, the Fermi constant G_F and the mass of the weak boson m_W. Here, $E_{\tilde{w}^0}$ and $p_{\tilde{w}^0}$ are the physical energy and the physical momentum of the neutral wino. The function $g_{\mathrm{loop}}(x)$ is given in appendix B.3. Notice that the last factor of the inelastic scattering rate in the above expression represents the Boltzmann suppression. In Fig. 4.3, we plot the reaction rates normalized by the Hubble parameter. The figure shows that the inelastic scattering become inefficient quickly at low temperature by the Boltzmann suppression, but in the relevant region of the cosmic temperature in which $\Gamma/H \gg 1$, the inelastic scattering dominates the elastic scattering.

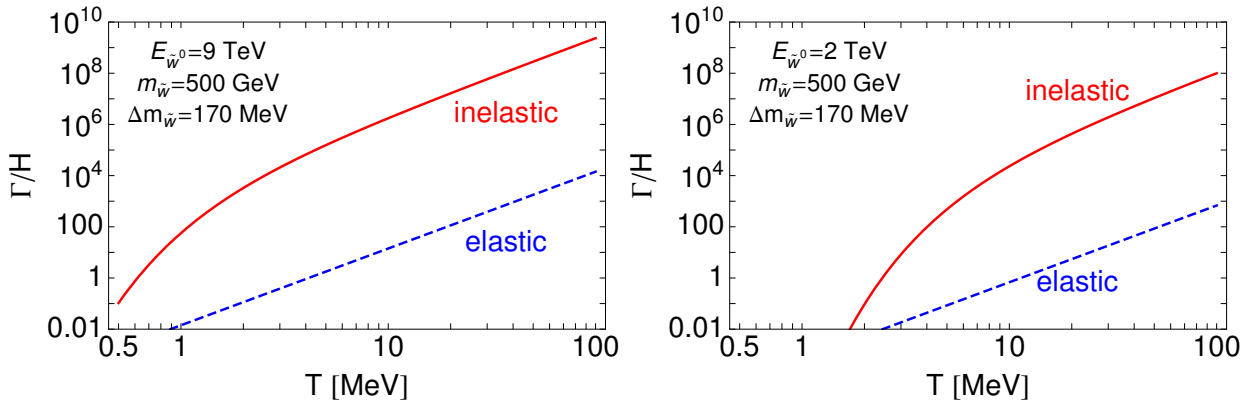

Figure 4.3: *The reaction rates of the neutral wino normalized by Hubble parameter as functions of the cosmic temperature. Here, we plot the reaction rates of the inelastic scattering (solid lines) and the elastic scattering (dashed lines), taking* $m_{\tilde{w}} = 500\,\mathrm{GeV}$ *and* $\Delta m_{\tilde{w}} = 170\,\mathrm{MeV}$ *for both* $E_{\tilde{w}^0} = 9\,\mathrm{TeV}$ *(left panel) and* $E_{\tilde{w}^0} = 2\,\mathrm{TeV}$ *(right panel).*

The inelastic scattering rate is higher for more energetic neutral winos since the inelastic scattering originates from the higher dimensional operator, and moreover, more energetic neutral wino can overcome the mass splitting between the charged and the neutral wino more easily.

Once the neutral winos turn into charged winos by the inelastic scattering, the charged winos lose most of their energy by the Coulomb scattering with the thermal background and turn back into neutral winos as discussed above. Therefore, the energetic neutral winos produced by the decays of the gravitinos become "warm" only if they are directly produced by the decays of the gravitinos and they do not undergo the inelastic scattering since then. We call such neutral wino the "warm" neutral wino and other neutral wino the "cold" neutral wino in the following.

4.2.3 The present momentum distribution of the "warm" neutral wino

Now we describe the Boltzmann equation which determines the time evolution of the momentum distribution of the "warm" neutral wino $f_{\mathrm{w}}(p_{\mathrm{w}}, t)$ where p_{w} and t denote the physical momentum of the "warm" neutral wino and the cosmic time. Throughout this chapter, we normalize the momentum distribution of the "warm" neutral wino by the present number density of the whole wino dark matter. Following the discussion of the previous subsections, the Boltzmann equation of the "warm" neutral wino does not depend on the charged wino or the "cold" neutral wino and takes the form,

$$\begin{aligned} &\frac{\partial}{\partial t} f_{\mathrm{w}}(p_{\mathrm{w}}, t) - H p_{\mathrm{w}} \frac{\partial}{\partial p_{\mathrm{w}}} f_{\mathrm{w}}(p_{\mathrm{w}}, t) \\ &\quad = \frac{1}{3} \frac{d\Gamma_{3/2}}{d^3 p_{\mathrm{w}}} \frac{a(t_0)^3}{a(t)^3} e^{-\Gamma_{3/2} t} - \Gamma_{\tilde{w}^0,\,\mathrm{inelastic}}\, f_{\mathrm{w}}(p_{\mathrm{w}}, t) \end{aligned} \tag{4.21}$$

where $a(t)$ is the scale factor and t_0 is the present time. Here, $d\Gamma_{3/2}/d^3 p_{\mathrm{w}}$ relates to $d\Gamma_{3/2}/dE_{\mathrm{w}}$ as

$$\frac{4\pi p_{\mathrm{w}}^2}{(2\pi)^3} \frac{E_{\mathrm{w}}}{p_{\mathrm{w}}} \frac{d\Gamma_{3/2}}{d^3 p_{\mathrm{w}}} = \frac{d\Gamma_{3/2}}{dE_{\mathrm{w}}} \tag{4.22}$$

where E_{w} denote the physical energy of the "warm" neutral wino. In the Boltzmann equation of the "warm" neutral wino, we have ignored the thermal motion of the gravitinos since the gravitinos are sufficiently nonrelativistic at the decay time.

By solving the Boltzmann equation numerically, we obtain the present momentum distribution of the "warm" neutral wino $f_{\rm w}(p_{\rm w}, t_0)$. It should be noted that at the present time, $p_{\rm w}$ equals the comoving momentum of the "warm" neutral wino. In the lower panels of Fig. 4.4, we plot the present momentum distribution of the "warm" neutral wino for the same parameters as in Fig. 4.2. For comparison, in the upper panels we also plot the present momentum distribution of the "warm" neutral wino obtained by solving the Boltzmann equation without the inelastic scattering term, i.e. letting $\Gamma_{\tilde{w}^0,\,\rm inelastic} = 0$. When we ignore the inelastic scattering of the neutral wino, we can estimate the typical comoving momentum of the "warm" neutral wino as,

$$p_{\rm w,\,typical}(t_0) = p_{\rm cm}\, a(t_d)/a(t_0) \tag{4.23}$$

where $p_{\rm cm}$ is the center-of-mass momentum and t_d is the time of the gravitino decay, at which $T = T_d$. In the present scenario, noting $p_{\rm cm} \simeq m_{3/2}/2$ and $a(t_d)/a(t_0) \simeq (4/11)^{1/3}\, T_0/T_d$ where T_0 is the present temperature of the cosmic microwave background, the typical present momentum of the "warm" neutral wino is given by,

$$p_{\rm w,\,typical}(t_0) \simeq 2.1 \times 10^{-6}\,{\rm GeV} \times \left(\frac{m_{3/2}}{100\,{\rm TeV}}\right)^{-1/2} . \tag{4.24}$$

The typical present momentum of the "warm" neutral wino is larger for smaller gravitino mass due to later decays of lighter gravitino and we can see this relation in the upper panels of Fig. 4.4. When we consider the inelastic scattering of the neutral wino, the inelastic scattering turns a part of the neutral winos produced by the decays of the gravitinos into the "cold" neutral winos. In particular, almost all of the neutral winos that are produced by the cascade decay of $\tilde{G} \to \tilde{b} \to \tilde{w}$ and the direct decay of $\tilde{G} \to \tilde{w}$ turn into the "cold" neutral winos, because the winos produced by these decay modes are more energetic than the winos produced by the cascade decays of $\tilde{G} \to \tilde{g} \to \tilde{w}$ and $\tilde{G} \to \tilde{g} \to \tilde{b} \to \tilde{w}$ as we can see in Fig. 4.2. The present abundance of softer "warm" neutral winos as well as harder "warm" neutral winos is reduced when we consider the inelastic scattering. This is because softer "warm" neutral winos are produced at the higher redshift, when the inelastic scattering rate is higher.

4.2.4 The ratio of the "warm" neutral wino and the free-streaming scale of the wino dark matter

According to the current understanding of the cosmology, the structure formation of the Universe occurs as a result of the mutual evolution of the primordial fluctuations of the gravitational potential and of the dark matter energy density. Since the "warm" neutral winos have high-velocity and can clime over the gravitational potential, they do not contribute to the structure formation of the Universe and reduce the power spectrum of the matter density fluctuations in comparison with the ΛCDM model.

When we discuss the imprints on the structure formation of the wino dark matter, we consider two indices. One is the ratio of the "warm" neutral wino to the whole wino dark matter, $r_{\rm warm}$. Smaller value of $r_{\rm warm}$ indicates smaller imprints on the matter power spectrum. Another is the free-streaming scale which is defined as the comoving Jeans scale at the matter-radiation equality time and it takes the form,

$$k_{\rm fs} = a \sqrt{\frac{4\pi G \rho_{\rm mat}}{\langle v^2 \rangle}}\bigg|_{a=a_{\rm eq}} \tag{4.25}$$

where $G = (8\pi M_{\rm Pl}^2)^{-1}$, $\rho_{\rm mat}$ and $\langle v^2 \rangle$ are the gravitational constant, the matter energy density of the Universe and the mean square of the velocity of dark matter, respectively. The primordial

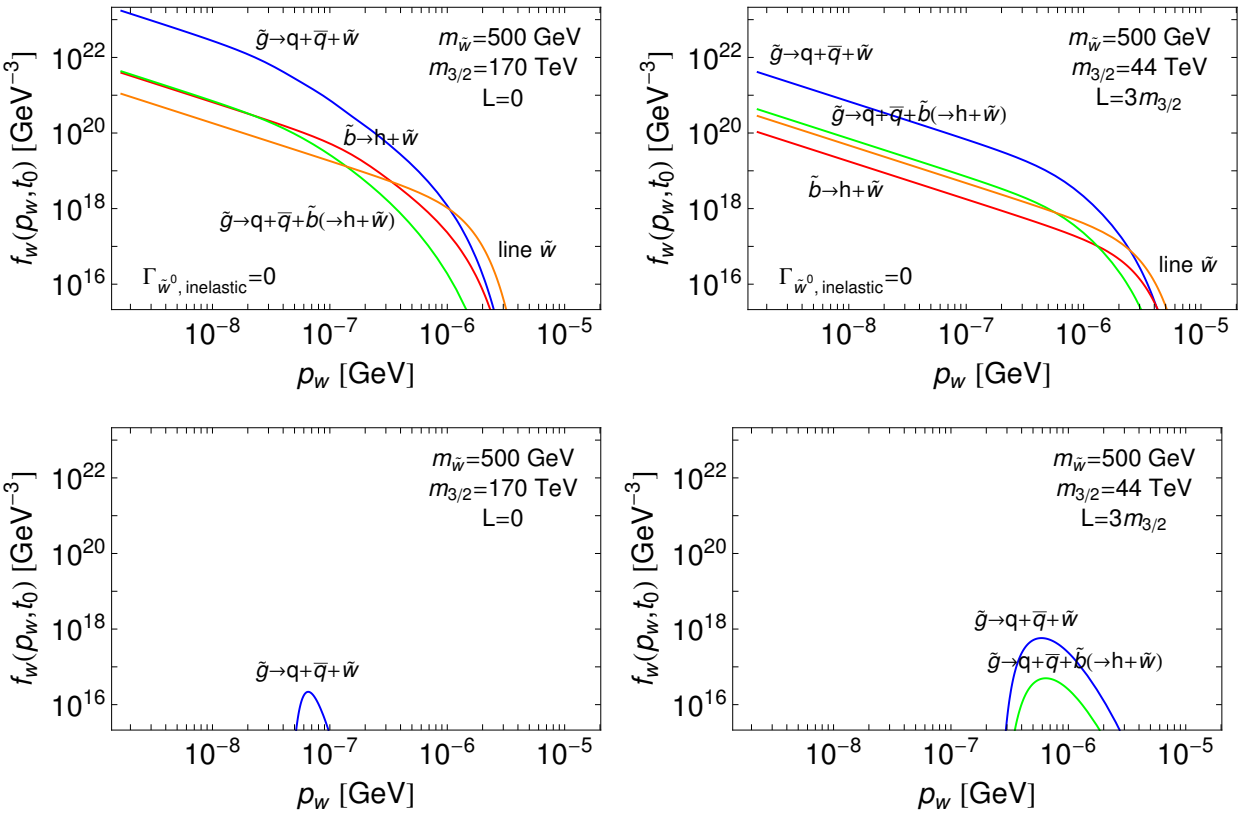

Figure 4.4: *The present momentum distribution of the "warm" neutral wino (lower panels). We also plot the present momentum distribution obtained by solving the Boltzmann equation without the inelastic scattering term for comparison (upper panels). Here, we have taken $m_{\tilde{w}} = 500\,\mathrm{GeV}$, $L = 0$ (left panels) and $L = 3m_{3/2}$ (right panels) as in Fig. 4.2.*

fluctuations with the wavenumber above the free-streaming scale hold the imprints of the "warm" natural wino. In the conventional warm dark matter scenario, which is suggested as a solution of the so-called "small-scale crisis" [35, 34, 33], the ratio of the warm dark matter to the whole dark matter of the Universe is assumed to be one and the free-streaming scale is assumed to be around $100\,\mathrm{Mpc}^{-1}$ [79]. In the present wino dark matter scenario, however, r_{warm} does not exceed one-third, and hence, the wino dark matter is not the conventional warm dark matter.

We calculate these two indices using the momentum distributions obtained in the previous subsection (see Fig. 4.4) and summarize the results in Table. 4.1. In this table, we also show the results obtained by ignoring the inelastic scattering of the neutral wino, $\Gamma_{\tilde{w}^0,\,\mathrm{inelastic}} = 0$, in the parentheses. We can confirm that the ratio of the "warm" neutral winos to the whole wino dark matter is one-third when we ignore the inelastic scattering as mentioned above. For $L = 3m_{3/2}$ the value of r_{warm} is smaller and the value of k_{fs} is larger, which indicates that the wino dark matter is "colder" than in the case of $L = 0$. This is because for heavier gravitino the value of $p_{\mathrm{w,\,typical}}(t_0)$ is smaller and the value of $\Gamma_{\tilde{w}^0,\,\mathrm{inelastic}}$ is larger.

In order to discuss the imprints on the matter power spectrum in the present scenario, we plot the values of r_{warm} (left panel) and k_{fs} (right panel) as functions of the wino mass $m_{\tilde{w}}$ for $L = 0, m_{3/2}, 2m_{3/2}, 3m_{3/2}$ in Fig. 4.5. Since larger value of L means smaller gravitino mass for a given wino mass, the wino dark matter for larger value of L is "warmer" as we can see in the figure.

In the above discussion of this section, we have taken the relative phases between the gaugino

Table 4.1: *The ratio of the "warm" neutral wino to the whole wino dark matter* $r_{\rm warm}$ *and the free-streaming scale of the wino dark matter* $k_{\rm fs}$*, for* $m_{\tilde{w}} = 500\,GeV$ *and* $L = 0$ *and* $L = 3m_{3/2}$ *as in Fig. 4.2. We also show the results for* $\Gamma_{\tilde{w}^0,\,\rm inelastic} = 0$ *in the parentheses.*

parameters	$r_{\rm warm}$	$k_{\rm fs}\,[{\rm Mpc}^{-1}]$
$m_{\tilde{w}} = 500\,{\rm GeV},\ m_{3/2} = 170\,{\rm TeV},\ L = 0$	$1.5 \times 10^{-7}\,(0.33)$	$4.5 \times 10^{7}\,(2.7 \times 10^{3})$
$m_{\tilde{w}} = 500\,{\rm GeV},\ m_{3/2} = 44\,{\rm TeV},\ L = 3m_{3/2}$	$0.016\,(0.33)$	$7.5 \times 10^{3}\,(1.2 \times 10^{3})$

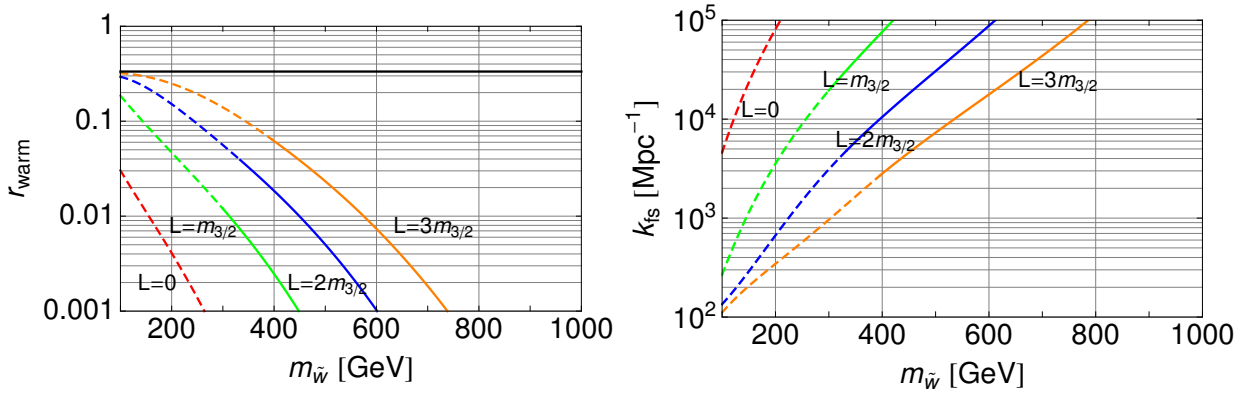

Figure 4.5: *The ratio of the "warm" neutral wino to the whole wino dark matter* $r_{\rm warm}$ *(left panel) and the free-streaming scale of the wino dark matter* $k_{\rm fs}$ *(right panel) as functions of the wino mass* $m_{\tilde{w}}$ *for* $L = 0, m_{3/2}, 2m_{3/2}, 3m_{3/2}$*. The regions shown by the dashed lines are not favored by the collider experiments and by the indirect detection searches.*

mass parameters, $\arg[m_{\tilde{w}}/m_{\tilde{g}}] = \pi$ and $\arg[m_{\tilde{b}}/m_{\tilde{g}}] = \pi$. We have also fixed the relation between the gaugino masses and the graviton mass, which are determined by given $m_{\tilde{w}}$ and L in the present scenario. Now, we vary the values of $\arg[m_{\tilde{w}}/m_{\tilde{g}}]$, $\arg[m_{\tilde{b}}/m_{\tilde{g}}]$, $m_{\tilde{b}}$ and $m_{\tilde{g}}$ to see their effects on the values of $r_{\rm warm}$ and $k_{\rm fs}$. In Fig. 4.6, we plot the values of $r_{\rm warm}$ (left panel) and $k_{\rm fs}$ (right panel) for various values of $\arg[m_{\tilde{w}}/m_{\tilde{g}}]$, $\arg[m_{\tilde{b}}/m_{\tilde{g}}]$ (dotted lines), $m_{\tilde{b}}$ (dashed lines) and $m_{\tilde{g}}$ (dot dashed lines). In the figure, we have taken $L = 3m_{3/2}$. The figure shows the effects of the relative phases between the gaugino mass parameters, $\arg[m_{\tilde{w}}/m_{\tilde{g}}]$ and $\arg[m_{\tilde{b}}/m_{\tilde{g}}]$ are at most 10 % and thus negligible. We can also see the effects of the bino mass $m_{\tilde{b}}$ are small. On the other hand, larger gluino mass $m_{\tilde{g}}$ significantly enhances the value of $r_{\rm warm}$ and reduces the value of $k_{\rm fs}$ and thus makes the wino dark matter "warmer". This is because the wino carries away smaller fraction of the gluino energy for larger mass difference between the gluino and the wino. Therefore, in other models where the gluino mass for a given wino mass is lager than in the present model, the imprints on the matter power spectra are enhanced.

As we have seen above, the wino dark matter is the so-called mixed dark matter [160] such as massive neutrinos [161] rather than the warm dark matter. The present constraints on the mixed and the warm dark matter come from the observations of the large-scale structure, especially Lyman-alpha cloud [48], while they can put the constraint on the mixed and warm dark matter with rather smaller free-streaming scale $k_{\rm fs} \ll 100\,{\rm Mpc}^{-1}$ than the typical free-streaming scale $k_{\rm fs} > 100\,{\rm Mpc}^{-1}$ in the present scenario. We suggest that the future observations of the redshifted 21 cm line should be most promising. In fact, the detectability of the neutrino mass in the future 21 cm line survey has been discussed [162, 163]. The spatial fluctuations of the 21 cm line from between $30 \lesssim z \lesssim 200$ can directly probe the linear matter density fluctuation with a comoving

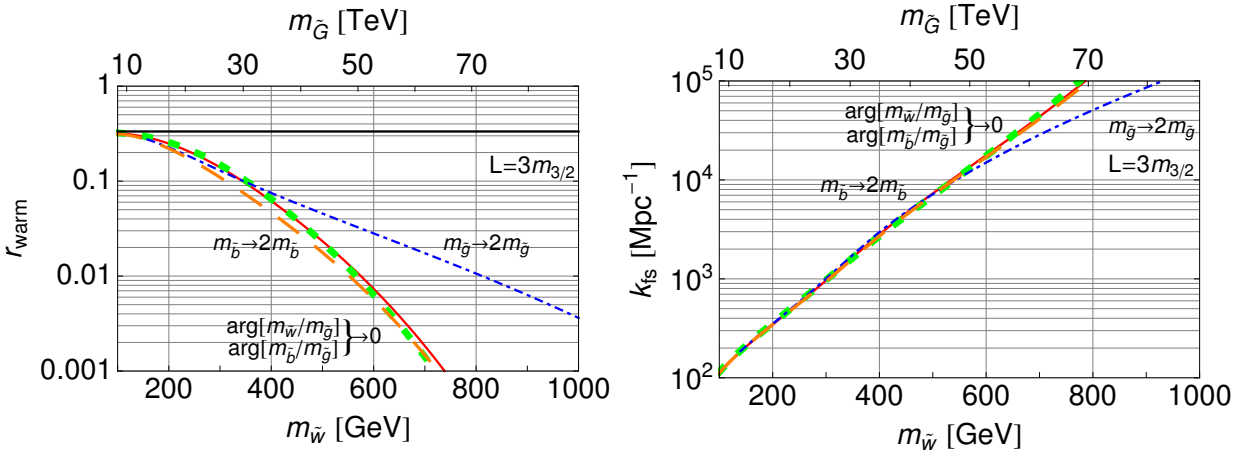

Figure 4.6: *The changes in the values of* $r_{\rm warm}$ *(left panel) and* $k_{\rm fs}$ *(right panel) for various values of* $\arg[m_{\tilde{w}}/m_{\tilde{g}}]$, $\arg[m_{\tilde{b}}/m_{\tilde{g}}]$ *(dotted lines),* $m_{\tilde{b}}$ *(dashed lines) and* $m_{\tilde{g}}$ *(dot dashed lines). Here, we have taken* $L = 3m_{3/2}$.

wavenumber larger than $100\,{\rm Mpc}^{-1}$ (wavelength smaller than 100 kpc) [164]. The detectability of the imprints of the non-thermal wino dark matter in the future 21 cm line survey should be studied, while it's beyond the scope of this chapter.

4.3 Conclusions

The wino dark matter is highly motivated in scenarios with heavy scalars such as the pure gravity mediation model after the discovery of a Higgs-like particle with a mass around 125 GeV at the LHC. In this chapter, we have studied how "warm" the wino dark matter is when it is non-thermally produced by the late time decays of the gravitinos.

The winos produced by the cascade decays of the gravitinos have the energy of $E_{\tilde{w}} \sim 0.1\, m_{3/2}$. The charged winos lose almost all of their energy within one lifetime through the electromagnetic interaction with the thermal background. As a result, at least two-thirds of the wino dark matter are "cold". The neutral winos produced by the decays of the gravitino can turn into charged winos by the inelastic scattering. The neutral winos which do not undergo the inelastic scattering become "warm". As we have shown, a sizable fraction of the wino dark matter can be "warm" for the wino mass $m_{\tilde{w}} \simeq 100 - 500\,{\rm GeV}$. The imprints on the matter power spectra may provide further insight on the origin of dark matter via the future 21 cm line survey in combination with the LHC experiments and the indirect dark matter searches. The detectability of the imprints of the non-thermal wino dark matter in the future 21 cm line survey is worthy of the future study.

Our calculation can be applied to other non-thermal wino production scenarios such as the wino dark matter produced by the decay of the moduli fields [128, 105, 165]. In such scenarios, the winos are over-produced after the chemical decoupling of the thermal winos, and then annihilate efficiently toexplain the observed dark matter density. Our calculation of the "warmness" of the wino dark matter is not altered by the annihilation process. However, the annihilation rate, which determines the relic density of the winos, can be altered by the existence of the "warm" component, while the thermally averaged annihilation rate is used in the literature. It should be noted that for the small fraction of the "warm" neural wino, the calculation with the thermally averaged annihilation rate is valid up to small corrections. We also should note that for heavier gluino scenarios, the imprints on the matter power spectra are enhanced, while searches in the LHC experiments become difficult.

Finally, we comment on a further application of this work. The higgsino dark matter scenarios are suggested in the supersymmetric models [166, 167]. The neutral and the charged higgsinos produced by the decay of the gravitino can leave the imprints on the matter power spectra as well as in the case of the non-thermal wino dark matter. In the higgsino dark matter scenarios, the mass splittings between the charged and the neutral higgsinos are in a GeV range, and hence, the lifetime of the charged higgsino is much shorter than the lifetime of the charged wino, which makes the higgsino dark matter "warmer". On the other hand, the higgsino-gaugino mixing provides the elastic scattering of the neutral higgsino at the tree level, which makes the higgsino dark matter "colder".

Chapter 5

Mixed (Cold+Warm) Dark Matter in the Bino-Wino co-annihilation scenario

In the previous chapter, we considered the wino LSP scenario in the high-scale SUSY breaking models. On the other hand, in the high-scale SUSY breaking models, bino LSP is realized with threshold effects by the higgsinos (see Fig. 4.1). In this chapter, we consider the bino LSP with the at most around 30 GeV heavier wino as the next-to-LSP (NLSP) in high-scale SUSY breaking scenarios. Due to the heavy sfermions, the self-annihilation of the bino LSP is insufficient and its thermal relic over-closes the Universe if the slightly heavier wino is not accompanied. On the other hand, the wino dark matter self-annihilates effectively, since the approximate custodial symmetry prohibits the large mass splitting between the neutral and the charged winos. The mass splitting between the neutral and the charged winos can be around $150 - 170\,\mathrm{MeV}$ [139, 104, 168]. The large annihilation cross section of the wino dark matter, however, is in tension with gamma-ray observations of the Galactic center in the Fermi-LAT and the H.E.S.S. telescope [169, 170], while there is still large ambiguity in the dark matter profile at the Galactic center. These issues are solved if the mass splitting between the bino LSP and the wino NLSP is sufficiently small. The small mass splitting keeps the wino and the bino abundance almost the same (except for the small Boltzmann factor) at the freeze-out. In this case, the efficient wino annihilation can reduce the resultant bino abundance to the observed dark matter density or below. This mechanism is referred to the co-annihilation [78].

We also consider the late-time decay of the gravitino, which provides the non-thermal bino dark matter when the small mass splitting between the bino and the wino does not leave the sufficient amount of the thermal bino dark matter. The non-thermal binos are highly energetic at the time of the gravitino decay. After that, they can loose their energy via interactions with the thermal background. Since the bino does not interact with the standard model particles elastically, the energy-loss proceeds via a cycle of interactions with the winos. The bino turns into the charged winos via the inelastic scattering by the thermal background. This inelastic process triggers the energy-loss cycle of the bino. The inelastic scattering rate is sensitive to the mass splitting between the bino and the wino, which also determines the thermal relic abundance of the bino. By direct integration of the Boltzmann equation with the energy-loss cycle, we show that a sizable fraction of the non-thermal bino remains relativistic after the energy-loss cycle becomes inefficient. Therefore, the bino dark matter, which consists of thermal and non-thermal components, can be mixed (cold+warm) dark matter. The imprints on the small-scale matter power spectrum may provide

further insights on the origin of dark matter via the future 21cm line survey [108, 109].

The organization of the chapter is as follows. In section 5.1, we summarize the bino-wino co-annihiliation scenario mainly assuming the pure gravity mediation [124, 125, 126]/minimal split SUSY model [171], although our discussion can be applied to generic bino-wino co-annihiliation scenarios. In section 5.2, we determines the mass splitting between the bino LSP and the wino NLSP for a given thermal relic abundance. The mass splitting determines the inelastic scattering rate of the non-thermal bino. In section 5.3, we discuss the imprints of the non-thermal bino on the small-scale matter power spectrum, assuming that the non-thermal bino is produced by the decay of the gravitino. Here, we clarify the energy-loss cycle of the non-thermal bino. The final section is devoted to summary.

5.1 The bino-wino co-annihilation Scenario

First, we summarize the bino-wino co-annihilation scenario in high-scale SUSY breaking models. [1] To be specific, we concentrate on the pure gravity mediation/minimal split SUSY model, although we do not need to change our discussion for generic bino-wino co-annihilation scenarios with the heavy sfermions and the heavy higgsinos. Then, we discuss phenomenological implications of the model.

5.1.1 Mass spectrum of the model

In the pure gravity mediation/minimal split SUSY model, the sfermion mass $m_{\tilde{f}}$ and the higgsino mass μ originate from the generic tree-level interactions in the supergravity, and thus they are expected to be of the order of the gravitino mass. The gravitino mass is set $m_{3/2} \simeq 10-1000\,\mathrm{TeV}$ in order to explain the large quantum corrections to the Higgs mass. On the other hand, the charge of the SUSY breaking field under some symmetry allows only one-loop suppressed contributions to the gaugino masses, i.e. the anomaly mediated contributions [136, 137]. The heavy higgsinos also lead to large threshold effects to the gaugino masses, which are parametrized by L [124, 125, 126, 104, 136]. The gaugino masses are given by Eq. (4.3)-(4.5). The formulas of the gaugino masses imply that bino is LSP for $L/m_{3/2} > 3$. We focus on the parameter region of $L/m_{3/2} \simeq 3.5 - 4.0$, where the mass splitting between the bino and the wino, $\Delta m_{\tilde{b}} \equiv m_{\tilde{w}} - m_{\tilde{b}}$, is about 10 % of the bino mass and the bino-wino co-annihilation is efficient. In the next section, we identify the suitable mass splitting for a given thermal relic density. In the following discussion, we set the sfermion mass and the higgsino mass equal to the gravitino mass $m_{\tilde{f}} = \mu = m_{3/2}$.

5.1.2 Phenomenological aspects of the model

Here, we describe phenomenological implications of the heavy sfermions and the heavy higgsinos. First, the large μ-term suppresses the bino-wino mixing to $\mathcal{O}(m_Z^2/(\mu|m_{\tilde{w}} - m_{\tilde{b}}|))$. Even with the small mass splitting between the bino and the wino, the bino compose at least 0.99 of LSP in the parameter region of interest. The tiny mixing and the heavy sfermions result in the extremely weakly interacting bino. Therefore, in the present model, the bino dark matter does not leave detectable signals in current and near-future direct and indirect detections of dark matter.

The only constraint is put by null-detection of the gluino signals at the LHC. By using multi-jets plus missing transverse momentum events, the ATLAS experiment reports that the gluino mass

[1] The bino-wino co-annihilation scenario, especially the thermal relic abundance of the bino, is studied in other contexts such as of the minimal supergravity model with non-universal gauging mass [172, 173] and the gaugino condensation in hidden sector [174].

should be $m_{\tilde{g}} \gtrsim 1.2\,\mathrm{TeV}$ for the LSP mass below 500 GeV [175]. In the near future, the 14 TeV LHC with $300\,\mathrm{fb}^{-1}$ has a potential to discover the gluino below $m_{\tilde{g}} \simeq 2.3\,\mathrm{TeV}$ [149]. Furthermore, a 33 TeV future proton collider with $3000\,\mathrm{fb}^{-1}$ can reach the gluino mass of $m_{\tilde{g}} \simeq 3.6\,\mathrm{TeV}$ [176]. Here, we should note that in these collider experiments, we can probe only the gluino production and its subsequent cascade decay, but not the bino LSP itself. This motivates us to study the cosmological imprints of the bino dark matter as the direct probe for the present scenario in this chapter.

The large μ-term also ensures the small mass splitting between the neutral wino $\tilde{w}^0$ and the charged winos $\tilde{w}^\pm$, $\Delta m_{\tilde{w}} \equiv m_{\tilde{w}^\pm} - m_{\tilde{w}^0}$. This is because the large μ-term suppresses the effect of the approximate custodial symmetry on the mass splitting $\Delta m_{\tilde{w}}$. The tree-level contribution to the mass splitting is $\Delta m_{\tilde{w}}^{\mathrm{tree}} \lesssim 20\,\mathrm{MeV}$ in the parameter region of interest. On the other hand, the one-loop contribution [139, 104] is given by

$$\Delta m_{\tilde{w}}^{\mathrm{loop}} = m_{\tilde{w}^\pm} - m_{\tilde{w}^0} = \frac{g_2^2}{16\pi^2} m_{\tilde{w}} \left[f(r_W) - \cos^2\theta_W f(r_Z) - \sin^2\theta_W f(0) \right], \tag{5.1}$$

where θ_W is the Weinberg angle, $f(r) = \int_0^1 dx (2+2x^2) \ln[x^2 + (1-x)r^2]$, and $r_{W,Z} = m_{W,Z}/m_{\tilde{w}}$ with the W, Z-boson mass $m_{W,Z}$. The one loop contribution is $\Delta m_{\tilde{w}}^{\mathrm{loop}} \simeq 150 - 170\,\mathrm{MeV}$, and thus dominates the mass splitting $\Delta m_{\tilde{w}}$. In the other scenarios with $|m_{\tilde{b}} - m_{\tilde{w}}| \sim m_{\tilde{b}}\,(m_{\tilde{w}})$, the tree-level contribution is negligible compared with the one-loop contribution, $\Delta m_{\tilde{w}}^{\mathrm{tree}} < \mathcal{O}(100)\,\mathrm{keV}$. However, in the present bino-wino co-annihilation scenario $\Delta m_{\tilde{b}}/m_{\tilde{b}} \ll 1$, the tree-level contribution is subdominant but can not be ignored, $\Delta m_{\tilde{w}}^{\mathrm{tree}}/\Delta m_{\tilde{w}}^{\mathrm{loop}} \lesssim 0.1$.

5.2 Mass splitting between bino and wino

The interactions of the bino LSP is extremely weak due to the heavy sfermions and the heavy higgisnos. The inefficient annihilation of the bino LSP generically leads to the over-closure of the Universe. However, when the bino is accompanied by the slightly heavier wino, the presence of the wino at the freeze-out of bino reduces the relic abundance of the bino. For the heavier bino with $m_{\tilde{b}} \gtrsim 1\,\mathrm{TeV}$, the bino-wino co-annihilation is also boosted up by the non-perturbative effects. The countless exchanges of gauge bosons (γ, W, Z) between the winos distort the initial state wave function from the direct product of the plane waves. This is known as the Sommerfeld enhancement [177]. In this section, we calculate the bino relic abundance taking into account the co-annihilation and the Sommerfeld enhancement.

5.2.1 Thermally averaged effective cross section

The thermal relic of the non-relativistic stable particle can be evaluated by solving the following Boltzmann equation [77],

$$\frac{dY}{dx} = -\frac{\langle \sigma v \rangle}{Hx} \left(1 - \frac{x}{3g_{*s}} \frac{dg_{*s}}{dx} \right) s \left(Y^2 - Y_{\mathrm{eq}}^2 \right), \tag{5.2}$$

with the time coordinate x, which is the inverse of the cosmic temperature T normalized by the particle mass m, $x \equiv m/T$. The yield of the particle Y is defined by the ratio of the particle number density n to the entropy density s, $Y = n/s$. The equilibrium yield Y_{eq} is given by,

$$Y_{\mathrm{eq}} = \frac{g}{(2\pi)^{3/2}} \frac{m^3}{s\, x^{3/2}} e^{-x}, \tag{5.3}$$

with the degrees of freedom of the particle g. The entropy density and the cosmic expansion rate H is given by,

$$s = g_{*s}\frac{2\pi^2}{45}\frac{m^3}{x^3}\,, \quad H = \left(\frac{g_*}{10}\right)^{1/2}\frac{\pi}{3M_{\rm pl}}\frac{m^2}{x^2}\,, \tag{5.4}$$

with the reduced Planck mass $M_{\rm pl} \simeq 2.43 \times 10^{18}\,\mathrm{GeV}$. The effective degrees of freedom for the energy density g_* and for the entropy density g_{*s} is calculated as the function of x according to Ref. [178]. The thermally averaged annihilation cross section $\langle\sigma v\rangle$ is related to the annihilation cross section (σv) by,

$$\langle\sigma v\rangle = \left(\frac{m}{4\pi T}\right)^{3/2}\int 4\pi v^2 dv\,(\sigma v)\,\exp\left(-\frac{mv^2}{4T}\right)\,, \tag{5.5}$$

with the relative velocity of the initial particles, v.

The co-annihilation introduces two changes in the above formulas [140],

$$g \;\rightarrow\; g_{\rm eff} = \sum_i g_i(1+\Delta_i)^{3/2}e^{-x\Delta_i}\,, \tag{5.6}$$

$$\langle\sigma v\rangle \;\rightarrow\; \langle\sigma_{\rm eff}v\rangle = \sum_{i,j}\langle\sigma_{ij}v\rangle\frac{g^2}{g_{\rm eff}^2}(1+\Delta_i)^{3/2}(1+\Delta_j)^{3/2}e^{-x(\Delta_i+\Delta_j)}\,. \tag{5.7}$$

The index i, j runs over the all particles that contribute to the co-annihilation including the stable particle itself. The dimensionless mass splitting between the stable particle and the particle i is defined by $\Delta_i = m_i/m - 1$. Since the thermal relic of the stable particle freeze-out at $x \simeq 20$ and the thermally averaged effective annihilation cross section $\langle\sigma_{\rm eff}v\rangle$ depends exponentially on the dimensionless mass splitting (Eq. (5.7)) , the co-annihilation is significant only with at most $\sim 10\,\%$ heavier particles than the stable particle.

The above formulas of the co-annihialation are valid only if the chemical equilibrium between the stable particle and the accompanying particles is kept around the freeze-out. In order to check this point, we should specify the inelastic interactions in charge of keeping the chemical equilibrium. In the case of our present bino-wino co-annihilation scenario, the dominant processes are $\tilde{b} + e\,(\nu_e) \leftrightarrow \tilde{w}^{\pm} + \nu_e\,(e)$, $\tilde{w}^0 + e\,(\nu_e) \leftrightarrow \tilde{w}^{\pm} + \nu_e\,(e)$, $\tilde{w}^{\pm} \rightarrow \tilde{b} + f_1 + \bar{f}_2$, $\tilde{w}^{\pm} \rightarrow \tilde{w}^0 + \pi$ and $\tilde{w}^0 \rightarrow \tilde{b} + f + \bar{f}$. The 2-body decays of $\tilde{w}^{\pm} \rightarrow \tilde{b} + \pi$ and $\tilde{w}^0 \rightarrow \tilde{b} + \pi$ are sub-dominant compared

with the 3-body decays for $\Delta m > 1\,\mathrm{GeV}$ [179]. The interaction rates are given by,

$$\Gamma_{\tilde{b}+e\,(\nu_e)\to\tilde{w}^{\pm}+\nu_e\,(e)} = 4N_{12}^2\langle\Gamma_{\mathrm{fi}}(p_{\tilde{b}},T;m_{\tilde{b}},\Delta m_{\tilde{b}}+\Delta m_{\tilde{w}})\rangle_{\tilde{b}}\,, \tag{5.8}$$

$$\Gamma_{\tilde{w}^0+e\,(\nu_e)\to\tilde{w}^{\pm}+\nu_e\,(e)} = 4\langle\Gamma_{\mathrm{fi}}(p_{\tilde{w}},T;m_{\tilde{w}},\Delta m_{\tilde{w}})\rangle_{\tilde{w}^0}\,, \tag{5.9}$$

$$\Gamma_{\tilde{w}^{\pm}+\nu_e\,(e)\to\tilde{b}+e\,(\nu_e)} = 4N_{12}^2\langle\Gamma_{\mathrm{bi}}(T;m_{\tilde{w}})\rangle_{\tilde{w}^{\pm}}\,, \tag{5.10}$$

$$\Gamma_{\tilde{w}^{\pm}+\nu_e\,(e)\to\tilde{w}^0+e\,(\nu_e)} = 4\langle\Gamma_{\mathrm{bi}}(T;m_{\tilde{w}})\rangle_{\tilde{w}^{\pm}}\,, \tag{5.11}$$

$$\begin{aligned}\Gamma_{\tilde{w}^{\pm}\to\tilde{b}+f_1+\bar{f}_2} = N_{12}^2\Bigg[&\sum_l \Gamma_c(m_{\tilde{w}^{\pm}},m_{\tilde{b}},m_l,0)\\ &+3\sum_{U,D}\left|V_{UD}^{\mathrm{CKM}}\right|^2\Gamma_c(m_{\tilde{w}^{\pm}},m_{\tilde{b}},m_{q_1},m_{q_2})\Bigg]\,,\end{aligned} \tag{5.12}$$

$$\Gamma_{\tilde{w}^{\pm}\to\tilde{w}^0+\pi} = \frac{2}{\pi}\left|V_{ud}^{\mathrm{CKM}}\right|^2 G_F^2 f_\pi^2 \Delta m_{\tilde{w}}^3\left(1-\frac{m_\pi}{\Delta m_{\tilde{w}}}\right)^{1/2}\,, \tag{5.13}$$

$$\begin{aligned}\Gamma_{\tilde{w}^0\to\tilde{b}+f+\bar{f}} = &\left[\frac{1}{2}\left(N_{13}-N_{23}\tan\theta_W\right)\cos\beta-\frac{1}{2}\left(N_{14}-N_{24}\tan\theta_W\right)\sin\beta\right]^2\\ &\times\left[\sum_l\Gamma_n(m_{\tilde{w}^0},m_{\tilde{b}},m_l)+3\sum_q\Gamma_n(m_{\tilde{w}^0},m_{\tilde{b}},m_q)\right]\\ &+\Bigg[\left(\frac{1}{2}\right)^2\sum_l\Gamma_{\tilde{f}}(m_{\tilde{w}^0},m_{\tilde{b}},m_l)\\ &\quad+3\left(\frac{1}{6}\right)^2\sum_q\Gamma_{\tilde{f}}(m_{\tilde{w}^0},m_{\tilde{b}},m_q)\Bigg]\,,\end{aligned} \tag{5.14}$$

with the Fermi constant G_F, the pion mass m_π, and the pion decay constant f_π. The mixing matrix of the neutralinos N_{ij} is defined in the same way as in Ref. [180]. The indices (i,j) on N_{ij} correspond to (mass, gauge) eigenstates. The subscripts qs and ls represent the quarks and the leptons, respectively. The Cabbibo-Kobayashi-Maskawa matrix is denoted by V_{UD}^{CKM}. The indices (U,D) on V_{UD}^{CKM} correspond to (up, down)-type quarks, while the indices (u,d) on V_{ud}^{CKM} in Eq. (5.13) denote the (up, down) quarks concretely. The ratio of the vacuum expectation values of the (up, down)-type Higgs, (v_u,v_d) is written as $\tan\beta = v_u/v_d$. It should be noted that $p_{\tilde{b},\tilde{w}}$ is

the physical momentum of the bino (wino) at the cosmic temperature T. Here, we define

$$\Gamma_{\rm fi}(p,T;m,\Delta m) = \frac{4}{3\pi^3}G_F^2T^5\left[72+36\frac{\Delta m}{T}+6\left(\frac{\Delta m}{T}\right)^2 -6\frac{p}{E}\left(\frac{\Delta m}{T}\right)^3+4\left(\frac{p}{E}\right)^2\left(\frac{\Delta m}{T}\right)^4\right]\exp\left(-\frac{\Delta m}{T}\right), \tag{5.15}$$

$$\Gamma_{\rm bi}(p,T;m) = \frac{96}{\pi^3}G_F^2T^5\frac{E^2+p^2}{m^2}, \tag{5.16}$$

$$\Gamma_c(M_1,M_2,m_1,m_2) = \frac{1}{3\pi^3}G_F^2\int_{M_2}^{\frac{M_1^2+M_2^2-(m_1+m_2)^2}{2M_1}} dE_2\,p_2\left(1-\frac{q^2}{m_W^2}\right)^{-2} \times\left[C_1\left(2(M_1E_2-M_2^2)(M_1-E_2)-M_2q^2\right)-C_2\left(2M_2-E_2\right)q^2\right] \tag{5.17}$$

$$\overset{M_1\to M_2,\,m_1=m_2=0}{\to} \frac{2}{15\pi^3}G_F^2(M_1-M_2)^5, \tag{5.18}$$

$$\Gamma_n(M_1,M_2,m) = \frac{1}{64\pi^3}\frac{g_2^4}{m_h^4}\left(\frac{m}{m_W}\right)^2\int_{M_2}^{\frac{M_1^2+M_2^2-4m^2}{2M_1}} dE_2\,p_2\left(1-\frac{q^2}{m_h^2}\right)^{-2} \times\left(1-\frac{4m^2}{q^2}\right)^{3/2}q^2\left(M_2+E_2\right) \tag{5.19}$$

$$\overset{M_1\to M_2,\,m=0}{\to} \frac{1}{240\pi^3}\frac{g_2^4}{m_h^4}\left(\frac{m}{m_W}\right)^2(M_1-M_2)^5, \tag{5.20}$$

$$\Gamma_{\tilde f}(M_1,M_2,m,c_{\tilde b\tilde w}) = \frac{1}{320\pi^3}\frac{g_1^2g_2^2}{m_{\tilde f}^4}\int_{M_2}^{\frac{M_1^2+M_2^2-4m^2}{2M_1}} dE_2\,p_2 \times\Big[C_1\left(2(M_1E_2-M_2^2)(M_1-E_2)+c_{\tilde b\tilde w}M_2q^2\right) +C_2\left(2c_{\tilde b\tilde w}M_2+E_2\right)q^2\Big] \overset{M_1\to M_2,\,m=0}{\to} \frac{(2+c_{\tilde b\tilde w})}{800\pi^3}\frac{g_1^2g_2^2}{m_{\tilde f}^4}(M_1-M_2)^5, \tag{5.21}$$

$$C_1 = \left(q^2-(M_1+M_2)^2\right)^{1/2}\left(q^2-(M_1-M_2)^2\right)^{1/2} \times\left(q^4+(M_1^2+M_2^2)q^2-2(M_1^2-M_2^2)^2\right)/q^6, \tag{5.22}$$

$$C_2 = \left(q^2-(M_1+M_2)^2\right)^{3/2}\left(q^2-(M_1-M_2)^2\right)^{3/2}/q^6, \tag{5.23}$$

$$q^2 = M_1^2+M_2^2-2M_1E_2, \tag{5.24}$$

with the mass of the standard model Higgs boson m_h. We normalize g_1 and g_2 such that $g_1 = \sqrt{5/3}\,g'$ and $g_2 = g$ with the conventional electro-weak gauge couplings g and g' ($e = g\sin\theta_W = g'\sin\theta_W$ with the positron charge e). The quantity in angle brackets $\langle Q\rangle_{\tilde b,(\tilde w)}$ denotes the average of quantity Q over the bino (wino) thermal distribution. The relative phase between the bino and the wino mass parameter $c_{\tilde b\tilde w}$ is unity in the present model, $c_{\tilde b\tilde w} = 1$.

In Fig. 5.1, we show the reaction rates for $m_{\tilde b} = 600\,\mathrm{GeV}$ and $\Delta m_{\tilde b} = 31.5\,\mathrm{GeV}$. The inelastic scatterings are efficient to keep the chemical equilibrium between $\tilde b$, $\tilde w^0$, and $\tilde w^\pm$ until the freeze-out of the bino LSP. It should also be noted that the 3-body decay of $\tilde w^\pm \to \tilde b + f_1 + f_2$, not the 2-body decay of $\tilde w^\pm \to \tilde w^0 + \pi$, dominates the decay of the charged winos.

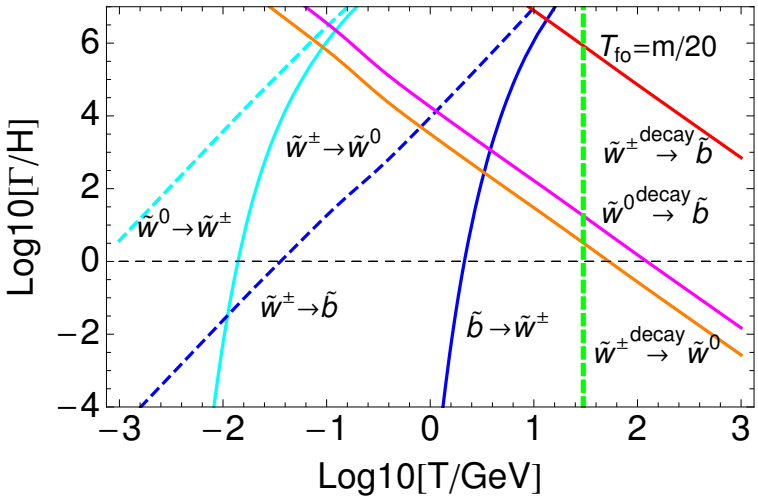

Figure 5.1: *The reaction rates of the inelastic processes in charge of keeping the chemical equilibrium between the bino $\tilde{b}$ and the winos $\tilde{w}$s. In the explanation of each line, we omit the standard model particles and explicitly specify the decay processes. Here, we set $m_{\tilde{b}} = 600\,GeV$ and $\Delta m_{\tilde{b}} = 31.5\,GeV$.*

The Sommerfeld enhancement is incorporated for the annihilations of the winos by calculating the annihilation cross section as

$$\sigma_{ij} v = c_{ij} \sum_{(k,l),(m,n)} d_{ij,kl} d^{*}_{mn,ij} \Gamma_{kl,mn}\,, \tag{5.25}$$

where $c_{ii} = 2$ and $c_{ij} = 1$ $(i \neq j)$, and $\Gamma_{ij,kl}$ is the absorptive term between two body states Φ_{ij} and Φ_{kl} [177]. The enhancement factor $d_{ij,kl}$ is given by the distortion of the wave function with respect to the relative position r of the annihilation particles at the infinity,

$$g^{>}_{ij,kl}(r) \overset{r\to\infty}{\to} d_{ij,kl} \exp(i\sqrt{mE}r)\,, \tag{5.26}$$

where $g^{>}_{ij,kl}(r)$ is the solution of the Schrödinger equation of

$$-\frac{1}{m}\frac{d^2}{dr^2} g^{>}_{ij,kl}(r) + \sum_{(m,n)} V_{ij,mn}\, g^{>}_{mn,kl}(r) = E g^{>}_{ij,kl}(r)\,, \tag{5.27}$$

with the potential $V_{ij,kl}(r)$ and the boundary condition of

$$g^{>}_{ij,kl}(0) = 0\,, \quad g^{>}_{ij,kl}(r) \overset{r\to\infty}{\propto} \exp(i\sqrt{mE}r)\,. \tag{5.28}$$

The absorptive term and the potential for each annihilation channel of the winos are summarized in Table 5.1.

5.2.2 The mass splitting between the bino and the wino $\Delta m_{\tilde{b}}$

We numerically solve the Boltzmann equation (Eq. (5.2)) with the co-annihilation and the Sommerfeld enhancement. We identify the suitable mass splitting between the bino and the wino $\Delta m_{\tilde{b}}$ for a given bino thermal relic, $r_{\rm T} \equiv \Omega^{\rm T}_{\tilde{b}}/\Omega_{\rm dm} = 1.0,\ 0.9,\ 0.5,\ 0.1$, up to $5\,\%$. The results are shown in Fig. 5.2.

Table 5.1: *The summary of absorptive term $\Gamma_{ij,kl}$ and the potential $V_{ij,kl}(r)$ for each annihilation channel of the winos. Here, we take an abbreviated notation of $c_W = \cos\theta_W$, $\alpha = e^2/4\pi$, and $\alpha_2 = g_2^2/4\pi$.*

channel $(i,\, j) \leftrightarrow (k,\, l)$	$\Gamma_{ij,kl}$	$V_{ij,kl}(r)$
$(\tilde{\chi}^{+(-)},\, \tilde{\chi}^{+(-)})$ (S=0)	$\dfrac{\pi\alpha_2^2}{2m^2}$	$\alpha\dfrac{1}{r} + \alpha_2 c_W^2 \dfrac{e^{-m_Z r}}{r}$
$(\tilde{\chi}^0,\, \tilde{\chi}^{\pm})$ (S=0, 1)	$\dfrac{\pi\alpha_2^2}{2m^2},\, \dfrac{25\pi\alpha_2^2}{24m^2}$	$-\alpha_2\dfrac{e^{-m_W r}}{r}$
$(\tilde{\chi}^{+},\, \tilde{\chi}^{-})$ (S=1)	$\dfrac{25\pi\alpha_2^2}{24m^2}$	$-\alpha\dfrac{1}{r} - \alpha_2 c_W^2 \dfrac{e^{-m_Z r}}{r}$
$(\tilde{\chi}^{+},\, \tilde{\chi}^{-}) \leftrightarrow (\tilde{\chi}^0,\, \tilde{\chi}^0)$ (S=0)	$\dfrac{\pi\alpha_2^2}{2m^2}\begin{pmatrix} 3 & \sqrt{2} \\ \sqrt{2} & 3 \end{pmatrix}$	$\begin{pmatrix} 2\Delta m_{\tilde{w}} - \alpha\dfrac{1}{r} - \alpha_2 c_W^2 \dfrac{e^{-m_Z r}}{r} & -\sqrt{2}\alpha_2\dfrac{e^{-m_W r}}{r} \\ -\sqrt{2}\alpha_2\dfrac{e^{-m_W r}}{r} & 0 \end{pmatrix}$

Here, we comment on the resonance in the Sommerfeld enhancement that is induced by the existence of the zero-energy binding states. As shown in Ref. [140], the wino relic abundance is resonantly reduced around some critical mass of $m_{\tilde{w}} > 2\,\mathrm{TeV}$. The resonance may change the monotonic decrease of $\Delta m_{\tilde{b}}$ in large $m_{\tilde{w}}$ (see Fig. 5.2). The first resonance appears around $m_{\tilde{b}} \simeq 2.4\,\mathrm{TeV}$ in our numerical calculation in the case of $\Delta m_{\tilde{b}} = 0$. However, we find that with a tiny mass splitting of at most $\Delta m_{\tilde{b}} \simeq 10\,\mathrm{MeV}$, the bino thermal relic can explain the observed dark matter density even around $m_{\tilde{b}} \simeq 2.4\,\mathrm{TeV}$. This is because the resonance is highly sensitive to the freeze-out temperature, which depends on the mass splitting between the bino and the wino $\Delta m_{\tilde{b}}$ (see Eq. (5.7)). The tiny mass splitting leads to an order of one mixing between the bino and the wino, i.e. the bino-wino dark matter rather than the bino dark matter. Since the phenomenology of the bino-wino dark matter is not the subject of this chapter, in the following we restrict ourselves within $m_{\tilde{b}} \lesssim 2.4\,\mathrm{TeV}$.

The mass splitting $\Delta m_{\tilde{b}}$ for $r_\mathrm{T} = 1.0$, plotted in Fig. 5.2, is the upper limit. If the mass splitting is larger, the bino thermal relic over-closes the Universe. On the other hand, for $r_\mathrm{T} < 1$, the thermal relic can not explain the observed mass density of dark matter. In that case, we need another production mechanism of the bino after the thermal freeze-out. We assume that the late-time decay of the gravitino is in charge. In the present scenario, the gravitino decays into the gauginos before the Big Bang Nucleosynthesis (BBN),

$$T_\mathrm{d} = \left(\frac{10}{\pi^2 g_*} M_\mathrm{pl}^2 \Gamma_{3/2}^2\right)^{1/4} \simeq 0.12\,\mathrm{MeV}\left(\frac{m_{3/2}}{10\,\mathrm{TeV}}\right)^{3/2}. \tag{5.29}$$

Here, the decay rate of the gravitino is given by,

$$\Gamma_{3/2} \simeq \frac{8+3+1}{32\pi}\frac{m_{3/2}^3}{M_\mathrm{pl}^2}. \tag{5.30}$$

The yield of the gravitino depends on the cosmic reheating temperature T_R. The resultant non-thermal bino relic is given by [181, 182],

$$\Omega_{\tilde{b}}^\mathrm{NT} h^2 \simeq 2.7\times 10^{-2}\left(\frac{m_{\tilde{b}}}{100\,\mathrm{GeV}}\right)\left(\frac{T_\mathrm{R}}{10^{10}\,\mathrm{GeV}}\right). \tag{5.31}$$

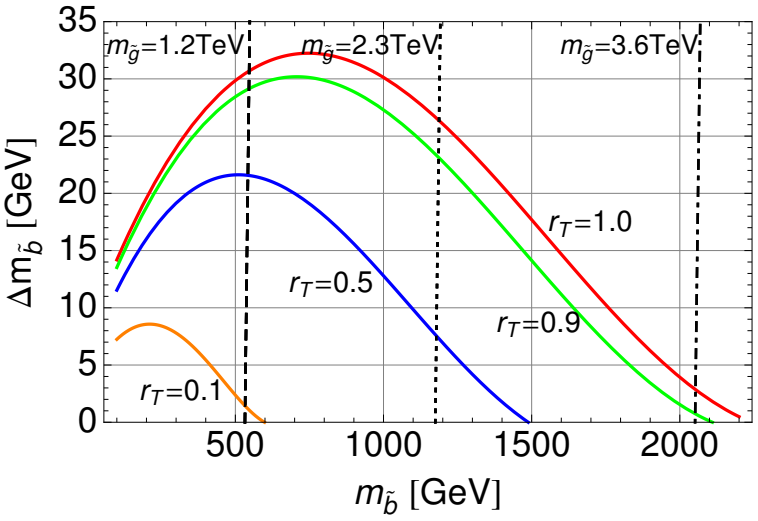

Figure 5.2: *The mass splitting $\Delta m_{\tilde{b}}$ as a function of the bino mass. Each line represents the thermal abundance of $r_{\rm T} = 1.0, 0.9, 0.5, 0.1$. The vertical lines show the constraints on the bino mass from the gluino search in the current LHC (dashed), the near-future LHC (dotted), and the future high-energy proton collider (dot-dashed).*

The non-thermal bino produced by the late time decay of the gravitino is relativistic. The dark matter with sizable peculiar velocity is called hot or warm dark matter, depending on the comoving velocity (roughly speaking, warm dark matter has comoving velocity of $v/c \sim 10^{-(7-8)}$). The peculiar velocity of warm dark matter suppresses the growth of primordial perturbations and leaves the cut-off in the matter power spectrum around the galactic or the sub-galactic scales [35]. The cut-off in the matter power spectrum is not only characteristic feature of the nature of dark matter, but also possible solution to the so-called "small-scale crisis" [183, 29, 30, 31]. As we will see in the next section, in the present scenario, the bino dark matter is mixed (warm+cold) dark matter rather than pure warm dark matter in the favored parameter range. However, tomography of the matter density fluctuations in the future 21 cm line observations is expected to give us a chance to find even weaker imprints on the matter power spectrum [164]. As mentioned in subsection 5.1.2, it is highly challenging to find the bino dark matter in direct and indirect detections. Therefore, the imprints on the matter power spectrum can give valuable evidence of the bino-wino co-annihilation scenario in high-scale SUSY models.

5.3 Imprints on the small-scale matter power spectrum

In this section, we study the imprints of the non-thermal bino on the small-scale matter power spectrum. The comoving velocity of the non-thermal bino at the gravitino decay can be estimated as,

$$v_{\tilde{b}}/c \simeq 6.8 \times 10^{-8} \left(\frac{m_{\tilde{b}}}{100\,\mathrm{GeV}}\right)^{-1} \left(\frac{m_{3/2}}{10\,\mathrm{TeV}}\right)^{-1/2} . \tag{5.32}$$

The non-thermal bino is sufficiently energetic to be warm dark matter when they are produced. However, after that, they may lose their energy through the interactions with the thermal background. Our goal is to obtain the momentum spectrum of the bino dark matter after the energy-loss

processes become inefficient. To this end, first, we clarify the dominant energy-loss process for non-thermal bino. Then, we derive and solve the Boltzmann equation of the momentum spectrum of the "warm" bino dark matter. Finally, we introduce two quantities that characterize the imprints of mixed dark matter on the matter power spectrum, and calculate them from the obtained momentum spectrum.

5.3.1 Energy-loss process

As mentioned above repeatedly, the bino LSP in the present scenario does not elastically interact with the standard model particles, i.e. thermal background. On the other hand, the winos can be a messenger between the bino and the standard model particles due to the small mass splitting $\Delta m_{\tilde{b}}$. The energy-loss of the non-thermally produced wino is investigated for the wino LSP in previous works [158] (see Chapter 4). Here we summarize their results, and discuss points of modification when we apply the previous results to the present scenario.

The charged winos lose their energy efficiently via Coulomb scattering,

$$-\frac{dE_{\tilde{w}^\pm}}{dt} = \frac{\pi\alpha^2 T^2}{3}\Lambda\left(1 - \frac{m_{\tilde{w}}^2}{2E_{\tilde{w}^\pm}^2}\ln\left(\frac{E_{\tilde{w}^\pm}+p_{\tilde{w}^\pm}}{E_{\tilde{w}^\pm}-p_{\tilde{w}^\pm}}\right)\right), \tag{5.33}$$

with the Coulomb logarithm Λ, which is estimated as

$$\Lambda = \ln\left[\frac{4\langle p_e^2\rangle}{k_{\rm D}^2}\right], \quad \langle p_e^2\rangle \sim \left(\frac{E_{\tilde{w}^\pm}}{m_{\tilde{w}^\pm}}T\right)^2, \quad k_{\rm D}^2 \simeq \frac{4\pi\alpha}{3}T^2, \tag{5.34}$$

taking into account the contributions to the Debye screening scale $k_{\rm D}$ from the relativistic electrons and the relativistic positrons. At the temperature of interest, $T_{\rm d} \simeq 0.1 - 10\,{\rm MeV}$, the charged wino turns into the neutral wino mainly via the 2-body decay process (see Fig. 5.3) in the case of the wino LSP. In this case, the relatively long lifetime of the charged winos allow the non-thermal charged winos lose most of their energy before they decay (see Chapter 4),

$$\tau_{\tilde{w}^\pm} \equiv \frac{1}{m_{\tilde{w}^\pm}\Gamma_{\tilde{w}^\pm\to\tilde{b}+f_1+\bar{f}_2}}\left(-\frac{dE_{\tilde{w}^\pm}}{dt}\right) \gg 1. \tag{5.35}$$

However, in the present scenario, the charged winos mainly decay into the bino LSP with a shorter lifetime. For the mass splitting of $\Delta m_{\tilde{b}} \gtrsim 5\,{\rm GeV}$, the energy-loss of the charged winos becomes inefficient, $-dE_{\tilde{w}^\pm}/\left(E_{\tilde{w}^\pm}\Gamma_{\tilde{w}^\pm}dt\right) \lesssim 1$, at $T \gtrsim 1\,{\rm MeV}$.

The neural wino itself does not have elastic energy-loss processes at the tree-level. The neutral wino lose its energy through the inelastic scattering of $\tilde{w}^0 + e\,(\nu_e) \to \tilde{w}^\pm + \nu_e\,(e)$. The inelastic scattering rate is given by,

$$\begin{aligned}\Gamma_{\tilde{w}^0,\,\rm inelastic} &= \frac{8}{\pi^3}G_F^2 T^5 \frac{(E_{\tilde{w}^0}+p_{\tilde{w}^0})^4}{m_{\tilde{w}}^2 E_{\tilde{w}^0}p_{\tilde{w}^0}}\left(6 + 2\frac{m_{\tilde{w}}}{E_{\tilde{w}^0}+p_{\tilde{w}^0}}\frac{\Delta m_{\tilde{w}}}{T}\right) \\ &\quad\times\exp\left(-\frac{m_{\tilde{w}}}{E_{\tilde{w}^0}+p_{\tilde{w}^0}}\frac{\Delta m_{\tilde{w}}}{T}\right).\end{aligned} \tag{5.36}$$

It should noted that this formula is applicable to only the relativistic wino and it is different from Eq. (5.9) that is for the non-relativistic wino. This formula can be easily translated into the inelastic scattering rate for the relativistic bino by multiplying the mixing and substituting physical quantities (e.g. mass splitting) related to the bino instead of the wino,

$$\Gamma_{\tilde{b},\,\rm inelastic} = N_{12}^2\Gamma_{\tilde{w}^0,\,\rm inelastic}(\tilde{w}^0 \to \tilde{b})\,. \tag{5.37}$$

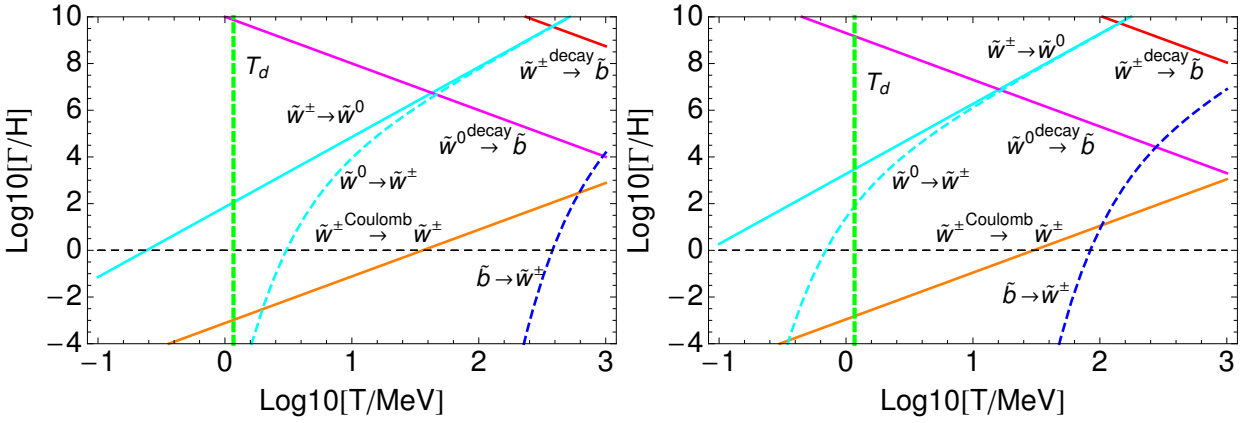

Figure 5.3: *The normalized reaction rates of interactions relevant to the energy-loss of the non-thermal bino (wino). Here, we take* $m_{\tilde{b}} = 600\,GeV$ *and* $\Delta m_{\tilde{w}} = 29.7\,GeV$ *(*$\leftrightarrow r_{\rm T} = 0.5$*) for* $E_{\tilde{b}(\tilde{w})} = 2\,TeV$ *(left panel) and* $E_{\tilde{b}(\tilde{w})} = 10\,TeV$ *(right panel). The vertical line shows the decay temperature of the gravitino (Eq. (5.29)).*

Table 5.2: *The energy-loss cycle of the bino and the winos around and after the gravitino decay.*

particle	dominant process
$\tilde{w}^{\pm}$	$\tilde{w}^{\pm} \overset{\text{Coulomb}}{\to} \tilde{w}^{\pm} \to \tilde{b} + f_1 + \bar{f}_2$
$\tilde{w}^0$	$\tilde{w}^0 + e\,(\nu_e) \to \tilde{w}^{\pm} + \nu_e\,(e)$ (high T)
	$\tilde{w}^0 \to \tilde{b} + f + \bar{f}$ (low T)
$\tilde{b}$	$\tilde{b} + e\,(\nu_e) \to \tilde{w}^{\pm} + \nu_e\,(e)$

In Fig. 5.3, we show the reaction rates for $m_{\tilde{b}} = 600\,\text{GeV}$ and $\Delta m_{\tilde{w}} = 29.7\,\text{GeV}$, which corresponds to the case of $r_{\rm T} = 0.5$. The energy of the bino (wino) is different in each panel, $E_{\tilde{b}\,(\tilde{w})} = 2\,\text{TeV}$ for the left panel and $E_{\tilde{b}\,(\tilde{w})} = 10\,\text{TeV}$ for the right panel. The inelastic scattering rate both for the bino and for the neutral wino sharply drops around

$$T_{\rm c} = \frac{m_{\tilde{b}\,(\tilde{w})}\Delta m_{\tilde{b}\,(\tilde{w})}}{2E_{\tilde{b}\,(\tilde{w})}} \simeq 900\,\text{MeV}\left(\frac{m_{\tilde{b}\,(\tilde{w})}}{600\,\text{GeV}}\right)\left(\frac{\Delta m_{\tilde{b}\,(\tilde{w})}}{30\,\text{GeV}}\right)\left(\frac{E_{\tilde{b}\,(\tilde{w})}}{10\,\text{TeV}}\right)^{-1}, \tag{5.38}$$

due to the Boltzmann factor in Eq. (5.36).

From Fig. 5.3, we can identify the energy-loss cycle of the bino and the winos around and after the gravitino decay and summarize it in Table 5.2. The non-thermal charged winos $\tilde{w}^{\pm}$ lose their energy thorough the Coulomb interaction and then decay into the bino $\tilde{b}$. The energetic bino $\tilde{b}$ is scattered inelastically and turns into the charged wino $\tilde{w}^{\pm}$. The relativistic neutral wino goes in two ways depending on the cosmic temperature. If the temperature is high enough, the inelastic scattering rapidly turns the neutral wino $\tilde{w}^0$ into the charged wino $\tilde{w}^{\pm}$. Otherwise, it decays into the bino $\tilde{b}$ before it is scattered inelastically.

5.3.2 Boltzmann equation and characteristic quantities

The discussion in the previous subsection clarifies the evolution equation of the bino momentum spectrum that should be solved. However, the calculation cost is still high and thus, we further simplify the evolution equation as follows without missing the essence. First, we take into account

the incomplete energy-loss of the charged winos until their decay by changing the bino inelastic scattering rate as,

$$\Gamma_{\tilde{b},\,\text{inelastic}} \to \left(1 - e^{-\tau_{\tilde{w}^\pm}}\right) \Gamma_{\tilde{b},\,\text{inelastic}}\,. \tag{5.39}$$

The prefactor $(1 - e^{-\tau_{\tilde{w}^\pm}})$ represents the probability of complete energy-loss at each inelastic scattering. The second simplification is for the neutral wino process. As we mentioned, the dominant process for the neutral wino shifts from the inelastic scattering to the decay as the temperature of the Universe decreases. We assume that this takes place instantaneously at the time

$$\tau_{\tilde{w}^0} \equiv \frac{\Gamma_{\tilde{w}^0,\,\text{inelastic}}}{(m_{\tilde{w}^0}/E_{\tilde{w}^0})\Gamma_{\tilde{w}^0 \to \tilde{b}+f+\bar{f}}} = 1\,. \tag{5.40}$$

With these simplifications, the Boltzmann equation of the momentum spectrum of the "warm" bino dark matter, $f_{\text{warm}}(p,t)$, can be written as,

$$\begin{aligned}
&\frac{\partial}{\partial t} f_{\text{warm}}(p,t) - Hp\frac{\partial}{\partial p} f_{\text{warm}}(p,t) \\
&\quad = \left[e^{-\tau_{\tilde{w}^\pm}} \frac{d\Gamma_{3/2,\,\tilde{w}^\pm}}{d^3p} + e^{-\Theta(\tau_{\tilde{w}^0}-1)\tau_{\tilde{w}^\pm}} \frac{d\Gamma_{3/2,\,\tilde{w}^0}}{d^3p} + \frac{d\Gamma_{3/2,\,\tilde{b}}}{d^3p} \right] \frac{a(t_0)^3}{a(t)^3} e^{-\Gamma_{3/2}t} \\
&\qquad - \left(1 - e^{-\tau_{\tilde{w}^\pm}}\right) \Gamma_{\tilde{b},\,\text{inelastic}}\, f_{\text{warm}}(p,t)\,,
\end{aligned} \tag{5.41}$$

with the Heaviside step function $\Theta(x)$. The differential decay rate of the gravitino into the bino $\tilde{b}$ (wino $\tilde{w}$), $d\Gamma_{3/2,\,\tilde{b}\,(\tilde{w})}/d^3p$, are given in Chapter 4. The prefactor $e^{-\Theta(\tau_{\tilde{b}}-1)\tau_{\tilde{w}^\pm}}$ and $e^{-\tau_{\tilde{w}^\pm}}$ represent the energy-loss of the neutral and the charged winos immediately after their production, respectively. The momentum spectrum of the "warm" bino dark matter is normalized such that,

$$\int \frac{d^3p}{(2\pi)^3}\, f_{\text{warm}}(p,t)\Big|_{t=t_0}^{\tau_{\tilde{w}^\pm}=0} = 1\,, \tag{5.42}$$

at present $t = t_0$ when we turn off the energy-loss process by hand, $\tau_{\tilde{w}^\pm} = 0$.

After obtaining the momentum spectrum of the "warm" bino dark matter, we calculate two quantities, which characterize the "warmness" of dark matter (see Chapter 4 for the case of the wino LSP). One is the resultant "warm" fraction of dark matter,

$$r_{\text{warm}} = (1 - r_{\text{T}}) \int \frac{d^3p}{(2\pi)^3}\, f_{\text{warm}}(p,t)\Big|_{t=t_0}\,. \tag{5.43}$$

The larger "warm" fraction leads to the more suppression of the matter power spectrum. The other is the free-streaming scale, which is defined by the Jeans scale at the matter radiation equality a_{eq},

$$\begin{aligned}
k_{\text{fs}} &= a\sqrt{\frac{4\pi G\rho_{\text{mat}}}{\langle v^2\rangle}}\Big|_{t=t_{\text{eq}}}\,, \\
\langle v^2\rangle(t_{\text{eq}}) &= (1 - r_{\text{T}})\frac{a(t_0)^2}{a(t_{\text{eq}})^2} \int \frac{d^3p}{(2\pi)^3}\, \frac{p^2}{m_{\tilde{b}}^2} f_{\text{warm}}(p,t)\Big|_{t=t_0}\,.
\end{aligned} \tag{5.44}$$

The free-streaming scale determines the critical scale below which the suppression on the matter power spectrum becomes significant (see Chapter 3).

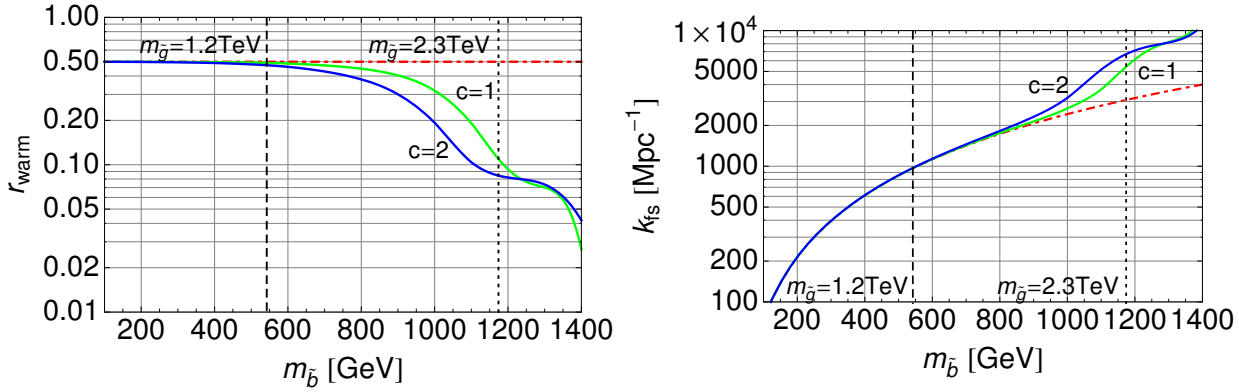

Figure 5.4: *The "warm" fraction $r_{\rm warm}$ (left panel) and the free-streaming scale $k_{\rm fs}$ (right panel). We set the mass splitting such that $r_{\rm T} = 0.5$ (see Fig. 5.2). The different choice of $c\,(= 1, 2)$ corresponds to the different value of the sfermion mass and the higgisino mass, $m_{\tilde{f}} = \mu = c\, m_{3/2}$. For comparison, we plot the "warmest" case ($\leftrightarrow \tau_{\tilde{w}^\pm} = 0$) in the dot-dashed line. Here, we also show the constraint on the bino mass from the current (8 TeV) and the future (14 TeV) gluino search at the LHC.*

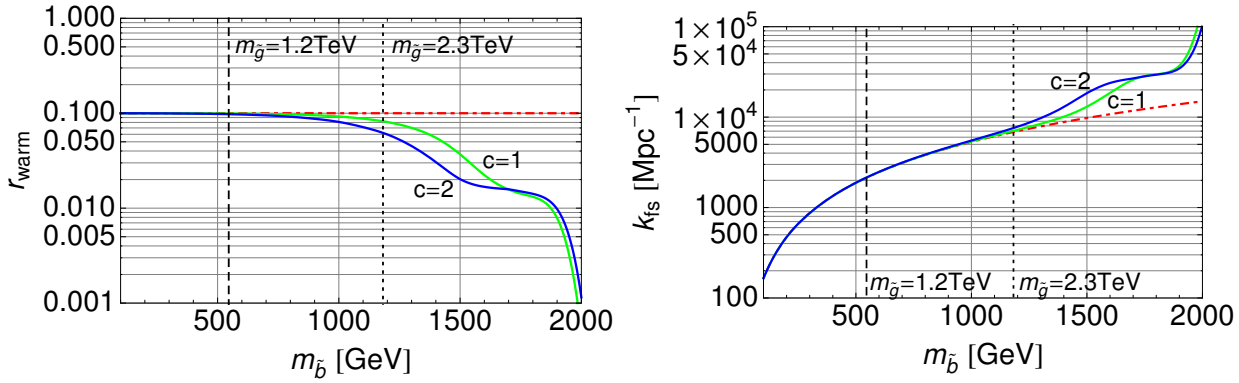

Figure 5.5: *The same plot as Fig. 5.4, but for $r_{\rm T} = 0.9$.*

5.3.3 Results

For each bino mass $m_{\rm b}$, we solve the Boltzmann equation (Eq. (5.41)) numerically to calculate $r_{\rm warm}$ and $k_{\rm fs}$. The results are shown in Fig. 5.4 ($\leftrightarrow r_{\rm T} = 0.5$) and Fig. 5.5 ($\leftrightarrow r_{\rm T} = 0.9$). The suppression of $r_{\rm warm}$ for the heavier bino mass $m_{\tilde{b}}$ is owing to the larger gravitino mass. The larger gravitino mass has two effects. First, the heavier gravitino decays in the earlier and hotter Universe, where the energy-loss processes are more efficient. Second, the bino and the winos are more energetic at the decay of the heavier gravitino, for which the inelastic scatterings are less suppressed.

While we set $m_{\tilde{f}} = \mu = m_{3/2}$ in the above discussion, this relation can be different by an order of one factor. In order to take into account this ambiguity, we introduce the parameter c, which is defined by

$$m_{\tilde{f}} = \mu = c\, m_{3/2}\,. \tag{5.45}$$

The effects of c parameter can be interpreted as follows. For the heavier sfermions and the heavier higgsinos ($c = 2$), the inelastic scattering rate $\Gamma_{\tilde{b},\,\rm inelastic}$ is more suppressed. However, as can be seen from Fig. 5.3, the inelastic scattering rate has dropped around the critical temperature (Eq. 5.38) well above the decay temperature of the gravitino $T_{\rm d}$ (Eq. 5.29). Therefore the additional order of one factor c does not have significant effects through the inelastic scattering rate. On the other

hand, the energy-loss via Coulomb scattering remains efficient until just before the gravitino decay. The large c prolongs the lifetime of the charged winos and thus, enhances their energy-loss during one lifetime $\tau_{\tilde{w}^\pm}$. Moreover, the large c increases the fraction of the non-thermal neutral wino that turns into the charged wino (i.e. large $\tau_{\tilde{w}^0}$). Therefore, the large c results in the "colder" bino dark matter with the smaller $r_{\rm warm}$ and the larger $k_{\rm fs}$.

Before closing this subsection, we remark the implication of our results. As we can see in Fig. 5.4 and Fig. 5.5, in the favorable (not constrained) parameter region, the "warm" component accounts for sizable fraction (at least 1 %) of the whole bino dark matter. This is why we refer the bino dark matter to mixed (cold+warm) dark matter in the present model. The bino dark matter can not resolve the so-called "small-scale crisis", since the free-streaming scale should be much smaller for that purpose, e.g. $k_{\rm fs} \simeq 20 - 200\,{\rm Mpc}^{-1}$ (see Chapter 3). Its imprints on the small-scale matter power spectrum, however, are significant before the formation of non-linear objects (e.g. dark matter halos) in the Universe. The future 21 cm survey will probe matter density fluctuations at high-redshifts, e.g. $z \simeq 30 - 200$, and thus provide us an important hint on the non-thermal production of the bino dark matter.

5.4 Summary

In this chapter, we studied the bino-wino co-annihilation scenario in high-scale SUSY breaking models with the heavy sfermions and the heavy higgsinos. As one specific realization, we consider the pure gravity mediation/minimal split SUSY model, which is highly motivated after the discovery of the Higgs boson. The wino LSP is now in tension with indirect dark matter searches by the Fermi-LAT and the H.E.S.S. telescope, while there is still large ambiguity in the dark matter profile at the Galactic center. On the other hand, the bino LSP is almost free from any direct and indirect detections.

The suppressed interaction of the bino dark matter generically results in the over-closure of the Universe. In order to account for the observed dark matter density, the bino LSP should be accompanied by the slightly heavier wino NLSP. The small mass splitting between the bino and the wino allows the sizable amount of the winos to exist at the freeze-out of the bino and it boosts the annihilation effectively. Therefore, for the first step, we identify the mass splitting needed for a correct bino thermal relic. In the calculation of the thermal relic, we take into account both the co-annihilation and the Sommerfeld enhancement. For that purpose, we also clarify the relevant processes in charge of keeping chemical equilibrium between the bino and the winos.

For smaller mass splittings, the bino thermal relic can not account for the whole dark matter density. We assume the late time decay of the gravitino produces the non-thermal bino after the freeze-out. The non-thermal bino is produced with sufficiently high energy to be "warm" dark matter. However, the "warmness" of the bino dark matter depends on the energy-loss processes after the production. To this end, we clarified the energy-loss cycle of the non-thermal bino and the non-thermal winos. With several reasonable simplifications, we derive the Boltzmann equation of the momentum spectrum of the "warm" bino dark matter. We solve it numerically and show that the "warm" component accounts for $1-50\,\%$ $(1-10\,\%)$ of the bino dark matter in the case of $r_{\rm T} = 0.5\,(0.1)$. The matter power spectrum is suppressed below $1-10\,{\rm kpc}$ $(\leftrightarrow k_{\rm fs} = 10^3 - 10^4\,[{\rm Mpc}^{-1}])$. As a result, we find that the imprints of non-thermal component on the small-scale matter power spectrum provides an invaluable hint on the present scenario, e.g. in the future 21 cm surveys.

In this chapter, we concentrated on the pure gravity mediation/minimal split SUSY model and its gaugino mass spectrum (Eq. (**??**)-(**??**)). However, the existence of the extra vector-like matter fields can change the gaugino mass spectrum [184]. In this case, the gluino mass as well as the wino mass can be close to the bino mass. The mass degeneracy hides the gluino from the collider

experiments, since the decay products of the gluino do not have sufficient energy to be distinguished from the background events. On the other hand, the cosmological imprints, which are discussed in this chapter, can be enhanced. This is because the gravitino mass can be smaller for the fixed bino mass. The lighter gravitino leaves the non-thermal bino with large comoving velocity at the gravitino decay (Eq. (5.32)). Moreover, the lighter gravitino decays at very late time (still before BBN), at which the energy-loss processes are insufficient (see Fig. 5.3).

Chapter 6

Weighing the Light Gravitino Mass with Weak Lensing Surveys

The null-detection of the SUSY particles so far suggests that SUSY is broken at some energy scale and mediated to MSSM via some messenger. Several mechanisms are proposed as the messenger such as gravity-mediated, anomaly-mediated, and gauge-mediated SUSY breaking (GMSB) models. GMSB models generally evade the flavor changing neutral current problem and the CP-problem, and thus they are thought to be the most interesting models.

Supergravity (SUGRA) as an extension of the global SUSY to the local one involves the super-partner of the graviton, which is referred to gravitino. The gravitino has helicity 3/2 and obtains the mass via the super-Higgs mechanism:

$$m_{3/2} = \frac{|\langle F \rangle|}{\sqrt{3} M_{\rm pl}}\,, \tag{6.1}$$

with the vacuum expectation value of F-term $\langle F \rangle$ and the reduced Planck mass $M_{\rm pl} \simeq 2.43 \times 10^{18}\,\mathrm{GeV}$. The gravitino is produced in the thermal bath immediately after the reheating of the Universe through the F-term suppressed interaction of goldstino component with spin $\pm 1/2$.

In the GMSB models, the gravitino mass is predicted to be in the range of $m_{3/2} \simeq \mathrm{eV}-\mathrm{keV}$. The small F-term allows the gravitino to be in the thermal equilibrium until the decoupling of others SUSY particles. When the gravitino is decoupled from the thermal bath, it begins to stream freely and contributes as a "diffuse" matter component of the Universe. The gravitino free-streaming imprints characteristic features on the matter power spectrum, which are expected to be probed by observations of large-scale structure. For example, the current constraint of $m_{3/2} < 16\,\mathrm{eV}$ is obtained by measuring the Ly-α flux power spectra that essentially probe the distribution of the inter-galactic medium at high redshifts [47]. We note that the constraint is based on the crucial assumption that the distribution of the inter-galactic neutral gas traces the distribution of underlying dark matter even at nonlinear length scales. Gravitational lensing provides a direct physical mean of probing the distribution of total matter. For example, it has been suggested that cosmic microwave background lensing has a potential to probe the gravitino mass of $m_{3/2} \simeq 1\,\mathrm{eV}$ in future experiments [185].

While the cosmological observations place an upper bound on the gravitino mass, the terrestrial collider experiments such as on-going Large Hadron Collider (LHC) give a lower bound through signatures of other SUSY particles (see Section 6.1). In the present chapter, we show that essentially all the interesting range of the gravitino mass can be probed by combining the up-coming LHC run at 14 TeV and the near future weak lensing surveys by the Subaru Hyper Suprime-Cam (HSC) and the Large Synoptic Survey Telescope (LSST).

Gravitational lensing is one of the powerful tools to probe directly the matter distribution in the Universe. The coherent pattern of image distortion by weak lensing is called cosmic shear. Cosmic shear in principle can be induced by any foreground mass distribution along the line of sight regardless of its dynamical state or luminosity. Cosmic shear signals have been detected with high significance levels, and constraints on some basic cosmological parameters have been derived [186, 187, 188, 189]. Upcoming weak lensing surveys such as HSC will cover a wide area extending more than a thousand square degrees. The surveys will also probe the matter distribution at $\sim$ Mpc scale most accurately, where the imprints of the gravitino can be detected. It is therefore important and timely to study the effect of the light gravitino on cosmic shear. To this end, we run a set of cosmological N-body simulations to follow the nonlinear evolution of the matter density fluctuations with the imprints of the gravitino free-streaming. We then perform accurate ray-tracing simulations of gravitational lensing. We show that the cosmic shear is indeed a promising probe of the existence and the mass of the light gravitino.

The rest of the chapter is organized as follows. In Section 6.1, we introduce the basics of the GMSB model. In particular, we clarify the relation between the gravitino mass and the masses of other SUSY particles. In Section 6.2, we discuss the linear evolution of the primordial density perturbation under the effect of the light gravitino. We present the resulting linear matter power spectra, which provides the initial conditions for our cosmological N-body simulations. In Section 6.3, we describe our simulation set-ups. In Section 6.4, we measure the cosmic shear power spectra from the simulations and forecast the discovery potential of the light gravitino in the future weak lensing surveys. The final section is devoted to the concluding remarks.

6.1 SUSY particle masses in the GMSB model

In the GMSB models [190, 191, 192, 193, 194, 70], the SUSY breaking is mediated from the hidden sector to the MSSM sector via some messenger fields that are charged under the standard model gauge group. The gaugino and the sfermion masses are induced by the one-loop and the two-loop diagrams, respectively, at the leading order. Note that the gaugino and sfermion mass spectrum generically depends on the charge assignment to the messenger fields and that inadequate charge assignment might ruin the success of MSSM in the grand unification of the gauge couplings. A popular choice is to set messenger fields in complete multiplets of the $SU(5)$ global/gauge symmetry. In the rest of this section, we consider specifically one of such models, the so-called minimal GMSB model.

The minimal GMSB model has the superpotential of

$$W = (\lambda S + M) \sum_{n=1}^{N_5} \Phi_n \bar{\Phi}_n \,, \tag{6.2}$$

where S is the goldstino superfields and M is the messenger mass. The F-term of the goldstino superfields develops the vacuum expectation values $\langle F \rangle$, and the N_5 pairs of messenger superfields Φ_n and $\bar{\Phi}_n$ $(n = 1, ..., N_5)$ form the multiplets of $\mathbf{5}$ and $\bar{\mathbf{5}}$ of $SU(5)$. In the minimal GMSB model, the gaugino mass is given by,

$$M_a = \frac{g_a^2}{16\pi^2} \Lambda N_5 g(x), \tag{6.3}$$

where the index $a\,(= 1, 2, 3)$ corresponds to the standard model gauge group $U(1)_Y \times SU(2)_L \times SU(3)_C$, and g_a denotes the standard model gauge coupling. We normalize g_1 and g_2 such that $g_1 = \sqrt{5/3}\, g'$ and $g_2 = g$ with the conventional electro-weak gauge couplings g and g' ($e =$

$g \sin\theta_W = g' \sin\theta_W$, e: positron charge, θ_W: Weinberg angle). The messenger scale Λ is defined by,

$$\Lambda = \left| \frac{\lambda \langle F \rangle}{M} \right| . \tag{6.4}$$

The function $g(x)$ is given by,

$$g(x) = \frac{1}{x^2}(1+x)\ln(1+x) + (x \to -x) , \tag{6.5}$$

and its argument is the dimensionless parameter $x = |\Lambda/M|$. The sfermion mass squared is given by

$$m_{\phi_i}^2 = 2\Lambda^2 N_5 \sum_{a=1}^{3} C_a(i) \left(\frac{g_a^2}{16\pi^2} \right)^2 f(x) , \tag{6.6}$$

where the index i denotes fermion flavour and $C_a(i)$ is the Casimir invariant. The function $f(x)$ is given by,

$$f(x) = \frac{1+x}{x^2} \left[\ln(1+x) - 2\mathrm{Li}_2\left(\frac{x}{1+x} \right) + \frac{1}{2}\mathrm{Li}_2\left(\frac{2x}{1+x} \right) \right] + (x \to -x) , \tag{6.7}$$

with the dilogarithm function $\mathrm{Li}_2(x)$. In practice, we use the public code `softsusy` [195] to calculate the mass spectrum of SUSY particles numerically. The calculations take into account the renormalization group running of SUSY particle masses. The gravitino mass (Eq. (6.1)) can be written in terms of the GMSB variables,

$$m_{3/2} = \frac{\Lambda M}{\sqrt{3} M_{\rm pl} |\lambda|} = \frac{\Lambda^2}{\sqrt{3} M_{\rm pl} |\lambda| x} . \tag{6.8}$$

From eqs. (6.3), (6.6) and (6.8), we can see that the SUSY particle masses are proportional to the square root of the gravitino mass, M_a, $m_{\phi_i} \propto \Lambda \propto \sqrt{m_{3/2}}$. Therefore, collider experiments with higher energies can be used generally to search for signatures of heavier SUSY particles, which in turn give information on gravitinos with relatively larger masses. Note that, in high-energy collision of the standard model particles, the direct product is not gravitino with gravitational interaction, but other SUSY particles with gauge interaction. For example, in proton-proton collision experiments at the LHC, the colored SUSY particles (i.e. gluino and squarks) are important and directly related to the discovery potential for SUSY particles. Lighter gravitinos are associated with lighter colored SUSY particles that can be searched even with the current generation experiments.

In order to derive conservative constraints on the gravitino mass from the collider experiments, we consider models with maximal N_5 and $|\lambda| x$. For the successful grand unification of the gauge couplings, the number of messenger N_5 needs to be at most five, $N_5 \leq 5$. We set $N_5 = 5$ as a conservative choice. The LHC current and future reach for the GMSB models is studied in detail in [196, 197, 198, 199, 200, 201, 202, 203, 204]. Let us consider two focus points specifically, as summarized in Table 6.1. The ATLAS collaboration sets the lower bound on $\Lambda > 51\,\mathrm{TeV}$ with $M = 250\,\mathrm{TeV}$ and $N_5 = 3$ ($\mathbf{10} + \bar{\mathbf{10}}$ of $SU(5)$) fixed from the events with at least one tau lepton and no light lepton in $21\,\mathrm{fb}^{-1}$ of LHC 8 TeV run [204]. This can be interpreted as a lower bound on the gravitino mass $m_{3/2} > 3\,\mathrm{eV}$ through Eq. (6.8), for the assumed perturbative coupling $|\lambda| < 1$.

It is expected that the $\Lambda = 80\,\mathrm{TeV}$ is accessible even for $N_5 = 5$ with the use of the multi-lepton modes in about $15\,\mathrm{fb}^{-1}$ of LHC 14 TeV run [200]. The stability of the SUSY breaking vacuum

focus point	fixed GMSB parameters	LHC	Λ	$m_{3/2}$
current	$M = 250\,\mathrm{TeV}, N_5 = 3, \lvert\lambda\rvert = 1$	$21\,\mathrm{fb}^{-1}$ at $\sqrt{s} = 8\,\mathrm{TeV}$	$\Lambda = 51\,\mathrm{TeV}$	$m_{3/2} = 3\,\mathrm{eV}$
future	$\lvert\lambda\rvert x = 1.4, N_5 = 5$	$15\,\mathrm{fb}^{-1}$ at $\sqrt{s} = 14\,\mathrm{TeV}$	$\Lambda = 80\,\mathrm{TeV}$	$m_{3/2} = 5\,\mathrm{eV}$

Table 6.1: Summary of the focus points for the GMSB model described in the text. The current focus point corresponds to the current lower bound on Λ reported in [204]. In the future focus point, the GMSB parameters are set such that they minimize the gravitino mass for fixed Λ while stabilizing the SUSY breaking vacuum. The future LHC reach is taken from [200].

requires $|\lambda|x > 1.4$ [205]. [1] An exciting implication of this is that virtually all of the GMSB models with $m_{3/2} < 5\,\mathrm{eV}$ can be probed in $15\,\mathrm{fb}^{-1}$ of LHC 14 TeV run. Later in section 4, we show that the future weak lensing survey can determine the gravitino mass with an accuracy of $m_{3/2} = 4 \pm 1\,\mathrm{eV}$, combined with the CMB anisotropy measurement by Planck satellite. We suggest that there is a good chance to test fundamentally the GMSB models in the near future.

6.2 Linear evolution of density perturbations with light gravitino

The light gravitino is in thermal equilibrium immediately after the reheating of the Universe unless the reheating temperature is extremely low [207]. When the cosmic temperature drops below the other SUSY particle masses, the decay and inverse-decay processes that have been keeping the thermal equilibrium between the light gravitino and the thermal bath, become inefficient. Then the light gravitino particles begins to stream freely with the momenta following the Fermi-Dirac distribution.

The gravitino contribution to the cosmic energy density is given by,

$$\Omega_{3/2}h^2 = 0.13 \left(\frac{g_{3/2}}{2}\right) \left(\frac{m_{3/2}}{100\,\mathrm{eV}}\right) \left(\frac{g_{*s3/2}}{90}\right)^{-1} \tag{6.9}$$

where $g_{*s3/2}$ is the effective massless degrees of freedom for the cosmic entropy at the time of gravitino decoupling. The exact value of $g_{*s3/2}$ depends on the mass spectrum of the SUSY particles (e.g. Λ) [208, 185]. However, its weak dependence allows us to fix $g_{*s3/2} = 90$ without changing our results by more than 5 %. It should be noted that the effective internal degrees of freedom of gravitino is not $g_{3/2} = 4$, but $g_{3/2} = 2$. This is because only goldstino component (spin $\pm 1/2$) can interact with the thermal bath through the $1/\langle F\rangle$ suppressed interactions.

From the above formula, we find that the light gravitino with $m_{3/2} \lesssim 100\,\mathrm{eV}$ (of our interest here) cannot account for the cosmological dark matter mass density. We assume that some cold and stable particle makes up the rest of dark matter, i.e.,

$$\Omega_{\mathrm{dm}} = \Omega_{\mathrm{cs}} + \Omega_{3/2}\,. \tag{6.10}$$

Such a cold and stable particle can be the QCD axion [209, 210, 211] or the composite baryons in the SUSY breaking, or can also be generated in the messenger sector in models with strongly coupled low scale gauge mediation [212, 213, 214, 215].

The free-streaming of light gravitino affects the evolution of primordial density perturbations in a similar manner as the standard model neutrinos do. We discuss the similarity and indeed the degeneracy of the effects of the light gravitino and the standard model neutrinos later in Section 6.4.

[1] Considering the thermal transition of the SUSY breaking vacuum leads to more stringent constraint on $|\lambda|x$ [206]. Here, we consider only quantum (zero-temperature) transition to be conservative.

The suppression owing to free-streaming occurs below a cut-off scale that is characterized by the Jeans scale at the matter-radiation equality $a_{\rm eq}$ (see Chapter 3):

$$k_{\rm J} = a\sqrt{\frac{4\pi G\rho_{\rm M}}{\langle v^2\rangle}}\bigg|_{a=a_{\rm eq}} \simeq 0.86\,{\rm Mpc}^{-1}\left(\frac{g_{3/2}}{2}\right)^{-1/2}\left(\frac{m_{3/2}}{100\,{\rm eV}}\right)^{1/2}\left(\frac{g_{*s3/2}}{90}\right)^{5/6}, \tag{6.11}$$

where G is the Newton's constant and $\rho_{\rm M}$ is the total matter density of the Universe. The mean square velocity $\langle v^2\rangle$ is evaluated over the whole dark matter mass distribution function $f_{\rm dm}(v)$ ($\int d^3v f_{\rm dm}(v) = \rho_{\rm dm}$). It means $\langle v^2\rangle = f_{3/2}\langle v^2\rangle_{3/2}$ effectively, where $f_{3/2}$ is the gravitino density fraction ($f_{3/2} \equiv \Omega_{3/2}/\Omega_c$) and $\langle v^2\rangle_{3/2}$ is the mean square velocity of the gravitino particles. The resultant linear matter power spectrum is shown and compared with that of the standard ΛCDM model in Figure 6.1.

Before discussing the details of the matter power spectrum, let us briefly consider the effect of some non-standard thermal history of the Universe. The overall influence of the light gravitino on the cosmic expansion can be basically characterized by one parameter, the gravitino mass $m_{3/2}$. This is because the gravitino temperature of the Fermi-Dirac distribution can be related to the observed CMB temperature through entropy conservation, i.e. $g_{*s3/2} \simeq 90$. However, non-standard thermal history with, e.g., entropy production [87], can change $g_{*s3/2}$ drastically to $g_{*s3/2} \simeq \mathcal{O}(1000)$. Then cosmological constraint on $m_{3/2}$ can be significantly altered, or the constraint needs to be re-interpreted within a suitable class of models. In the following discussion, we consider the standard thermal history with $g_{*s3/2} = 90$, and hence $m_{3/2}$ is the single model parameter.

We calculate the evolution of the linear density perturbations δ by modifying `CAMB` [89] suitably. In Figure 6.1, we plot the dimensionless matter power spectra $\Delta(k)$ defined by

$$\langle\delta(\mathbf{x})\delta(\mathbf{y})\rangle = \int d\ln k\,\Delta(k)\,e^{i\mathbf{k}\cdot(\mathbf{x}-\mathbf{y})}, \tag{6.12}$$

for mixed dark matter models with $m_{3/2} = 0$ (cdm), 4, and 16 eV. We adopt the cosmological parameters of the Planck mission first year results [1]. The free-streaming effect appears clearly at small length scales (Eq. 6.11) but the suppression below the cut-off scale is more significant for models with heavier gravitino (compare $m_{3/2} = 4$ eV and 16 eV in Figure 6.1). This is because larger $m_{3/2}$ gives a larger fractional contribution to the total matter density as $f_{3/2} \propto m_{3/2}$. We thus expect that models with heavy gravitino can be constrained by observations of large-scale structure of the universe.

6.3 Weak gravitational lensing

6.3.1 Lensing power spectrum

We summarize basics of gravitational lensing by large-scale structure. When one denotes the observed position of a source object as $\boldsymbol{\theta}$ and the true position as $\boldsymbol{\beta}$, one can characterize the distortion of image of a source object by the following 2D matrix:

$$A_{ij} = \frac{\partial\beta^i}{\partial\theta^j} \equiv \begin{pmatrix} 1-\kappa-\gamma_1 & -\gamma_2 \\ -\gamma_2 & 1-\kappa+\gamma_1 \end{pmatrix}, \tag{6.13}$$

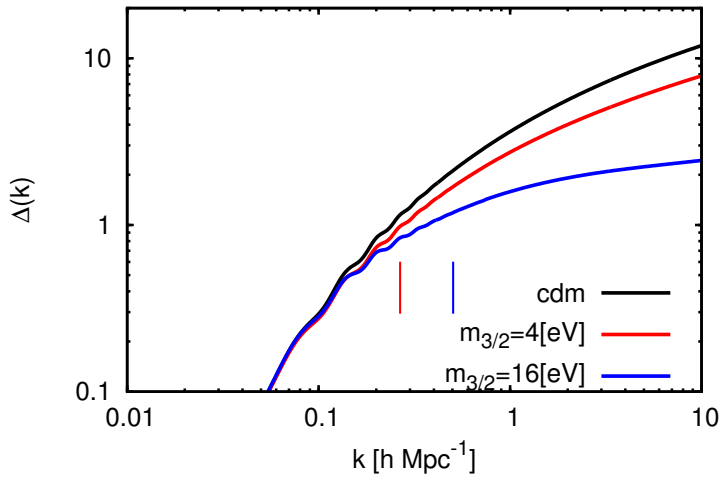

Figure 6.1: Linear dimensionless matter power spectra for $m_{3/2} = 0$ (cdm), 4, and 16 eV. We adopt basic cosmological parameters given by the Planck mission first year results [1]. The vertical lines represents the cut-off scales of Eq. (6.11).

where κ is convergence and γ is shear. In weak lensing regime (i.e. $\kappa, \gamma \ll 1$), each component of A_{ij} can be related to the second derivative of the gravitational potential Φ [216, 217] as

$$A_{ij} = \delta_{ij} - \Phi_{ij}, \tag{6.14}$$

$$\Phi_{ij} = \frac{2}{c^2}\int_0^\chi \mathrm{d}\chi' g(\chi,\chi')\frac{\partial^2}{\partial x_i \partial x_j}\Phi[r(\chi')\boldsymbol{\theta},\chi'], \tag{6.15}$$

$$g(\chi,\chi') = \frac{r(\chi-\chi')r(\chi')}{r(\chi)} \tag{6.16}$$

where χ is comoving distance, $r(\chi)$ is angular diameter distance, and $x_i = r\theta_i$ represents physical distance. By using the Poisson equation, one can relate the convergence field to the matter overdensity field δ [216, 217]. Weak lensing convergence field is then given by

$$\kappa(\boldsymbol{\theta},\chi) = \frac{3}{2}\left(\frac{H_0}{c}\right)^2 \Omega_{\mathrm{m0}}\int_0^\chi \mathrm{d}\chi' g(\chi,\chi')\frac{\delta[r(\chi')\boldsymbol{\theta},\chi']}{a(\chi')}. \tag{6.17}$$

In this chapter, we use the convergence power spectrum to constrain the gravitino mass. With the flat sky approximation, which is sufficient for angular scales of our interest, the Fourier transform of convergence field is defined by

$$\kappa(\boldsymbol{\theta}) = \int \frac{\mathrm{d}^2\ell}{(2\pi)^2} e^{i\boldsymbol{\ell}\cdot\boldsymbol{\theta}}\tilde{\kappa}(\boldsymbol{\ell}). \tag{6.18}$$

The power spectrum of the convergence field P_κ is defined by

$$\langle\tilde{\kappa}(\boldsymbol{\ell}_1)\tilde{\kappa}(\boldsymbol{\ell}_2)\rangle = (2\pi)^2\delta_D(\boldsymbol{\ell}_1-\boldsymbol{\ell}_2)P_\kappa(\ell_1), \tag{6.19}$$

where $\delta_D(\boldsymbol{\ell})$ is the Dirac delta function. By using Limber approximation [218, 219] and Eq. (6.17), we obtain the convergence power spectrum as

$$P_\kappa(\ell) = \int_0^{\chi_s}\mathrm{d}\chi\frac{W(\chi)^2}{r(\chi)^2}P_\delta\left(k=\frac{\ell}{r(\chi)},z(\chi)\right), \tag{6.20}$$

where $P_\delta(k)$ is the three dimensional matter power spectrum, χ_s is comoving distance of source galaxies and $W(\chi)$ is the lensing weight function defined as

$$W(\chi) = \frac{3}{2}\left(\frac{H_0}{c}\right)^2 \Omega_{\rm m0}\frac{r(\chi_s-\chi)r(\chi)}{r(\chi_s)}(1+z(\chi)). \tag{6.21}$$

The non-linear gravitational growth of $P_\delta(k)$ significantly affects the amplitude of convergence power spectrum for the angular scales less than 1 degree [220, 221, 222]. Typical weak lensing surveys are aimed at measuring the cosmic shear at angular scales larger than a few arcmin, corresponding to a few mega-parsec. Therefore, accurate theoretical prediction of non-linear matter power spectrum is essential to derive cosmological constraints from weak lensing power spectrum. Several analytic models are available that accurately predict the non-linear evolution of $P_\delta(k)$ for the standard ΛCDM universe [223, 224, 225, 2]. Unfortunately, there are no calibrated fitting formulae of $P_\delta(k)$ for the mixed dark matter models we consider here. We thus use direct numerical simulations to obtain the convergence power spectra.

6.3.2 Cosmological simulations

N-body simulations

It is necessary to use ray-tracing simulations in order to study the effect of light gravitino on the weak lensing power spectrum in nonlinear regimes. We first run cosmological N-body simulations for models with light gravitinos. We use the parallel Tree-Particle Mesh code `Gadget2` [95]. Each simulation is run with 512^3 dark matter particles in a volume of comoving 240 Mpc/h on a side. We generate the initial conditions following the standard Zel'dovich approximation. We use the accurate linear matter power spectrum calculated by the modified `CAMB` (Section 6.2). It is important to generate the initial conditions at a sufficiently low redshift so that the total matter, including the contribution from the light gravitino, can be treated as effectively a cold component. We set the initial redshift $z_{\rm init} = 9$ because the typical thermal velocity of the gravitino is then sufficiently small compared to the virial velocity of the smallest halos resolved in our simulation. We also run a N-body simulation from $z_{\rm init} = 49$ for the mixed dark matter model to examine the overall effect caused by the choice of $z_{\rm init}$.

For our fiducial cosmology, we adopt the following parameters: matter density $\Omega_m = 0.3175$, dark energy density $\Omega_\Lambda = 0.6825$ with the equation of state parameter $w_0 = -1$, Hubble parameter $h = 0.6711$ and the primordial spectrum with the scalar spectral index $n_s = 0.9624$ and the normalized amplitude $A_s = 2.215 \times 10^{-9}$ at the pivot scale $k = 0.05$ Mpc^{-1}. These parameters are consistent with the Planck mission first year results [1]. Two cases with the gravitino mass $m_{3/2} = 4$ and 16 eV are chosen as representative models. We summarize the simulation parameters in Table 6.2.

Ray-Tracing simulation

We generate light-cone outputs from our N-body simulations for ray-tracing simulations of gravitational lensing. The simulation boxes are placed to cover a past light-cone of a hypothetical observer with angular extent $5^\circ \times 5^\circ$, from redshift $z = 0$ to $z \sim 1$, similarly to the methods in [226, 227]. We use the standard multiple lens plane algorithm in order to simulate gravitational lensing signals [220]. The configuration of our simulations is similar to that in [222].

We set the initial ray directions on 4096^2 grids. The corresponding angular grid size is $5^\circ/4096 \sim 0.075$ arcmin. To avoid multiple appearance of the same structure aligned along a line-of-sight, we shift randomly the N-body simulation boxes. In addition, we use simulation outputs from

	$m_{3/2}$ [eV]	$z_{\rm init}$	# of N-body sims
CDM	0	49	5
MDM4–lowz	4	9	5
MDM16–lowz	16	9	5
MDM4–highz	4	49	5
MDM16–highz	16	49	5

Table 6.2: Parameters for our N-body simulations. For each model, we run 5 N-body realizations and generate 20 weak lensing convergence maps.

independent realizations when generating the light-cone outputs. Finally we obtain 20 independent convergence maps from 5 N-body simulations for each cosmological model. We fix the redshift of the source galaxies to $z_{\rm source} = 1.0$.

We measure the binned power spectrum of convergence field by averaging the product of Fourier modes $|\tilde{\kappa}(\boldsymbol{\ell})|^2$ for each multiple bin with $\Delta \log_{10} \ell = 0.1$ from $\ell = 100$ to 10^5.

6.4 Results

6.4.1 Convergence power spectrum

Let us first discuss how the light gravitino affects the lensing power spectrum. Figure 6.2 compares the measured convergence power spectra with the analytic model prediction (Eq. (6.20)) calculated by the fitting model in [2]. The results for $m_{3/2} = 0, 4$ and 16 eV are shown in the left, medium and right panel, respectively. The red points show the average power spectrum over 20 realizations with the error bars indicating the standard deviation of the realizations. The solid line is the model prediction of Eq. (6.20) for $z_{\rm source} = 1$. Note that the fitting function for $P_\delta(k)$ is calibrated for the standard ΛCDM cosmologies with a wide range of cosmological parameters. We thus assume that the non-linear evolution of $P_\delta(k)$ for our mixed dark matter model is also described in the same manner as in the standard ΛCDM. In practice, we simply input the linear power spectrum for the mixed dark matter model (Section 3), but do not change the coefficients in the formula.

We see in Figure 6.2 that the analytic model and the simulation result agree well to $\ell \leq 4000$. This is consistent with the results of previous studies [222, 2]; the fitting model becomes less accurate at (sub-)arcminute scales even in the case of standard ΛCDM cosmology. The convergence power spectra for the mixed dark matter model differ significantly from that for the ΛCDM model even at around $\ell = 1000$ corresponding to physical mega-parsec scale. Clearly, free-streaming of the gravitino affects the matter power spectrum at the nonlinear scales, and thus the above simple analytic approach does not work well even at $\ell = 1000$ for the mixed dark matter model.

We have examined the effect of choice of the initial redshift. In general, N-body simulations for the kind of mixed dark matter model should be initialized at a sufficiently low redshift in order to avoid numerical effects owing to gravitino thermal motions. Because assigning thermal velocities to N-body simulation particles is a non-trivial issue (see, e.g., [228]), we do not attempt to add random velocities to the particles. Instead, we examine how the choice of initial redshift affects the result at low redshifts by comparing two simulations that are started from $z_{\rm init} = 9$ and 49. Figure 6.3 compares the lensing power spectra obtained from our simulations with different $z_{\rm init}$.

The red points are for the gravitino with $m_{3/2} = 4$ eV and the blue points for $m_{3/2} = 16$ eV. Note that, unlike in ordinary warm dark matter models, the free-streaming scale, the gravitino mass, and the cosmic abundance are all related to each other in our light gravitino model. We plot

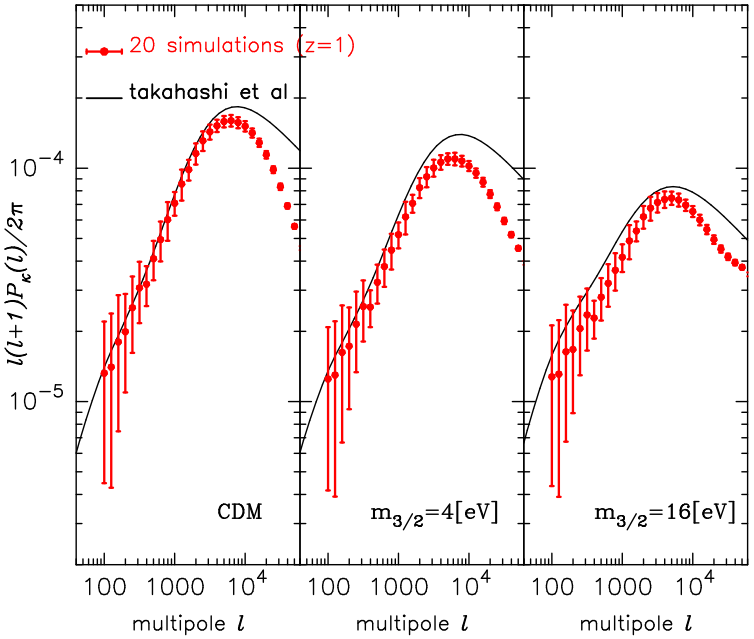

Figure 6.2: The convergence power spectra from our ray-tracing simulations for models with $m_{3/2} = 0, 4$ and 16 eV are shown in the left. In each panel, the red points represent the average measured power spectrum and the error bars show the standard deviation over 20 realizations. We use the simulations that start from $z_{\rm init} = 9$ for this figure. The solid line is calculated by Eq. (6.20) and fitting formula of $P_\delta(k)$ in [2] with $z_{\rm source} = 1.0$.

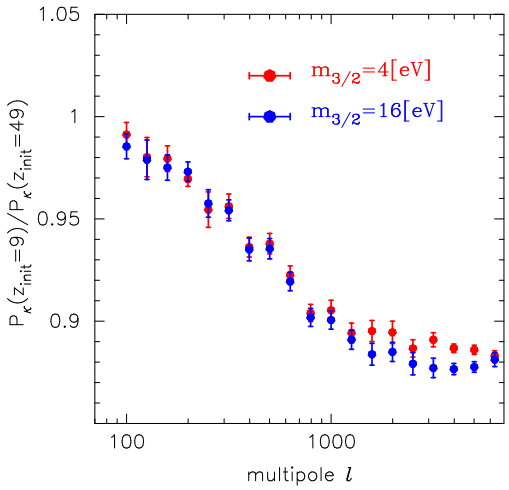

Figure 6.3: We plot the ratio of the lensing power spectra of the ray-tracing simulations with $z_{\rm init} = 9$ and 49. The error bars indicating standard deviation estimated from 20 realizations.

the standard deviation of mean value over 20 maps as error bars for each model. We find that the initial redshift affects the convergence power spectra at a level of ~ 10 %. It is important to note that the simulation from $z_{\rm init} = 49$ is not set up consistently, because our simulation particles can represent only non-relativistic components, while the light gravitino is relativistic at such a high redshift. Overall, Figure 6.3 indicates that the simulated lensing power spectrum for the mixed dark matter model likely has inaccuracies with a level of $\sim 10\%$.

	$m_{3/2}$ [eV]	$10^9 A_s$	n_s	$\Omega_c h^2$	w_0
fiducial	4	2.215	0.924	0.12029	-1
$d\boldsymbol{p}$	–	0.1	0.01	0.03	0.1

Table 6.3: Parameters in our Fisher analysis. For each parameter, we calculate the power spectra P_κ with $d\boldsymbol{p}$ varied around the fiducial value in order to calculate the derivative of Equation (6.23).

6.4.2 Fisher analysis

We perform a Fisher analysis to forecast the cosmological parameter constraints, including $m_{3/2}$. For a multivariate Gaussian likelihood, the Fisher matrix F_{ij} is written as

$$F_{ij} = \frac{1}{2}\mathrm{Tr}\left[A_i A_j + C^{-1}M_{ij}\right], \tag{6.22}$$

where $A_i = C^{-1}\partial C/\partial p_i$, $M_{ij} = 2\left(\partial P_\kappa/\partial p_i\right)\left(\partial P_\kappa/\partial p_j\right)$, C is the data covariance matrix and $\boldsymbol{p}$ is a set of parameters of interest. [2] In the present study, we choose $\boldsymbol{p} = (m_{3/2}, 10^9 A_s, n_s, \Omega_c h^2, w_0)$ as cosmological parameters to constrain. For the Fisher analysis, we need to calculate the derivative of P_κ with respect to $\boldsymbol{p}$. For $m_{3/2}$, we first fit the measured power spectrum $P_\kappa(\ell)$ using a quadratic form of $m_{3/2}$, i.e. $a_0(\ell) + a_1(\ell)m_{3/2} + a_2(\ell)m_{3/2}^2$. We then calculate the derivative by $a_1(\ell) + 2a_2(\ell)m_{3/2}$. For the other parameters, we evaluate the derivatives as follows:

$$\frac{\partial P_\kappa(\ell)}{\partial p_i} = \frac{P_\kappa(\ell, p_i^{(0)} + dp_i) - P_\kappa(\ell, p_i^{(0)} - dp_i)}{2dp_i}, \tag{6.23}$$

where $p_i^{(0)}$ is the fiducial value and dp_i is the variation of i-th parameter. Here, we simply calculate $P_\kappa(\ell, \boldsymbol{p})$ using Eq. (6.20) and the fitting formula of $P_\delta(k)$ in [2]. We summarize the fiducial values of $\boldsymbol{p}$ and $d\boldsymbol{p}$ in Table 6.3.

The covariance matrix of the convergence power spectrum can be expressed as a sum of the Gaussian and non-Gaussian contributions [230, 222]. Previous studies show that the non-Gaussian error degrades the constraints on cosmological parameters with a level of $O(10\%)$ [231]. We calculate the non-Gaussian contribution by using 1000 lensing maps in [222] in the following direct manner:

$$\mathrm{Cov}[P_\kappa(\ell), P_\kappa(\ell')] = \frac{1}{N_R - 1}\sum_{r=1}^{N_R}(\hat{P}_\kappa^r(\ell) - \bar{P}_\kappa(\ell))(\hat{P}_\kappa^r(\ell') - \bar{P}_\kappa(\ell')), \tag{6.24}$$

where $\hat{P}_\kappa^r(\ell)$ is the measured power spectrum in r-th realization and $\bar{P}_\kappa(\ell)$ is the average power spectrum over $N_R = 1000$ realizations. The configuration of the simulation in [222] is similar to ours, which covers 25 deg^2 on the sky. When necessary, we simply scale the covariance matrix Eq. (6.24) by the designated survey area.

We also take various systematic effects into account in the following manner. It is well-known that the intrinsic ellipticities of source galaxies induce noises to lensing power spectrum. Assuming intrinsic ellipticities are uncorrelated, we compute the noise contribution to the covariance matrix of convergence power spectrum as [232]

$$\mathrm{Cov}[P_\kappa(\ell), P_\kappa(\ell')]|_{\mathrm{noise}} = \frac{2}{f_{\mathrm{sky}}(2\ell+1)\Delta\ell}P_{\mathrm{noise}}\left(P_{\mathrm{noise}} + 2P_\kappa(\ell)\right)\delta_{\ell\ell'}, \tag{6.25}$$

$$P_{\mathrm{noise}} = \frac{1}{n_{\mathrm{gal}}}\left(\frac{\sigma_{\mathrm{int}}}{\mathcal{R}}\right)^2, \tag{6.26}$$

[2] We only consider the second term in Eq. (6.22). Because C scales approximately inverse-proportionally to survey area, the second term is expected to be dominant for a very wide area survey [229].

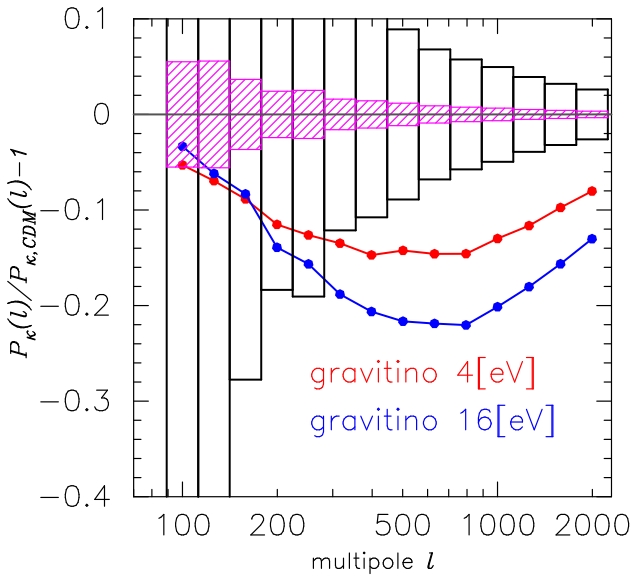

Figure 6.4: The derived statistical error of the lensing power spectrum. The boxes show the statistical error of lensing power spectrum given by a sum of Eq. (6.24) and (6.25). The black boxes are for a 25 deg^2 area survey, which is same as the size of our simulation. The purple hatched regions show the expected error for upcoming lensing survey with an area of 1500 deg^2. For comparison, we also plot the difference of the lensing power spectra between the pure CDM model and mixed dark matter models. The red line is for $m_{3/2} = 4$ eV and the blue one for $m_{3/2} = 16$ eV. For this plot, the number density of sources is set to be 10 arcmin^{-2}.

where $\Delta\ell$ is the width of the multipole bin, $f_{\rm sky}$ is the fraction of sky covered, $n_{\rm gal}$ is the number density of source galaxies, $\mathcal{R}$ is the shear response, and $\sigma_{\rm int}$ is the root-mean-square of the shear noise. Throughout the present chapter, we adopt $\mathcal{R} = 1.7$ and $\sigma_{\rm int} = 0.4$. The values are typical in ground based weak lensing surveys [233, 234]. We finally obtain the covariance matrix for our Fisher analysis as a sum of Eq. (6.24) and (6.25). In Figure 6.4, we compare the derived statistical error (the square root of the diagonal part of the covariance matrix) and the estimated difference of the lensing power spectra between the mixed dark matter models considered here. Clearly, future wide field lensing surveys with 1500 square degrees can discriminate (or constrain) the light gravitino models. There are some certain degeneracies among the cosmological parameters, which we shall discuss in section 5.4.

We explore more realistic constraints by using priors expected from the cosmological parameter estimates from the Planck satellite mission. When we compute the Fisher matrix for the CMB, we use the Markov-Chain Monte-Carlo (MCMC) engine `COSMOMC` [235] for exploring cosmological parameter space. We consider the parameter constraints from the angular power spectra of temperature anisotropies, E-mode polarization, and their cross-correlation. For MCMC, in addition to $10^9 A_s, n_s, \Omega_c h^2$ and w_0, we adopt the baryon density $\Omega_b h^2$, Hubble parameter h, and reionization optical depth τ as independent parameters. To examine the potential of lensing power spectrum to constrain $m_{3/2}$, we do not assume any prior on $m_{3/2}$ from the CMB. Assuming that the constraints from the CMB and the lensing power spectrum are independent of each other, we express the total Fisher matrix as

$$\boldsymbol{F} = \boldsymbol{F}_{\rm lensing} + \boldsymbol{F}_{\rm CMB}. \tag{6.27}$$

When we include the CMB priors in this way, we marginalize over the other cosmological parameters

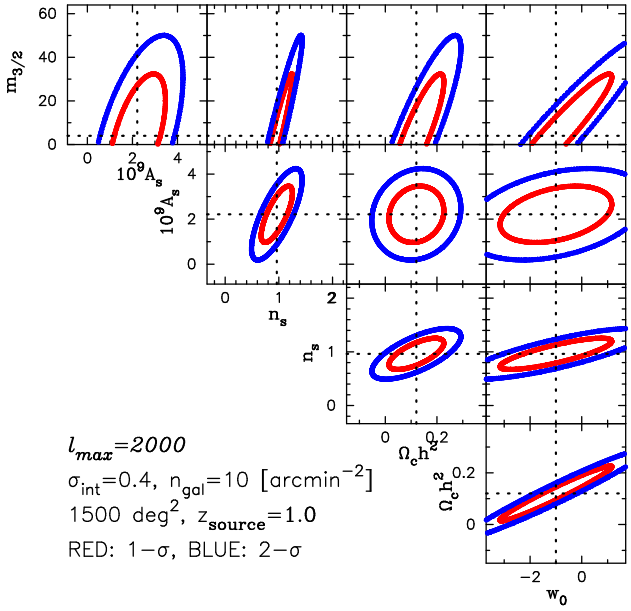

Figure 6.5: We show the cosmological constraints from lensing power spectrum alone. We consider the upcoming Subaru Hyper Suprime-Cam survey with an area of 1500 deg^2.

except $\boldsymbol{p} = (m_{3/2}, 10^9 A_s, n_s, \Omega_c h^2, w_0)$.

6.4.3 Forecast for future surveys

We provide the forecast for upcoming weak lensing surveys with an area coverage of more than a thousand square degrees. We use logarithmically spaced bins with $\Delta \log_{10} \ell = 0.1$ from $\ell = 100$ to 2000. We thus need a 14×14 covariance matrix of lensing power spectrum in the Fisher analysis. Our 1000 mock observations are sufficiently large to estimate the covariance matrix accurately.

Figure 6.5 shows the two-dimensional confidence contours for the Subaru Hyper Suprime-Cam (HSC) lensing survey [3]. We assume $n_{\rm gal} = 10$ arcmin^{-2}. The red circles show the constraints with 68 % confidence level (1σ) whereas the blue ones correspond to 95 % confidence level (2σ). The marginalized 1σ error for $m_{3/2}$ over other parameters is found to be ~ 18 eV. Note that this is a constraint from the lensing survey alone. We also show the forecast with the CMB priors in Figure 6.6. The constraint on the gravitino mass is significantly improved in this case, because using the CMB data breaks some degeneracies among cosmological parameters, e.g. $10^9 A_s$ and $\Omega_c h^2$ [189]. It is impressive that we can derive constraint on the gravitino mass with a level of 1 eV by combining data from the HSC lensing survey and the Planck mission.

6.4.4 Degeneracy between massive neutrino

It is well known that massive neutrinos affect the lensing power spectrum in a similar way to the light gravitino; free-streaming of massive neutrinos suppress the growth of structure. At large length scales, the effect on $P_\delta(k)$ has been quantified by linear theory and extensions to first-order perturbation theory, e.g. [236, 237]. Probing the effect of massive neutrinos on $P_\delta(k)$ in the fully non-linear regime is still challenging, because it is difficult to include the relativistic species in N-body simulations [238, 239, 240, 3]. In order to study the degeneracy between the light gravitino

[3] http://www.naoj.org/Projects/HSC/j_index.html

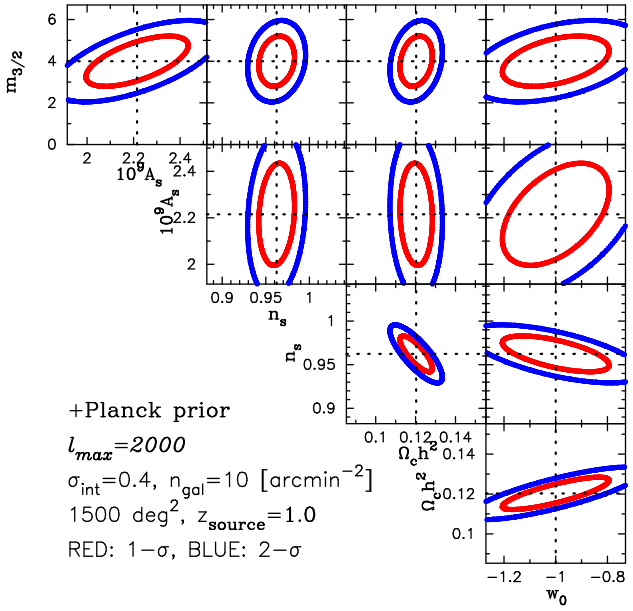

Figure 6.6: As for Figure 6.5, but with the CMB priors described in Section 5.2.

mass and the total mass of massive neutrinos in the cosmological parameter estimate, we utilize a fitting model of $P_\delta(k)$ that include the effect of neutrinos [3].

Figure 6.7 shows the effect of massive neutrinos on the lensing power spectrum. There, we assume the mass of neutrino $m_{\nu,\mathrm{tot}} = 0.7$ eV, which is comparable to the current upper limits with 95 percent confidence [13, 241, 242]. We compare the lensing power spectrum with those of the light gravitino with $m_{3/2} = 4$ and 16 eV. As expected, massive neutrinos with $m_{\nu,\mathrm{tot}} = 0.7$ eV causes a similar effect on the lensing power spectrum to that of the light gravitino. It would thus be difficult to break the degeneracy between the contribution of the light gravitino and that of massive neutrinos by a weak lensing survey alone. We need other probes of the matter distribution at large scales and at different epochs, such as galaxy clustering. For example, future galaxy redshift surveys are aimed at measuring the galaxy clustering at $k \sim 0.01 - 0.1$ h/Mpc. At the quasi-nonlinear scales, the effect of massive neutrinos on $P_\delta(k)$ can be distinguishable from that of the light gravitino, as shown in the right panel of Figure 6.7.

6.5 Summary and Discussion

The gravitino mass is one of the fundamental parameters in SUSY theory that is directly related to the SUSY breaking energy scale. We focus on the gauge-mediated supersymmetry breaking model that generically predicts the existence of light gravitinos with $m_{3/2} \sim$eV-keV. Free-streaming of such light gravitino affects the matter distribution significantly, leaving characteristic suppression in the matter power spectrum at around $k \gtrsim 0.1\,\mathrm{h/Mpc}$. The nonlinear scale is beyond the reach of the CMB anisotropy measurements. We show that observations of weak gravitational lensing can be used to probe the matter distribution at the relevant length scales and thus can be used to detect the imprints of the light gravitino.

We have explored cosmological constraints on the light gravitino mass from cosmic shear statistics. Our ray-tracing simulations have revealed that the conventional model for nonlinear correction to the matter power spectrum [2] does not work well for models with the light gravitino. The dif-

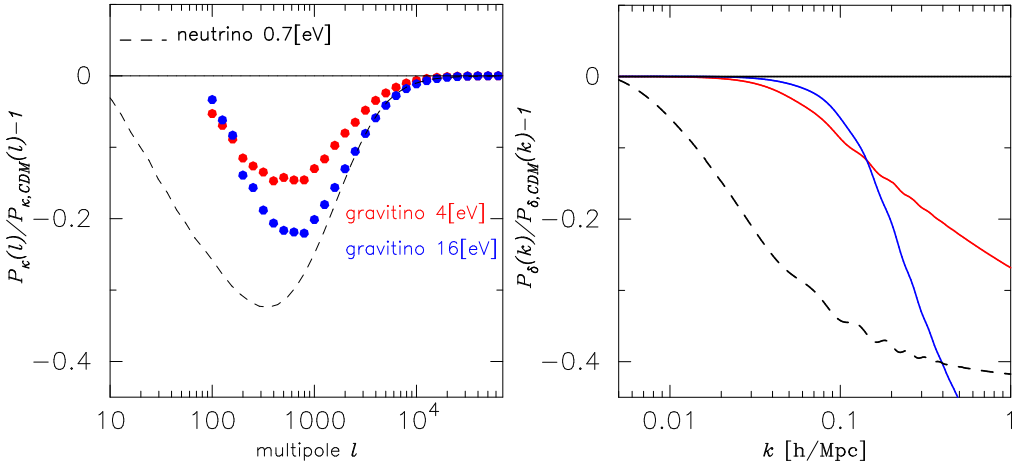

Figure 6.7: The effect of the light gravitino and massive neutrinos on the lensing power spectrum (left) and on the three dimensional matter power spectrum at $z = 0$ (right). In each panel, the dashed line shows the resulting lensing power spectrum calculated by the fitting model in [3] including the effect of massive neutrinos. We assume $m_{\nu,\mathrm{tot}} = 0.7$ eV. The points show the measured power spectra from our simulations in the case of $m_{3/2} = 4$ eV (red) and $m_{3/2} = 16$ eV (blue). We show these power spectra normalized by that for the pure CDM model.

ference between the simulation results and the fitting formula is significant at $\ell \sim 1000$, where upcoming lensing surveys are aimed at measuring the power spectrum accurately. Using a large set of ray-tracing simulations, we have shown that the HSC like survey has a potential to determine the gravitino mass with an accuracy of 4 ± 1 eV with the help of Planck CMB priors on the basic cosmological parameters.

Let us further discuss prospects for future lensing surveys. For the upcoming survey with 20000 deg^2 by the Large Synoptic Survey Telescope (LSST) [4], we will be able to use fainter galaxies for lensing analysis. Effectively the number of source galaxies will be larger. In this case, we can constrain on $m_{3/2}$ with a level of 4 ± 0.6 eV assuming $n_{\mathrm{gal}} = 15$ arcmin^{-2}. Note that the constraint is tighter than the current one from the Lyman-α forest by a factor of ~ 10 [47], and also comparable to the forecast that utilizes CMB lensing [185]. Although there is some certain degeneracy between the effect of massive neutrinos and that of the light gravitino in cosmic shear power spectrum, we argue that combining cosmic shear and galaxy clustering and/or CMB lensing can break the degeneracy. We summarize the forecast of $m_{3/2}$ from upcoming weak lensing survey in figure 6.8. There, we estimate the future constraint on the gravitino mass from the LHC 14 TeV run for the minimal GMSB model.

Ultimately, the International Linear Collider (ILC) experiment has a potential to determine the gravitino mass. When the next lightest supersymmetric particle is stau, its lifetime is proportional to the gravitino mass squared. By measuring the distribution of the impact parameter, one can evaluate the stau lifetime and hence the gravitino mass [243]. [5] Overall, under reasonable assumptions, almost all of the interesting GMSB models with $m_{3/2} < 5$ eV can be probed in 15 fb^{-1} of LHC 14 TeV run. Combining cosmological and collider searches together, we will reach the conclusion about the GMSB model.

[4] http://www.lsst.org/lsst/

[5] To this end, the center of mass energy should exceed two time the stau mass and the background events should be effectively eliminated. However, this may be challenging for the present design of the ILC in the case of the heavy stau for a given gravitino mass, i.e. large N_5 and λx.

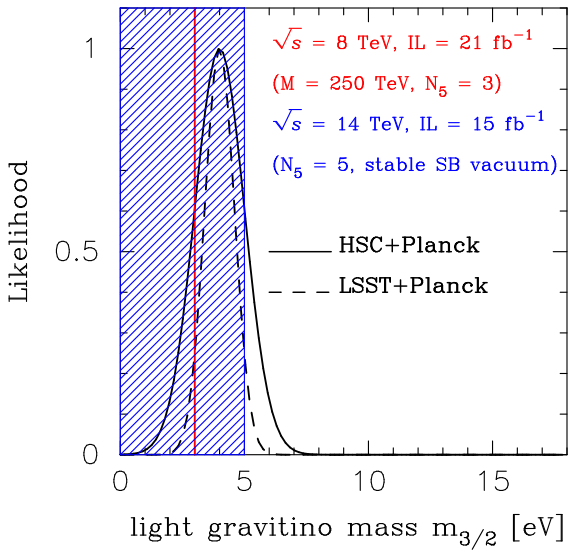

Figure 6.8: The likelihood distribution of $m_{3/2}$ expected by future weak lensing surveys. We have used the binned lensing power spectrum with the CMB prior for this figure. The solid line corresponds to the Hyper Suprime-Cam survey and the dashed one is for Large Synoptic Survey Telescope. The vertical lines show the current/future focus points of the GMSB model at the LHC (Table 6.1). In the near-future LHC, all GMSB models with $m_{3/2} < 5\,\mathrm{eV}$ (shaded region) can be probed if they involve the stable SUSY breaking (SB) vacuum and the successful grand unification.

Chapter 7

Summary and Conclusions

In this thesis, we investigated imprints of dark matter properties on small-scale density perturbations. Although cold dark matter model is currently popular, particle physics candidates of dark matter is not completely cold and dark. In the structure formation with the realistic candidates, the large-scale density perturbations are almost the same with CDM, but small-scale ones are not. Therefore, the deviation in the matter power spectra from CDM contains information of particle physical properties of dark matter.

In Chapter 2, we briefly reviewed the basic equations that describes evolution of the Universe. Since the matter and energy couples with the gravity only through the energy-momentum tensor, fluid dynamical approximation gives a closed form of evolution equation. For free-streaming particles, the fluid dynamical approximation is not valid and hence we should solve the full Boltzmann hierarchy.

In Chapter 3, we studied the structure formation in WDM models and in models with long-lived CHAMPs. Not only does the imprint on the matter power spectrum give us valuable information about the nature of dark matter, but also it may resolve the problems in the formation of small-scale structure (SSS) in ΛCDM model ("small-scale crisis"). One possible solution to "small-scale crisis" is warm dark matter (WDM). The thermal velocity of WDM behaves like effective "pressure" of dark matter fluid and suppress the gravitational growth of small-scale matter density fluctuations. Several WDM candidates are suggested in the well-motivated particle physics models (e.g. light gravitino, sterile neutrino). In these models, the WDM particles are produced in different ways. On the other hand, the astrophysical/cosmological constraints (e.g. by the Lyα absorption lines in emission spectra from high-redshift quasars) on WDM is usually reported in terms of the light gravitino mass. It should be clarified how the WDM matter power spectra in different WDM models can be related. To this end, we introduced two quantities, the fraction of warm dark matter $r_{\rm warm}$ and the Jeans scale at the matter-radiation equality $k_{\rm J}$. We also considered the long-lived Charged Massive Particle model. CHAMP naturally appears in the physics beyond the standard model such as GUT. CHAMP decays into a neutral particle, which becomes dark matter. The acoustic oscillation between CHAMPs, baryons and CMB lasts until CHAMP decays. In the long-lived CHAMP model, the cut-off scale is determined by the horizon scale at the decay of CHAMP $k_{\rm Ch}$. From the simulated matter distribution, we found that the cut-off scale $k_{\rm cut}$ characterizes the matter distribution in WDM models and long-lived CHAMP model even after non-linear growth of structure of the Universe. We compared the radial distribution of subhalos in simulated Milky Way-like halos with the one of observed satellites. From this comparison, We concluded that WDM models and long-lived CHAMP model can resolve the "missing satellite problem" when the cut-off scale takes a value in $k_{\rm cut} \sim 20 - 200\,{\rm Mpc}^{-1}$.

In Chapter 4, we studied imprints of non-thermal wino dark matter on small-scale structure. The

wino, which is the supersymmetric partner of the weak boson, is now well-motivated candidate of dark matter. Due to the observed relatively large Higgs mass and null-detection of SUSY particles, high-scale SUSY-breaking models are considered to be promising. In high-scale SUSY breaking models with the gravitino mass of $m_{3/2} \sim \mathcal{O}(10 - 1000)\,\mathrm{TeV}$, the gravitino decays before the Big Bang Nucleosynthesis (BBN) and thus does not cause any cosmological problem. The so-called Polony (moduli) problem is also ameliorated if models do not involve any singlet scalar field. As a result of the absence of singlet SUSY-breaking field, the gaugino masses are induced only at loop level, i.e. the anomaly mediated contribution and the higgsino threshold correction. Therefore, the wino is generically LSP in high-scale SUSY breaking models. The thermal relic of the wino LSP can account for the observed dark matter density for the relatively large wino mass $m_{\tilde{w}} \simeq 2.7\,\mathrm{TeV}$. The wino dark matter with $m_{\tilde{w}} \lesssim 2.7\,\mathrm{TeV}$ should be produced non-thermally. This is owing to the efficient self- and co-annihilation of the wino with the charged winos. The large annihilation cross section of the wino dark matter also makes it promising to search high-energy cosmic rays produced by the annihilation of the wino dark matter (indirect detection). Furthermore, we have a chance to determine the wino mass in the indirect detection since the annihilation cross section depends only on the wino mass. On the other hand, indirect detection generically suffers from an ambiguity in dark matter distribution in target objects. The dark matter distribution has been estimated from N-body simulations in ΛCDM model. Therefore, it should be clarified to what extent the wino dark matter satisfies the hypothesis of CDM, because the wino dark matter with $m_{\tilde{w}} \lesssim 2.7\,\mathrm{TeV}$ is produced non-thermally. To this end, we studied the "warmness" of the wino dark matter produced in the late time decay of the gravitino. Taking into account the energy loss processes, we solved the time evolution of the wino momentum spectrum. Then, we calculated the two quantities r_{warm} and k_{cut}. The results showed that large fraction (> 0.99) of the wino dark matter is cold component in the parameter region allowed by the gluino search in the LHC. Therefore, distribution of the wino dark matter in dark mater halos can be estimated by N-body simulations in ΛCDM model. We also showed that the warm component (~ 0.01) of the wino dark matter leaves imprints on the small-scale matter power spectra which may be probed by future observations of redshifted 21 cm e.g. in the FFT Telescope.

In Chapter 5, we studied imprints of non-thermal wino dark matter on small-scale structure. Wee studied the bino-wino co-annihilation scenario in high-scale SUSY breaking models. While there is still large ambiguity in the dark matter distribution at and background emission from the Galactic center, large annihilation cross section of the wino dark mater is now in tension with γ-ray observations in the Fermi-LAT and the H.E.S.S. telescope. On the other hand, the interaction of the bino LSP is highly suppressed in high-scale SUSY breaking models. The bino dark matter evade the γ-ray constraints, but its thermal relic abundance may over-close the Universe. We considered the bino LSP accompanied by the slightly heavier wino NLSP. The existence of the winos at the freeze-out of the bino reduces the thermal relic abundance of the bino dark matter (co-annihialtion). Taking into account the co-annihilation and the Sommerfeld enhancement, I identify the required mass splitting between the bino and the wino for a given thermal relic abundance of the bino dark matter. In the case of $r_{\mathrm{T}}\,(\equiv \Omega_{\tilde{b}}^{\mathrm{T}}/\Omega_{\mathrm{dm}}) < 1$, the bino dark matter should be produced non-thermally. Assuming the late time decay of the gravitino is in charge, We performed the similar analysis to in Chapter 4. We found that $1 - 50\,\%$ $(1 - 10\,\%)$ of the non-thermal bino dark matter behaves as warm component for $r_{\mathrm{T}} = 0.5\,(0.1)$.

The gravitino mass is one of the fundamental parameters in SUSY theory that is directly related to the SUSY breaking energy scale. We focused on the gauge-mediated supersymmetry breaking model that generically predicts the existence of light gravitinos with $m_{3/2} \sim$ eV-keV. In Chapter 6, we have explored cosmological constraints on the light gravitino mass from cosmic shear statistics. Using a large set of ray-tracing simulations, we have shown that the HSC like survey

has a potential to determine the gravitino mass with an accuracy of $4 \pm 1\,\mathrm{eV}$ with the help of Planck CMB priors on the basic cosmological parameters. Under reasonable assumptions, almost all of the interesting GMSB models with $m_{3/2} < 5\,\mathrm{eV}$ can be probed in $15\,\mathrm{fb}^{-1}$ of LHC $14\,\mathrm{TeV}$ run. Combining cosmological and collider searches together, we will reach the conclusion about the GMSB model.

Appendix A

Formulas of special functions

In this appendix, we summarize the formulas of the special functions that are used in chapter 2.

A.1 Legendre polynomial

— Rodrigues' formula —

$$P_l(x) = \frac{1}{2^l l!} \frac{d^l}{dx^l} \left[(x^2 - 1)^l \right] , \tag{A.1}$$

where $l! = \Gamma(l+1) = l \cdot (l-1) \cdots 2 \cdot 1$.
— Orthogonal relation —

$$\int_{-1}^{1} dx\, P_l(x) P_{l'}(x) = \delta_{l\,l'} \frac{2}{2l+1} \tag{A.2}$$

— Recurrance relation —

$$x P_l(x) = \frac{1}{2l+1} \left[(l+1) P_{l+1}(x) + l P_{l-1}(x) \right] \tag{A.3}$$

Appendix B

Partial Decay Widths of the Gauginos

In this appendix, we calculate the partial decay widths of the gluino and the bino produced by the decay of the gravitino used in section 4.2.

B.1 Partial decay widths of the gluino

The gluino decays into the winos and the bino through the three-body decays, $\tilde{g} \to q + \bar{q} + \tilde{w}$. The spin averaged and color summed partial decay width of the neutral wino mode is given by,

$$\begin{aligned}\frac{d\Gamma_{\tilde{g}\to\tilde{w}}}{dE_{\tilde{w}}} &= \frac{2}{3\cdot(8\pi)^3}\frac{g_3^2 g_2^2}{m_{\rm squark}^4}\frac{m_{\tilde{g}}^6}{p_{\tilde{g}}E_{\tilde{g}}}\Big(2r_{\tilde{w}}(3c_{\tilde{w}}-2r_{\tilde{w}}+3c_{\tilde{w}}r_{\tilde{w}}^2)(\epsilon_{\tilde{w},\rm CM,upper}-\epsilon_{\tilde{w},\rm CM,lower}) \\ &\quad +3(1-2c_{\tilde{w}}r_{\tilde{w}}+r_{\tilde{w}}^2)(\epsilon_{\tilde{w},\rm CM,upper}^2-\epsilon_{\tilde{w},\rm CM,lower}^2) \\ &\quad -\frac{8}{3}(\epsilon_{\tilde{w},\rm CM,upper}^3-\epsilon_{\tilde{w},\rm CM,lower}^3)\Big)\ , \end{aligned} \tag{B.1}$$

where g's are the gauge coupling constants, $p_{\tilde{g}}$ is the size of the three-dimensional momentum of the gluino, $r_{\tilde{w}}$ is the mass ratio $r_{\tilde{w}} = m_{\tilde{w}}/m_{\tilde{g}}$, and $c_{\tilde{w}}$ is the relative phase $c_{\tilde{w}} = \cos(\arg[m_{\tilde{w}}/m_{\tilde{g}}])$. In our analysis, we neglect the masses of the standard model fermion for simplicity.

In the above expression, we have introduced ϵ's which are defined by

$$\epsilon_{\tilde{w},\rm CM,\,lower} = \frac{E_{\tilde{g}}E_{\tilde{w}}-p_{\tilde{g}}p_{\tilde{w}}}{m_{\tilde{g}}^2}\ , \tag{B.2}$$

$$\epsilon_{\tilde{w},\rm CM,\,upper} = \frac{m_{\tilde{g}}^2+m_{\tilde{w}}^2}{2m_{\tilde{g}}^2}\ , \tag{B.3}$$

for a highly boosted gluino, i.e. $m_{\tilde{g}} > (m_{\tilde{g}}^2+m_{\tilde{w}}^2)/2E_{\tilde{g}}$. For $m_{\tilde{g}} > (m_{\tilde{g}}^2+m_{\tilde{w}}^2)/2E_{\tilde{g}}$, the wino energy in the boosted gluino frame is in between

$$E_{\tilde{w}}^- = \frac{E_{\tilde{g}}(m_{\tilde{g}}^2+m_{\tilde{w}}^2)-p_{\tilde{g}}(m_{\tilde{g}}^2-m_{\tilde{w}}^2)}{2m_{\tilde{g}}^2}\ , \tag{B.4}$$

$$E_{\tilde{w}}^+ = \frac{E_{\tilde{g}}(m_{\tilde{g}}^2+m_{\tilde{w}}^2)+p_{\tilde{g}}(m_{\tilde{g}}^2-m_{\tilde{w}}^2)}{2m_{\tilde{g}}^2}\ . \tag{B.5}$$

For a less boosted gluino, i.e. $m_{\tilde{w}} < (m_{\tilde{g}}^2 + m_{\tilde{w}}^2)/2E_{\tilde{g}}$, on the other hand, ϵ's are defined by,

$$\epsilon_{\tilde{w},\mathrm{CM,\,lower}} = \frac{E_{\tilde{g}}E_{\tilde{w}} - p_{\tilde{g}}p_{\tilde{w}}}{m_{\tilde{g}}^2} , \tag{B.6}$$

$$\epsilon_{\tilde{w},\mathrm{CM,\,upper}} = \begin{cases} \dfrac{E_{\tilde{g}}E_{\tilde{w}} + p_{\tilde{g}}p_{\tilde{w}}}{m_{\tilde{g}}^2} & (E_{\tilde{w}} < E_{\tilde{w}}^-) , \\ \dfrac{m_{\tilde{g}}^2 + m_{\tilde{w}}^2}{2m_{\tilde{g}}^2} & (E_{\tilde{w}} > E_{\tilde{w}}^-) , \end{cases} \tag{B.7}$$

and the wino energy is in between $m_{\tilde{w}}$ and $E_{\tilde{w}}^+$ in the boosted gluino frame. In our application, the gluino produced by the gravitino decay is highly boosted, and hence, we use ϵ's in Eqs. (B.2) and (B.3). By integrating the above partial width in between $E_{\tilde{w}}^{\pm}$, we obtain the total decay width into the neutral wino,

$$\begin{aligned} \Gamma_{\tilde{g}\to\tilde{w}} = {} & \frac{4g_2^2 g_3^2}{3(16\pi)^3}\frac{m_{\tilde{g}}^6}{E_{\tilde{g}} m_{\mathrm{squark}}^4}\Big((1-r_{\tilde{w}}^2)\left(1-7r_{\tilde{w}}^2-7r_{\tilde{w}}^4+r_{\tilde{w}}^6+2c_{\tilde{w}}(r_{\tilde{w}}+10r_{\tilde{w}}^3+r_{\tilde{w}}^5)\right) \\ & +24r_{\tilde{w}}^3(c_{\tilde{w}} - r_{\tilde{w}}c_{\tilde{w}} - r_{\tilde{w}} + c_{\tilde{w}}r_{\tilde{w}}^2)\ln r_{\tilde{w}}\Big) . \end{aligned} \tag{B.8}$$

Similarly, we obtain the decay width of the gluino into the bino via the three body decays,

$$\begin{aligned} \Gamma_{\tilde{g}\to\tilde{b}} = {} & \frac{44g_1^2 g_3^2}{45(16\pi)^3}\frac{m_{\tilde{g}}^6}{E_{\tilde{g}} m_{\mathrm{squark}}^4}\Big(\left(1-r_{\tilde{b}}^2\right)\left(1-7r_{\tilde{b}}^2-7r_{\tilde{b}}^4+r_{\tilde{b}}^6+2c_{\tilde{b}}(r_{\tilde{b}}+10r_{\tilde{b}}^3+r_{\tilde{b}}^5)\right) \\ & +24r_{\tilde{b}}^3\left(c_{\tilde{b}} - r_{\tilde{b}}c_{\tilde{b}} - r_{\tilde{b}} + c_{\tilde{b}}r_{\tilde{b}}^2\right)\ln r_{\tilde{b}}\Big) , \end{aligned} \tag{B.9}$$

where $r_{\tilde{b}} = m_{\tilde{b}}/m_{\tilde{g}}$. The partial width is also obtained,

$$\begin{aligned} \frac{d\Gamma_{\tilde{g}\to\tilde{b}}}{dE_{\tilde{b}}} = {} & \frac{22}{45(8\pi)^3}\frac{g_3^2 g_1^2}{m_{\mathrm{squark}}^4}\frac{m_{\tilde{g}}^6}{p_{\tilde{g}}E_{\tilde{g}}}\Big(2r_{\tilde{b}}(3c_{\tilde{b}} - 2r_{\tilde{b}} + 3c_{\tilde{b}}r_{\tilde{b}}^2)(\epsilon_{\tilde{b},\mathrm{CM,upper}} - \epsilon_{\tilde{b},\mathrm{CM,lower}}) \\ & +3(1-2c_{\tilde{b}}r_{\tilde{b}} + r_{\tilde{b}}^2)(\epsilon_{\tilde{b},\mathrm{CM,upper}}^2 - \epsilon_{\tilde{b},\mathrm{CM,lower}}^2) \\ & -\frac{8}{3}(\epsilon_{\tilde{b},\mathrm{CM,upper}}^3 - \epsilon_{\tilde{b},\mathrm{CM,lower}}^3)\Big) . \end{aligned} \tag{B.10}$$

Here, ϵ's are obtained by replacing $\tilde{w}$ with $\tilde{b}$ in Eqs. (B.2) and (B.3), and $c_{\tilde{b}} = \cos(\arg[m_{\tilde{b}}/m_{\tilde{g}}])$. By remembering that the wino is a triplet, the branching ratio of the bino mode is given by,

$$Br_{\tilde{g}\to\tilde{b}} = \frac{\Gamma_{\tilde{g}\to\tilde{b}}}{3\Gamma_{\tilde{g}\to\tilde{w}} + \Gamma_{\tilde{g}\to\tilde{b}}} , \tag{B.11}$$

which is less than about 10 % in the parameter space we are interested in.

B.2 Partial decay widths of the bino

The main decay modes of the bino are the two-body decay into the neutral wino, $\tilde{b} \to h + \tilde{w}$ and the ones into the charged wino, $\tilde{b} \to W^{\pm} + \tilde{w}^{\mp}$. To calculate the decay widths, let us define the mass eigenstates of the neutralino mass matrix,

$$M_{\mathrm{neut}} = \begin{pmatrix} M_1 & 0 & -c_\beta s_W m_Z & s_\beta s_W m_Z \\ 0 & M_2 & c_\beta c_W m_Z & -s_\beta c_W m_Z \\ -c_\beta s_W m_Z & c_\beta c_W m_Z & 0 & -\mu \\ s_\beta s_W m_Z & -s_\beta c_W m_Z & -\mu & 0 \end{pmatrix} , \tag{B.12}$$

and the chargino mass matrix,

$$M_{\rm ch} = \begin{pmatrix} M_2 & \sqrt{2}c_\beta c_W m_Z \\ \sqrt{2}s_\beta c_W m_Z & \mu \end{pmatrix} . \tag{B.13}$$

where $M_{1,2}$ denotes the gaugino masses, μ is the μ-term, $s_\beta = \sin\beta$, $c_\beta = \cos\beta$, and the subscript W denotes the Weinberg angle.

The mass eigenstates up to $O(m_Z^2/\mu^2)$ are given by,

$$\begin{aligned}
\tilde{b} &= -\frac{s_{2\beta}s_{2W}m_Z^2}{2(M_1-M_2)\mu}\,\chi_1^0 + \chi_2^0 + O(m_Z^2/\mu^2) , && \text{(B.14)}\\
\tilde{w}^0 &= \chi_1^0 + \frac{s_{2\beta}s_{2W}m_Z^2}{2(M_1-M_2)\mu}\,\chi_2^0 + O(m_Z^2/\mu^2) , && \text{(B.15)}\\
\tilde{H}_d^0 &= -\frac{s_\beta c_W m_Z}{\mu}\,\chi_1^0 + \frac{s_\beta s_W m_Z}{\mu}\,\chi_2^0 + \chi_3^0 + O(m_Z^2/\mu^2) , && \text{(B.16)}\\
\tilde{H}_u^0 &= \frac{c_\beta c_W m_Z}{\mu}\,\chi_1^0 - \frac{c_\beta s_W m_Z}{\mu}\,\chi_2^0 + \chi_4^0 + O(m_Z^2/\mu^2) , && \text{(B.17)}
\end{aligned}$$

for the neutralinos, and

$$\begin{aligned}
\tilde{w}^\pm &= \chi_1^\pm + O(m_Z^2/\mu^2) , && \text{(B.18)}\\
\tilde{H}_d^- &= -\sqrt{2}\frac{c_\beta c_W m_Z}{\mu}\chi_1^- + \chi_2^- + O(m_Z^2/\mu^2) , && \text{(B.19)}\\
\tilde{H}_u^+ &= -\sqrt{2}\frac{s_\beta c_W m_Z}{\mu}\chi_1^+ + \chi_2^+ + O(m_Z^2/\mu^2) . && \text{(B.20)}
\end{aligned}$$

for the charginos.

In these bases, the mass eigenvalues are given by,

$$\begin{aligned}
m_{\chi_1^0} &= M_2 - \frac{s_{2\beta}c_W^2 m_Z^2}{\mu} + O(m_Z^3/\mu^2) ,\\
m_{\chi_2^0} &= M_1 - \frac{s_{2\beta}s_W^2 m_Z^2}{\mu} + O(m_Z^3/\mu^2) ,\\
m_{\chi_3^0} &= \mu + O(m_Z^3/\mu^2) ,\\
m_{\chi_4^0} &= \mu + O(m_Z^3/\mu^2) , && \text{(B.21)}
\end{aligned}$$

and

$$\begin{aligned}
m_{\chi_1^\pm} &= M_2 - \frac{s_{2\beta}c_W^2 m_Z^2}{\mu} + O(m_Z^3/\mu^2) , && \text{(B.22)}\\
m_{\chi_2^\pm} &= \mu + O(m_Z^3/\mu^2) . && \text{(B.23)}
\end{aligned}$$

In the followings, we call χ_1^0 the neutral wino, χ_2^0 the bino, and $\chi_1^\pm$ the charged wino.

In terms of these mass eigenstates, the neutral wino-bino-Higgs couplings, i.e. χ_1^0-χ_2^0-h, are obtained from the gaugino-higgsino-Higgs interactions, which lead to

$$\begin{aligned}
\mathcal{L}_{\chi_1^0-\chi_2^0-h} &= -\frac{g s_W s_{2\beta} m_Z}{\mu}\,h\,\chi_1^0\,\chi_2^0 + c.c.\\
&= -\frac{g s_W s_{2\beta} m_Z}{\mu}\,h\,\bar{\Psi}_1^0\,\Psi_2^0 . && \text{(B.24)}
\end{aligned}$$

In the final expression, we have used the four component Majorana fermions. The charged wino-bino-W-boson interactions are obtained from the gauge interactions of the wino leading to,

$$\begin{aligned}\mathcal{L}_{\chi_1^\pm-\chi_2^0-W^\mp} &= g\frac{s_{2\beta}s_{2W}m_Z^2}{2(M_1-M_2)\mu}(-\tilde{\chi}_1^{+\dagger}\sigma^\mu\tilde{b}W_\mu^+ + \tilde{\chi}_1^{-\dagger}\sigma^\mu\tilde{b}W_\mu^- \\ &\quad + \tilde{b}^\dagger\sigma^\mu\tilde{\chi}_1^-W_\mu^+ - \tilde{b}^\dagger\sigma^\mu\tilde{\chi}_1^+W_\mu^-) \qquad \text{(B.25)} \\ &= -g\frac{s_{2\beta}s_{2W}m_Z^2}{2(M_1-M_2)\mu}(\bar{\Psi}_1^+\gamma^\mu W_\mu^+\Psi_2^0 + \bar{\Psi}_2^0\gamma^\mu W_\mu^-\Psi_1^+)\ . \qquad \text{(B.26)}\end{aligned}$$

From these interactions, we obtain the decay widths of the bino, As a result, we obtain the decay width,

$$\begin{aligned}\Gamma_{\tilde{b}\to h+\tilde{w}} &= \frac{1}{16\pi}\left(\frac{gm_Zs_{2\beta}s_W}{\mu}\right)^2 M_1\left(1+2\frac{M_2}{M_1}+\frac{M_2^2}{M_1^2}-\frac{m_h^2}{M_1^2}\right) \\ &\quad\times\left(1-\frac{(M_2+m_h)^2}{M_1^2}\right)^{1/2}\left(1-\frac{(M_2-m_h)^2}{M_1^2}\right)^{1/2}\ , \qquad \text{(B.27)} \\ \Gamma_{\tilde{b}\to W^\pm+\tilde{w}^\mp} &= \frac{1}{16\pi}\left(\frac{gm_Zs_{2\beta}s_W}{\mu}\right)^2 M_1\left(1-\frac{M_2}{M_1}\right)^{-2} \\ &\quad\times\left(\left(1-\frac{M_2^2}{M_1^2}+\frac{m_W^2}{M_1^2}\right)\left(1-\frac{M_2^2}{M_1^2}-\frac{m_W^2}{M_1^2}\right)+\frac{m_W^2}{M_1^2}\left(1-6\frac{M_2}{M_1}+\frac{M_2^2}{M_1^2}-\frac{m_W^2}{M_1^2}\right)\right) \\ &\quad\times\left(1-\frac{(M_2+m_W)^2}{M_1^2}\right)^{1/2}\left(1-\frac{(M_2-m_W)^2}{M_1^2}\right)^{1/2}\ . \qquad \text{(B.28)}\end{aligned}$$

Notice that these decay widths coincides in the limit of $M_{1,2} \gg m_{W,h}$,

$$\Gamma_{\tilde{b}\to h+\tilde{w}} = \Gamma_{\tilde{b}\to W^\pm+\tilde{w}^\mp} = \frac{1}{16\pi}\left(\frac{gm_Zs_{2\beta}s_W}{\mu}\right)^2 M_1\left(1+\frac{M_2}{M_1}\right)^2\left(1-\frac{M_2^2}{M_1^2}\right)\ , \qquad \text{(B.29)}$$

up to $O(m_{h,W}^2/M_1^2)$ corrections, which exemplifies the equivalence theorem. With the equivalence theorem, in our mind, we simplify our analysis by fixing $Br_{\tilde{b}\to\tilde{w}^0} \simeq 1/3$.

Since the bino decay into the neutral wino is the two-body decay, the energy distribution of the neutral wino is a flat distribution as shown in Fig. 4.2 in between,

$$\begin{aligned}E_{\tilde{w}}^{\max} &= \frac{E_{\tilde{b}}}{m_{\tilde{b}}}E_{\tilde{w}}^{\rm CM} + \frac{p_{\tilde{b}}}{m_{\tilde{b}}}p_{\tilde{w}}^{\rm CM}\ , \qquad \text{(B.30)} \\ E_{\tilde{w}}^{\min} &= \frac{E_{\tilde{b}}}{m_{\tilde{b}}}E_{\tilde{w}}^{\rm CM} - \frac{p_{\tilde{b}}}{m_{\tilde{b}}}p_{\tilde{w}}^{\rm CM}\ , \qquad \text{(B.31)}\end{aligned}$$

where $E_{\tilde{w}}^{\rm CM}$ and $p_{\tilde{w}}^{\rm CM}$ denote the energy and the size of the three-dimensional momentum in the rest frame of the bino which are given by,

$$\begin{aligned}E_{\tilde{w}}^{\rm CM} &= \frac{m_{\tilde{b}}^2+m_{\tilde{w}}^2-m_h^2}{2m_{\tilde{b}}}\ , \qquad \text{(B.32)} \\ p_{\tilde{w}}^{\rm CM} &= \frac{\sqrt{(m_{\tilde{b}}^2-(m_{\tilde{w}}+m_h)^2)(m_{\tilde{b}}^2-(m_{\tilde{w}}-m_h)^2)}}{2m_{\tilde{b}}}\ . \qquad \text{(B.33)}\end{aligned}$$

Similarly, the charged wino distribution is given by replacing the Higgs boson masses with the W-boson mass. In our actual analysis, we set $m_h = m_W = 0$ which leads to harder wino in the

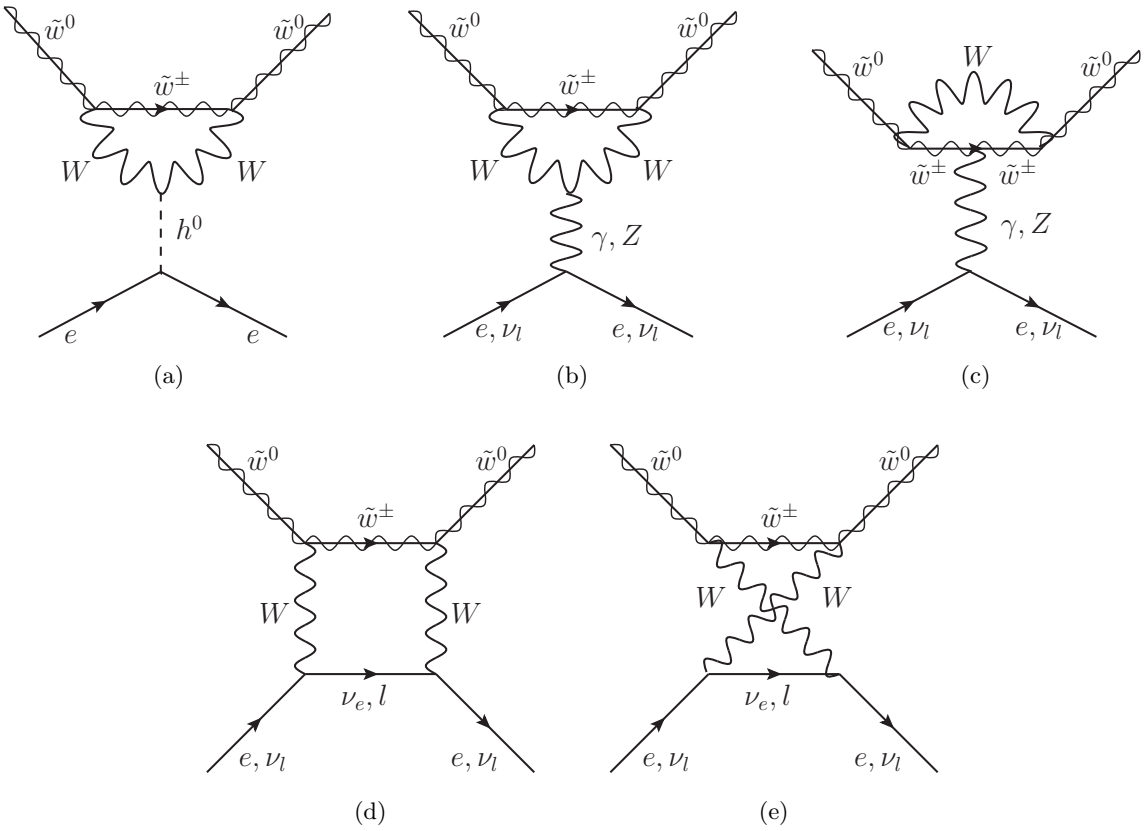

Figure B.1: *The one-loop diagrams which contribute to the elastic scattering between the neutral wino and the thermal background in the decoupling limit of the sfermions, the higgsinos and the heavy Higgses.*

cascade decays of the gravitinos. As we have discussed in section 4.2, the harder the initial wino is, the more likely it is converted to the charged wino which immediately loses its energy via the scattering processes with the thermal background. Therefore, this assumption gives us conservative estimations of possible imprints on the small-scale structure of the non-thermally produced wino dark matter.

B.3 Elastic scattering of the neutral wino at the one-loop level

In the decoupling limit of the sfermions, the higgsinos and the heavy Higgses, the neutral wino does not have any tree level elastic interaction with the thermal background. The one-loop diagrams shown in Fig. B.1 contribute to the elastic scattering between the neutral wino and the thermal background. The contribution of the light Higgs exchange diagram (Fig. B.1(a)) is negligible because the Yukawa coupling of the electron is small. The γ, Z-boson exchange diagrams (Fig. B.1(b), B.1(c)) originate from the one-loop correction to the $\tilde{w}^0 - \tilde{w}^0 - \gamma, Z$-boson vertex. The one-loop vertex correction consists of only vector-like interactions and vanishes by the charge-conjugation invariance.

Thus, we should consider only box diagrams (Fig. B.1(d), B.1(e)). In calculating the contribution of the box diagrams, we expand it by the incoming and the outgoing four-momenta of the thermal background particles in the loop. The incoming and the outgoing four-momenta of the

thermal background particles are of the order of $O(E_{\tilde{w}}T/m_{\tilde{w}})$ at the rest frame of the neutral wino and much smaller than the wino mass $m_{\tilde{w}}$ and the W-boson mass m_W. This allows us to adopt the leading order of the expansion. At the leading order, these diagrams yield an effective interaction,

$$\mathcal{L}_{\rm int}^{\rm eff} = \sum_{f=e,\,\nu_e,\,\nu_\mu,\,\nu_\tau} \frac{1}{2} g_{\rm loop}\left(\frac{m_W^2}{m_{\tilde{w}}^2}\right) G_F^2 m_W^2\, \bar{\tilde{w}}^0 \gamma_\mu \gamma_5 \tilde{w}^0\, \bar{f}\gamma^\mu P_L f \tag{B.34}$$

with

$$g_{\rm loop}(x) = \frac{1}{3\pi^2}\left(\frac{\sqrt{x}}{\sqrt{1-x/4}}(8-x-x^2)\arctan\left(\frac{2\sqrt{1-x/4}}{\sqrt{x}}\right) - x\,(2-(3+x)\ln x)\right). \tag{B.35}$$

In the above expression, we have used four component Majorana fermion for the neutral wino $\tilde{w}^0$. Using the above effective interaction, we can obtain the reaction rate of the elastic scattering,

$$\Gamma_{\tilde{w}^0,\,\rm elastic} = \frac{135}{\pi^3}\zeta(5) g_{\rm loop}^2\left(\frac{m_W^2}{m_{\tilde{w}}^2}\right) G_F^4 T^5 m_W^4 \frac{E_{\tilde{w}^0}^2}{m_{\tilde{w}}^2}\left(1+\frac{p_{\tilde{w}^0}^2}{E_{\tilde{w}^0}^2}\right). \tag{B.36}$$

Acknowledgments

First, I am grateful to my supervisor, Hitoshi Murayama. He provided me with an opportunity to spend my Ph.D. years in the unique environment, Kavli Institute for the Physics and Mathematics of the Universe (Kavli IPMU). He originally lead me to the interesting research area, astrophysical probes of dark matter properties. I wish to express my special gratitude to Naoki Yoshida. He is not only an excellent collaborator, but also good example as a researcher for me. He kindly supported and encouraged me throughout all my research life. I gratefully acknowledge my collaborators, Kohri Kazunori, Tomo Takahashi, Ibe Masahiro, Shigeki Matsumoto and Masato Shirasaki. Through the fruitful discussions with them, I learned many things in astrophysics, cosmology and particle physics. I am thankful to all of the members in Kavli IPMU, the University of Tokyo Theoretical Astrophysics Group (UTAP) and Research Center for the Early Universe (RESCEU).

This research is supported by the Japan Society for the Promotion of Science (JSPS) predoctoral research fellowship. The numerical simulations in this thesis were carried out in part at the Yukawa Institute Computer Facility, on Cray XC30 at Center for Computational Astrophysics, CfCA, of National Astronomical Observatory of Japan, and under the Interdisciplinary Computational Science Program in Center for Computational Sciences, University of Tsukuba.

Finally, I would like to express my special thanks to my family and friends. Without their perpetual understanding and warm help, I could not have been completed this thesis.

References

[1] Planck Collaboration Collaboration, P. Ade *et al.*, *Planck 2013 results. XVI. Cosmological parameters*, [arXiv:1303.5076]

[2] R. Takahashi, M. Sato, T. Nishimichi, A. Taruya and M. Oguri, *Revising the Halofit Model for the Nonlinear Matter Power Spectrum*, Astrophys.J. **761** (2012) 152, [arXiv:1208.2701]

[3] S. Bird, M. Viel and M. G. Haehnelt, *Massive Neutrinos and the Non-linear Matter Power Spectrum*, Mon.Not.Roy.Astron.Soc. **420** (2012) 2551–2561, [arXiv:1109.4416]

[4] G. Jungman, M. Kamionkowski and K. Griest, *Supersymmetric dark matter*, Phys.Rept. **267** (1996) 195–373, [hep-ph/9506380]

[5] G. Bertone, D. Hooper and J. Silk, *Particle dark matter: Evidence, candidates and constraints*, Phys.Rept. **405** (2005) 279–390, [hep-ph/0404175]

[6] WMAP Collaboration, G. Hinshaw *et al.*, *Nine-Year Wilkinson Microwave Anisotropy Probe (WMAP) Observations: Cosmological Parameter Results*, Astrophys.J.Suppl. **208** (2013) 19, [arXiv:1212.5226]

[7] Planck Collaboration Collaboration, P. Ade *et al.*, *Planck 2013 results. XVI. Cosmological parameters*, [arXiv:1303.5076]

[8] H. Murayama, *Physics Beyond the Standard Model and Dark Matter*, [arXiv:0704.2276]

[9] P. Fayet, *Supersymmetry and Weak, Electromagnetic and Strong Interactions*, Phys.Lett. **B64** (1976) 159

[10] P. Fayet, *Spontaneously Broken Supersymmetric Theories of Weak, Electromagnetic and Strong Interactions*, Phys.Lett. **B69** (1977) 489

[11] P. Fayet, *Relations Between the Masses of the Superpartners of Leptons and Quarks, the Goldstino Couplings and the Neutral Currents*, Phys.Lett. **B84** (1979) 416

[12] SDSS Collaboration Collaboration, M. Tegmark *et al.*, *Cosmological parameters from SDSS and WMAP*, Phys.Rev. **D69** (2004) 103501, [astro-ph/0310723]

[13] B. A. Reid, W. J. Percival, D. J. Eisenstein, L. Verde, D. N. Spergel *et al.*, *Cosmological Constraints from the Clustering of the Sloan Digital Sky Survey DR7 Luminous Red Galaxies*, Mon.Not.Roy.Astron.Soc. **404** (2010) 60–85, [arXiv:0907.1659]

[14] SDSS Collaboration Collaboration, W. J. Percival *et al.*, *Baryon Acoustic Oscillations in the Sloan Digital Sky Survey Data Release 7 Galaxy Sample*, Mon.Not.Roy.Astron.Soc. **401** (2010) 2148–2168, [arXiv:0907.1660]

[15] A. Kamada, N. Yoshida, K. Kohri and T. Takahashi, *Structure of Dark Matter Halos in Warm Dark Matter models and in models with Long-Lived Charged Massive Particles*, JCAP **1303** (2013) 008, [arXiv:1301.2744]

[16] M. Ibe, A. Kamada and S. Matsumoto, *Imprints of nonthermal Wino dark matter on small-scale structure*, Phys.Rev. **D87** (2013), no. 6, 063511, [arXiv:1210.0191]

[17] M. Ibe, A. Kamada and S. Matsumoto, *Mixed (Cold+Warm) Dark Matter in the Bino-Wino co-annihilation scenario*, [arXiv:1311.2162]

[18] A. Kamada, M. Shirasaki and N. Yoshida, *Weighing the Light Gravitino Mass with Weak Lensing Surveys*, [arXiv:1311.4323]

[19] L. D. Landau and E. M. Lifshitz, *Fluid mechanics*. 1959

[20] H. Kodama and M. Sasaki, *Cosmological Perturbation Theory*, Prog.Theor.Phys.Suppl. **78** (1984) 1–166

[21] J. M. Bardeen, *Gauge Invariant Cosmological Perturbations*, Phys.Rev. **D22** (1980) 1882–1905

[22] M. Sasaki, *Large Scale Quantum Fluctuations in the Inflationary Universe*, Prog.Theor.Phys. **76** (1986) 1036

[23] V. F. Mukhanov, *Quantum Theory of Gauge Invariant Cosmological Perturbations*, Sov.Phys.JETP **67** (1988) 1297–1302

[24] E. Lifshitz and I. Khalatnikov, *Investigations in relativistic cosmology*, Adv.Phys. **12** (1963) 185–249

[25] V. F. Mukhanov, H. Feldman and R. H. Brandenberger, *Theory of cosmological perturbations. Part 1. Classical perturbations. Part 2. Quantum theory of perturbations. Part 3. Extensions*, Phys.Rept. **215** (1992) 203–333

[26] C.-P. Ma and E. Bertschinger, *Cosmological perturbation theory in the synchronous and conformal Newtonian gauges*, Astrophys.J. **455** (1995) 7–25, [astro-ph/9506072]

[27] K. Yoshikawa, N. Yoshida and M. Umemura, *Direct Integration of the Collisionless Boltzmann Equation in Six-dimensional Phase Space: Self-gravitating Systems*, Astrophys.J. **762** (2013) 116, [arXiv:1206.6152]

[28] WMAP Collaboration Collaboration, E. Komatsu *et al.*, *Seven-Year Wilkinson Microwave Anisotropy Probe (WMAP) Observations: Cosmological Interpretation*, Astrophys.J.Suppl. **192** (2011) 18, [arXiv:1001.4538]

[29] B. Moore, S. Ghigna, F. Governato, G. Lake, T. R. Quinn *et al.*, *Dark matter substructure within galactic halos*, Astrophys.J. **524** (1999) L19–L22, [astro-ph/9907411]

[30] A. V. Kravtsov, *Dark matter substructure and dwarf galactic satellites*, Adv.Astron. **2010** (2010) 281913, [arXiv:0906.3295]

[31] M. Boylan-Kolchin, J. S. Bullock and M. Kaplinghat, *Too big to fail? The puzzling darkness of massive Milky Way subhaloes*, Mon.Not.Roy.Astron.Soc. **415** (2011) L40, [arXiv:1103.0007]

[32] M. R. Lovell, V. Eke, C. S. Frenk, L. Gao, A. Jenkins *et al.*, *The Haloes of Bright Satellite Galaxies in a Warm Dark Matter Universe*, Mon.Not.Roy.Astron.Soc. **420** (2012) 2318–2324, [arXiv:1104.2929]

[33] M. Boylan-Kolchin, J. S. Bullock and M. Kaplinghat, *The Milky Way's bright satellites as an apparent failure of LCDM*, Mon.Not.Roy.Astron.Soc. **422** (2012) 1203–1218, [arXiv:1111.2048]

[34] E. Papastergis, A. M. Martin, R. Giovanelli and M. P. Haynes, *The velocity width function of galaxies from the 40light on the cold dark matter overabundance problem*, Astrophys.J. **739** (2011) 38, [arXiv:1106.0710]

[35] P. Bode, J. P. Ostriker and N. Turok, *Halo formation in warm dark matter models*, Astrophys.J. **556** (2001) 93–107, [astro-ph/0010389]

[36] H. de Vega and N. Sanchez, *Model independent analysis of dark matter points to a particle mass at the keV scale*, Mon.Not.Roy.Astron.Soc. **404** (2010) 885, [arXiv:0901.0922]

[37] H. de Vega and N. Sanchez, *Constant surface gravity and density profile of dark matter*, Int.J.Mod.Phys. **A26** (2011) 1057–1072, [arXiv:0907.0006]

[38] H. de Vega, P. Salucci and N. Sanchez, *The mass of the dark matter particle from theory and observations*, New Astron. **17** (2012) 653–666, [arXiv:1004.1908]

[39] M. Viel, K. Markovic, M. Baldi and J. Weller, *The Non-Linear Matter Power Spectrum in Warm Dark Matter Cosmologies*, Mon.Not.Roy.Astron.Soc. **421** (2012) 50–62, [arXiv:1107.4094]

[40] R. M. Dunstan, K. N. Abazajian, E. Polisensky and M. Ricotti, *The Halo Model of Large Scale Structure for Warm Dark Matter*, [arXiv:1109.6291]

[41] A. Schneider, R. E. Smith, A. V. Maccio and B. Moore, *Nonlinear Evolution of Cosmological Structures in Warm Dark Matter Models*, [arXiv:1112.0330]

[42] N. Menci, F. Fiore and A. Lamastra, *Galaxy Formation in WDM Cosmology*, [arXiv:1201.1617]

[43] A. V. Maccio, S. Paduroiu, D. Anderhalden, A. Schneider and B. Moore, *Cores in warm dark matter haloes: a Catch 22 problem*, [arXiv:1202.1282]

[44] C. Destri, H. de Vega and N. Sanchez, *Fermionic warm dark matter produces galaxy cores in the observed scales because of quantum mechanics*, New Astron. **22** (2013) 39–50, [arXiv:1204.3090]

[45] D. Anderhalden, A. Schneider, A. V. Maccio, J. Diemand and G. Bertone, *Hints on the Nature of Dark Matter from the Properties of Milky Way Satellites*, JCAP **1303** (2013) 014, [arXiv:1212.2967]

[46] C. Destri, H. de Vega and N. Sanchez, *Quantum WDM fermions and gravitation determine the observed galaxy structures*, Astropart.Phys. **46** (2013) 14–22, [arXiv:1301.1864]

[47] M. Viel, J. Lesgourgues, M. G. Haehnelt, S. Matarrese and A. Riotto, *Constraining warm dark matter candidates including sterile neutrinos and light gravitinos with WMAP and the Lyman-alpha forest*, Phys.Rev. **D71** (2005) 063534, [astro-ph/0501562]

[48] A. Boyarsky, J. Lesgourgues, O. Ruchayskiy and M. Viel, *Lyman-alpha constraints on warm and on warm-plus-cold dark matter models*, JCAP **0905** (2009) 012, [arXiv:0812.0010]

[49] R. Barkana, Z. Haiman and J. P. Ostriker, *Constraints on warm dark matter from cosmological reionization*, [astro-ph/0102304]

[50] N. Yoshida, A. Sokasian, L. Hernquist and V. Springel, *Early structure formation and reionization in a warm dark matter cosmology*, Astrophys.J. **591** (2003) L1–L4, [astro-ph/0303622]

[51] L. Gao and T. Theuns, *Lighting the Universe with filaments*, Science **317** (2007) 1527, [arXiv:0709.2165]

[52] B. Yue and X. Chen, *Reionization in the Warm Dark Matter Model*, Astrophys.J. **747** (2012) 127, [arXiv:1201.3686]

[53] M. Kawasaki, N. Sugiyama and T. Yanagida, *Gravitino warm dark matter motivated by the CDF e e gamma gamma event*, Mod.Phys.Lett. **A12** (1997) 1275–1282, [hep-ph/9607273]

[54] A. Kusenko, *Sterile neutrinos: The Dark side of the light fermions*, Phys.Rept. **481** (2009) 1–28, [arXiv:0906.2968]

[55] J. A. Cembranos, J. L. Feng, A. Rajaraman and F. Takayama, *SuperWIMP solutions to small scale structure problems*, Phys.Rev.Lett. **95** (2005) 181301, [hep-ph/0507150]

[56] Particle Data Group Collaboration, J. Beringer *et al.*, *Review of Particle Physics (RPP)*, Phys.Rev. **D86** (2012) 010001

[57] W. Buchmuller, L. Covi, J. Kersten and K. Schmidt-Hoberg, *Dark Matter from Gaugino Mediation*, JCAP **0611** (2006) 007, [hep-ph/0609142]

[58] M. Pospelov, *Particle physics catalysis of thermal Big Bang Nucleosynthesis*, Phys.Rev.Lett. **98** (2007) 231301, [hep-ph/0605215]

[59] K. Kohri and F. Takayama, *Big bang nucleosynthesis with long lived charged massive particles*, Phys.Rev. **D76** (2007) 063507, [hep-ph/0605243]

[60] M. Kaplinghat and A. Rajaraman, *Big Bang Nucleosynthesis with Bound States of Long-lived Charged Particles*, Phys.Rev. **D74** (2006) 103004, [astro-ph/0606209]

[61] R. H. Cyburt, J. R. Ellis, B. D. Fields, K. A. Olive and V. C. Spanos, *Bound-State Effects on Light-Element Abundances in Gravitino Dark Matter Scenarios*, JCAP **0611** (2006) 014, [astro-ph/0608562]

[62] F. D. Steffen, *Constraints on Gravitino Dark Matter Scenarios with Long-Lived Charged Sleptons*, AIP Conf.Proc. **903** (2007) 595–598, [hep-ph/0611027]

[63] K. Hamaguchi, T. Hatsuda, M. Kamimura, Y. Kino and T. Yanagida, *Stau-catalyzed ^{6}Li Production in Big-Bang Nucleosynthesis*, Phys.Lett. **B650** (2007) 268–274, [hep-ph/0702274]

[64] M. Kawasaki, K. Kohri and T. Moroi, *Big-Bang Nucleosynthesis with Long-Lived Charged Slepton*, Phys.Lett. **B649** (2007) 436–439, [hep-ph/0703122]

[65] K. Jedamzik, *The cosmic Li-6 and Li-7 problems and BBN with long-lived charged massive particles*, Phys.Rev. **D77** (2008) 063524, [arXiv:0707.2070]

[66] K. Jedamzik, *Bounds on long-lived charged massive particles from Big Bang nucleosynthesis*, JCAP **0803** (2008) 008, [arXiv:0710.5153]

[67] T. Jittoh, K. Kohri, M. Koike, J. Sato, K. Sugai *et al.*, *Big-bang nucleosynthesis with a long-lived charged massive particle including ^{4}He spallation processes*, Phys.Rev. **D84** (2011) 035008, [arXiv:1105.1431]

[68] K. Sigurdson and M. Kamionkowski, *Charged - particle decay and suppression of small - scale power*, Phys.Rev.Lett. **92** (2004) 171302, [astro-ph/0311486]

[69] K. Kohri and T. Takahashi, *Cosmology with Long-Lived Charged Massive Particles*, Phys.Lett. **B682** (2010) 337–341, [arXiv:0909.4610]

[70] M. Dine, A. E. Nelson, Y. Nir and Y. Shirman, *New tools for low-energy dynamical supersymmetry breaking*, Phys.Rev. **D53** (1996) 2658–2669, [hep-ph/9507378]

[71] K. A. Olive and M. S. Turner, *Cosmological Bounds on the Masses of Stable, Right-handed Neutrinos*, Phys.Rev. **D25** (1982) 213

[72] S. Dodelson and L. M. Widrow, *Sterile-neutrinos as dark matter*, Phys.Rev.Lett. **72** (1994) 17–20, [hep-ph/9303287]

[73] J. M. Cline, *Constraints on almost Dirac neutrinos from neutrino - anti-neutrino oscillations*, Phys.Rev.Lett. **68** (1992) 3137–3140

[74] M. Shaposhnikov and I. Tkachev, *The nuMSM, inflation, and dark matter*, Phys.Lett. **B639** (2006) 414–417, [hep-ph/0604236]

[75] K. Petraki and A. Kusenko, *Dark-matter sterile neutrinos in models with a gauge singlet in the Higgs sector*, Phys.Rev. **D77** (2008) 065014, [arXiv:0711.4646]

[76] D. Boyanovsky, *Clustering properties of a sterile neutrino dark matter candidate*, Phys.Rev. **D78** (2008) 103505, [arXiv:0807.0646]

[77] P. Gondolo and G. Gelmini, *Cosmic abundances of stable particles: Improved analysis*, Nucl.Phys. **B360** (1991) 145–179

[78] K. Griest and D. Seckel, *Three exceptions in the calculation of relic abundances*, Phys.Rev. **D43** (1991) 3191–3203

[79] W. Lin, D. Huang, X. Zhang and R. H. Brandenberger, *Nonthermal production of WIMPs and the subgalactic structure of the universe*, Phys.Rev.Lett. **86** (2001) 954, [astro-ph/0009003]

[80] J. Hisano, K. Kohri and M. M. Nojiri, *Neutralino warm dark matter*, Phys.Lett. **B505** (2001) 169–176, [hep-ph/0011216]

[81] M. Kawasaki, F. Takahashi and T. Yanagida, *Gravitino overproduction in inflaton decay*, Phys.Lett. **B638** (2006) 8–12, [hep-ph/0603265]

[82] M. Endo, K. Hamaguchi and F. Takahashi, *Moduli-induced gravitino problem*, Phys.Rev.Lett. **96** (2006) 211301, [hep-ph/0602061]

[83] F. Takahashi, *Gravitino dark matter from inflaton decay*, Phys.Lett. **B660** (2008) 100–106, [arXiv:0705.0579]

[84] M. Kaplinghat, *Dark matter from early decays*, Phys.Rev. **D72** (2005) 063510, [astro-ph/0507300]

[85] L. E. Strigari, M. Kaplinghat and J. S. Bullock, *Dark Matter Halos with Cores from Hierarchical Structure Formation*, Phys.Rev. **D75** (2007) 061303, [astro-ph/0606281]

[86] S. Aoyama, K. Ichiki, D. Nitta and N. Sugiyama, *Formulation and constraints on decaying dark matter with finite mass daughter particles*, JCAP **1109** (2011) 025, [arXiv:1106.1984]

[87] M. Ibe, R. Sato, T. T. Yanagida and K. Yonekura, *Gravitino Dark Matter and Light Gluino in an R-invariant Low Scale Gauge Mediation*, JHEP **1104** (2011) 077, [arXiv:1012.5466]

[88] M. Ibe and R. Sato, *A 125 GeV Higgs Boson Mass and Gravitino Dark Matter in R-invariant Direct Gauge Mediation*, Phys.Lett. **B717** (2012) 197–201, [arXiv:1204.3499]

[89] A. Lewis, A. Challinor and A. Lasenby, *Efficient Computation of CMB anisotropies in closed FRW models*, Astrophys. J. **538** (2000) 473–476, [astro-ph/9911177]

[90] A. Lewis and A. Challinor, *Evolution of cosmological dark matter perturbations*, Phys.Rev. **D66** (2002) 023531, [astro-ph/0203507]

[91] J. Hisano, K. T. Inoue and T. Takahashi, *Constraining SuperWIMPy and Warm Subhalos with Future Submillilensing*, Phys.Lett. **B643** (2006) 141–146, [hep-ph/0608126]

[92] M. Kamimura, Y. Kino and E. Hiyama, *Big-Bang Nucleosynthesis Reactions Catalyzed by a Long-Lived Negatively-Charged Leptonic Particle*, Prog.Theor.Phys. **121** (2009) 1059–1098, [arXiv:0809.4772]

[93] M. Kawasaki, K. Kohri and T. Moroi, *Radiative decay of a massive particle and the nonthermal process in primordial nucleosynthesis*, Phys.Rev. **D63** (2001) 103502, [hep-ph/0012279]

[94] W. Hu and J. Silk, *Thermalization constraints and spectral distortions for massive unstable relic particles*, Phys.Rev.Lett. **70** (1993) 2661–2664

[95] V. Springel, *The Cosmological simulation code GADGET-2*, Mon.Not.Roy.Astron.Soc. **364** (2005) 1105–1134, [astro-ph/0505010]

[96] M. Davis, G. Efstathiou, C. S. Frenk and S. D. White, *The Evolution of Large Scale Structure in a Universe Dominated by Cold Dark Matter*, Astrophys.J. **292** (1985) 371–394

[97] V. Springel, S. D. White, G. Tormen and G. Kauffmann, *Populating a cluster of galaxies. 1. Results at $z = 0$*, Mon.Not.Roy.Astron.Soc. **328** (2001) 726, [astro-ph/0012055]

[98] P. Colin, O. Valenzuela and V. Avila-Reese, *On the Structure of Dark Matter Halos at the Damping Scale of the Power Spectrum with and without Relict Velocities*, Astrophys.J. **673** (2008) 203–214, [arXiv:0709.4027]

[99] J. Wang and S. D. White, *Discreteness effects in simulations of Hot/Warm dark matter*, Mon.Not.Roy.Astron.Soc. **380** (2007) 93–103, [astro-ph/0702575]

[100] E. Polisensky and M. Ricotti, *Constraints on the Dark Matter Particle Mass from the Number of Milky Way Satellites*, Phys.Rev. **D83** (2011) 043506, [arXiv:1004.1459]

[101] SDSS Collaboration Collaboration, X. Xue *et al.*, *The Milky Way's Circular Velocity Curve to 60 kpc and an Estimate of the Dark Matter Halo Mass from Kinematics of 2400 SDSS Blue Horizontal Branch Stars*, Astrophys.J. **684** (2008) 1143–1158, [arXiv:0801.1232]

[102] T. Ishiyama, T. Fukushige and J. Makino, *Variation of the subhalo abundance in dark matter halos*, Astrophys.J. **696** (2009) 2115–2125, [arXiv:0812.0683]

[103] A. M. Brooks, M. Kuhlen, A. Zolotov and D. Hooper, *A Baryonic Solution to the Missing Satellites Problem*, Astrophys.J. **765** (2013) 22, [arXiv:1209.5394]

[104] T. Gherghetta, G. F. Giudice and J. D. Wells, *Phenomenological consequences of supersymmetry with anomaly induced masses*, Nucl.Phys. **B559** (1999) 27–47, [hep-ph/9904378]

[105] T. Moroi and L. Randall, *Wino cold dark matter from anomaly mediated SUSY breaking*, Nucl.Phys. **B570** (2000) 455–472, [hep-ph/9906527]

[106] M. Ibe, R. Kitano, H. Murayama and T. Yanagida, *Viable supersymmetry and leptogenesis with anomaly mediation*, Phys.Rev. **D70** (2004) 075012, [hep-ph/0403198]

[107] M. Ibe, R. Kitano and H. Murayama, *A Viable supersymmetric model with UV insensitive anomaly mediation*, Phys.Rev. **D71** (2005) 075003, [hep-ph/0412200]

[108] S. Furlanetto, S. P. Oh and F. Briggs, *Cosmology at Low Frequencies: The 21 cm Transition and the High-Redshift Universe*, Phys.Rept. **433** (2006) 181–301, [astro-ph/0608032]

[109] J. R. Pritchard and A. Loeb, *21-cm cosmology*, Rept.Prog.Phys. **75** (2012) 086901, [arXiv:1109.6012]

[110] ATLAS Collaboration Collaboration, G. Aad *et al.*, *Observation of a new particle in the search for the Standard Model Higgs boson with the ATLAS detector at the LHC*, Phys.Lett. **B716** (2012) 1–29, [arXiv:1207.7214]

[111] CMS Collaboration Collaboration, S. Chatrchyan *et al.*, *Observation of a new boson at a mass of 125 GeV with the CMS experiment at the LHC*, Phys.Lett. **B716** (2012) 30–61, [arXiv:1207.7235]

[112] Y. Okada, M. Yamaguchi and T. Yanagida, *Upper bound of the lightest Higgs boson mass in the minimal supersymmetric standard model*, Prog.Theor.Phys. **85** (1991) 1–6

[113] Y. Okada, M. Yamaguchi and T. Yanagida, *Renormalization group analysis on the Higgs mass in the softly broken supersymmetric standard model*, Phys.Lett. **B262** (1991) 54–58

[114] J. R. Ellis, G. Ridolfi and F. Zwirner, *On radiative corrections to supersymmetric Higgs boson masses and their implications for LEP searches*, Phys.Lett. **B262** (1991) 477–484

[115] H. E. Haber and R. Hempfling, *Can the mass of the lightest Higgs boson of the minimal supersymmetric model be larger than m(Z)?*, Phys.Rev.Lett. **66** (1991) 1815–1818

[116] J. R. Espinosa and R.-J. Zhang, *MSSM lightest CP even Higgs boson mass to O(alpha(s) alpha(t)): The Effective potential approach*, JHEP **0003** (2000) 026, [hep-ph/9912236]

[117] A. H. Chamseddine, R. L. Arnowitt and P. Nath, *Locally Supersymmetric Grand Unification*, Phys.Rev.Lett. **49** (1982) 970

[118] R. Barbieri, S. Ferrara and C. A. Savoy, *Gauge Models with Spontaneously Broken Local Supersymmetry*, Phys.Lett. **B119** (1982) 343

[119] L. E. Ibanez, *Locally Supersymmetric SU(5) Grand Unification*, Phys.Lett. **B118** (1982) 73

[120] L. J. Hall, J. D. Lykken and S. Weinberg, *Supergravity as the Messenger of Supersymmetry Breaking*, Phys.Rev. **D27** (1983) 2359–2378

[121] N. Ohta, *GRAND UNIFIED THEORIES BASED ON LOCAL SUPERSYMMETRY*, Prog.Theor.Phys. **70** (1983) 542

[122] G. Coughlan, W. Fischler, E. W. Kolb, S. Raby and G. G. Ross, *Cosmological Problems for the Polonyi Potential*, Phys.Lett. **B131** (1983) 59

[123] M. Ibe, Y. Shinbara and T. Yanagida, *The Polonyi Problem and Upper bound on Inflation Scale in Supergravity*, Phys.Lett. **B639** (2006) 534–540, [hep-ph/0605252]

[124] M. Ibe, T. Moroi and T. Yanagida, *Possible Signals of Wino LSP at the Large Hadron Collider*, Phys.Lett. **B644** (2007) 355–360, [hep-ph/0610277]

[125] M. Ibe and T. T. Yanagida, *The Lightest Higgs Boson Mass in Pure Gravity Mediation Model*, Phys.Lett. **B709** (2012) 374–380, [arXiv:1112.2462]

[126] M. Ibe, S. Matsumoto and T. T. Yanagida, *Pure Gravity Mediation with* $m_{3/2} = 10 - 100\,TeV$, Phys.Rev. **D85** (2012) 095011, [arXiv:1202.2253]

[127] J. D. Wells, *PeV-scale supersymmetry*, Phys.Rev. **D71** (2005) 015013, [hep-ph/0411041]

[128] B. S. Acharya, K. Bobkov, G. L. Kane, P. Kumar and J. Shao, *Explaining the Electroweak Scale and Stabilizing Moduli in M Theory*, Phys.Rev. **D76** (2007) 126010, [hep-th/0701034]

[129] L. J. Hall and Y. Nomura, *Spread Supersymmetry*, JHEP **1201** (2012) 082, [arXiv:1111.4519]

[130] E. Dudas, A. Linde, Y. Mambrini, A. Mustafayev and K. A. Olive, *Strong moduli stabilization and phenomenology*, Eur.Phys.J. **C73** (2013) 2268, [arXiv:1209.0499]

[131] N. Arkani-Hamed and S. Dimopoulos, *Supersymmetric unification without low energy supersymmetry and signatures for fine-tuning at the LHC*, JHEP **0506** (2005) 073, [hep-th/0405159]

[132] G. Giudice and A. Romanino, *Split supersymmetry*, Nucl.Phys. **B699** (2004) 65–89, [hep-ph/0406088]

[133] N. Arkani-Hamed, S. Dimopoulos, G. Giudice and A. Romanino, *Aspects of split supersymmetry*, Nucl.Phys. **B709** (2005) 3–46, [hep-ph/0409232]

[134] M. Bose and M. Dine, *Gravity Mediation Retrofitted*, JHEP **1303** (2013) 057, [arXiv:1209.2488]

[135] K. Inoue, M. Kawasaki, M. Yamaguchi and T. Yanagida, *Vanishing squark and slepton masses in a class of supergravity models*, Phys.Rev. **D45** (1992) 328–337

[136] G. F. Giudice, M. A. Luty, H. Murayama and R. Rattazzi, *Gaugino mass without singlets*, JHEP **9812** (1998) 027, [hep-ph/9810442]

[137] L. Randall and R. Sundrum, *Out of this world supersymmetry breaking*, Nucl.Phys. **B557** (1999) 79–118, [hep-th/9810155]

[138] M. Dine and D. MacIntire, *Supersymmetry, naturalness, and dynamical supersymmetry breaking*, Phys.Rev. **D46** (1992) 2594–2601, [hep-ph/9205227]

[139] J. L. Feng, T. Moroi, L. Randall, M. Strassler and S.-f. Su, *Discovering supersymmetry at the Tevatron in wino LSP scenarios*, Phys.Rev.Lett. **83** (1999) 1731–1734, [hep-ph/9904250]

[140] J. Hisano, S. Matsumoto, M. Nagai, O. Saito and M. Senami, *Non-perturbative effect on thermal relic abundance of dark matter*, Phys.Lett. **B646** (2007) 34–38, [hep-ph/0610249]

[141] M. Bolz, A. Brandenburg and W. Buchmuller, *Thermal production of gravitinos*, Nucl.Phys. **B606** (2001) 518–544, [hep-ph/0012052]

[142] M. Kawasaki, K. Kohri and T. Moroi, *Big-Bang nucleosynthesis and hadronic decay of long-lived massive particles*, Phys.Rev. **D71** (2005) 083502, [astro-ph/0408426]

[143] K. Jedamzik, *Big bang nucleosynthesis constraints on hadronically and electromagnetically decaying relic neutral particles*, Phys.Rev. **D74** (2006) 103509, [hep-ph/0604251]

[144] M. Kawasaki, K. Kohri, T. Moroi and A. Yotsuyanagi, *Big-Bang Nucleosynthesis and Gravitino*, Phys.Rev. **D78** (2008) 065011, [arXiv:0804.3745]

[145] M. Fukugita and T. Yanagida, *Baryogenesis Without Grand Unification*, Phys.Lett. **B174** (1986) 45

[146] W. Buchmuller, R. Peccei and T. Yanagida, *Leptogenesis as the origin of matter*, Ann.Rev.Nucl.Part.Sci. **55** (2005) 311–355, [hep-ph/0502169]

[147] S. Davidson, E. Nardi and Y. Nir, *Leptogenesis*, Phys.Rept. **466** (2008) 105–177, [arXiv:0802.2962]

[148] ATLAS Collaboration Collaboration, *Search for squarks and gluinos with the ATLAS detector using final states with jets and missing transverse momentum and 5.8 fb^{-1} of $\sqrt{s}$=8 TeV proton-proton collision data*, Tech. Rep. ATLAS-CONF-2012-109, CERN, Geneva, Aug, 2012.

[149] B. Bhattacherjee, B. Feldstein, M. Ibe, S. Matsumoto and T. T. Yanagida, *Pure Gravity Mediation of Supersymmetry Breaking at the LHC*, Phys.Rev. **D87** (2013) 015028, [arXiv:1207.5453]

[150] M. Toharia and J. D. Wells, *Gluino decays with heavier scalar superpartners*, JHEP **0602** (2006) 015, [hep-ph/0503175]

[151] P. Gambino, G. Giudice and P. Slavich, *Gluino decays in split supersymmetry*, Nucl.Phys. **B726** (2005) 35–52, [hep-ph/0506214]

[152] A. Arvanitaki, S. Dimopoulos, A. Pierce, S. Rajendran and J. G. Wacker, *Stopping gluinos*, Phys.Rev. **D76** (2007) 055007, [hep-ph/0506242]

[153] Fermi-LAT collaboration Collaboration, M. Ackermann *et al.*, *Constraining Dark Matter Models from a Combined Analysis of Milky Way Satellites with the Fermi Large Area Telescope*, Phys.Rev.Lett. **107** (2011) 241302, [arXiv:1108.3546]

[154] D. Hooper, C. Kelso and F. S. Queiroz, *Stringent and Robust Constraints on the Dark Matter Annihilation Cross Section From the Region of the Galactic Center*, Astropart.Phys. **46** (2013) 55–70, [arXiv:1209.3015]

[155] C. Evoli, I. Cholis, D. Grasso, L. Maccione and P. Ullio, *Antiprotons from dark matter annihilation in the Galaxy: astrophysical uncertainties*, Phys.Rev. **D85** (2012) 123511, [arXiv:1108.0664]

[156] T. Moroi and K. Nakayama, *Wino LSP detection in the light of recent Higgs searches at the LHC*, Phys.Lett. **B710** (2012) 159–163, [arXiv:1112.3123]

[157] ATLAS Collaboration Collaboration, *Search for direct chargino production in anomaly-mediated supersymmetry breaking models based on a disappearing-track signature, in pp collisions at sqrt(s) = 7 TeV with the ATLAS detector at the LHC*, Tech. Rep. ATLAS-CONF-2012-111, CERN, Geneva, Aug, 2012.

[158] G. Arcadi and P. Ullio, *Accurate estimate of the relic density and the kinetic decoupling in non-thermal dark matter models*, Phys.Rev. **D84** (2011) 043520, [arXiv:1104.3591]

[159] M. Reno and D. Seckel, *Primordial Nucleosynthesis: The Effects of Injecting Hadrons*, Phys.Rev. **D37** (1988) 3441

[160] D. Anderhalden, J. Diemand, G. Bertone, A. V. Maccio and A. Schneider, *The Galactic Halo in Mixed Dark Matter Cosmologies*, JCAP **1210** (2012) 047, [arXiv:1206.3788]

[161] J. Lesgourgues and S. Pastor, *Massive neutrinos and cosmology*, Phys.Rept. **429** (2006) 307–379, [astro-ph/0603494]

[162] J. R. Pritchard and E. Pierpaoli, *Constraining massive neutrinos using cosmological 21 cm observations*, Phys.Rev. **D78** (2008) 065009, [arXiv:0805.1920]

[163] Y. Oyama, A. Shimizu and K. Kohri, *Determination of neutrino mass hierarchy by 21 cm line and CMB B-mode polarization observations*, Phys.Lett. **B718** (2013) 1186–1193, [arXiv:1205.5223]

[164] A. Loeb and M. Zaldarriaga, *Measuring the small - scale power spectrum of cosmic density fluctuations through 21 cm tomography prior to the epoch of structure formation*, Phys.Rev.Lett. **92** (2004) 211301, [astro-ph/0312134]

[165] G. Kane, J. Shao, S. Watson and H.-B. Yu, *The Baryon-Dark Matter Ratio Via Moduli Decay After Affleck-Dine Baryogenesis*, JCAP **1111** (2011) 012, [arXiv:1108.5178]

[166] M. Drees, M. M. Nojiri, D. Roy and Y. Yamada, *Light Higgsino dark matter*, Phys.Rev. **D56** (1997) 276–290, [hep-ph/9701219]

[167] M. Fujii and K. Hamaguchi, *Nonthermal dark matter via Affleck-Dine baryogenesis and its detection possibility*, Phys.Rev. **D66** (2002) 083501, [hep-ph/0205044]

[168] M. Ibe, S. Matsumoto and R. Sato, *Mass Splitting between Charged and Neutral Winos at Two-Loop Level*, Phys.Lett. **B721** (2013) 252–260, [arXiv:1212.5989]

[169] T. Cohen, M. Lisanti, A. Pierce and T. R. Slatyer, *Wino Dark Matter Under Siege*, JCAP **1310** (2013) 061, [arXiv:1307.4082]

[170] J. Fan and M. Reece, *In Wino Veritas? Indirect Searches Shed Light on Neutralino Dark Matter*, JHEP **1310** (2013) 124, [arXiv:1307.4400]

[171] N. Arkani-Hamed, A. Gupta, D. E. Kaplan, N. Weiner and T. Zorawski, *Simply Unnatural Supersymmetry*, [arXiv:1212.6971]

[172] H. Baer, A. Mustafayev, E.-K. Park and S. Profumo, *Mixed wino dark matter: Consequences for direct, indirect and collider detection*, JHEP **0507** (2005) 046, [hep-ph/0505227]

[173] H. Baer, T. Krupovnickas, A. Mustafayev, E.-K. Park, S. Profumo *et al.*, *Exploring the BWCA (bino-wino co-annihilation) scenario for neutralino dark matter*, JHEP **0512** (2005) 011, [hep-ph/0511034]

[174] A. Birkedal-Hansen and B. D. Nelson, *The Role of Wino content in neutralino dark matter*, Phys.Rev. **D64** (2001) 015008, [hep-ph/0102075]

[175] ATLAS Collaboration Collaboration, G. Aad *et al.*, *Search for new phenomena in final states with large jet multiplicities and missing transverse momentum at $\sqrt{s} = 8$ TeV proton-proton collisions using the ATLAS experiment*, JHEP **1310** (2013) 130, [arXiv:1308.1841]

[176] T. Cohen, T. Golling, M. Hance, A. Henrichs, K. Howe *et al.*, *A Comparison of Future Proton Colliders Using SUSY Simplified Models: A Snowmass Whitepaper*, [arXiv:1310.0077]

[177] J. Hisano, S. Matsumoto, M. M. Nojiri and O. Saito, *Non-perturbative effect on dark matter annihilation and gamma ray signature from galactic center*, Phys.Rev. **D71** (2005) 063528, [hep-ph/0412403]

[178] M. Srednicki, R. Watkins and K. A. Olive, *Calculations of Relic Densities in the Early Universe*, Nucl.Phys. **B310** (1988) 693

[179] C. Chen, M. Drees and J. Gunion, *A Nonstandard string / SUSY scenario and its phenomenological implications*, Phys.Rev. **D55** (1997) 330–347, [hep-ph/9607421]

[180] S. P. Martin, *A Supersymmetry primer*, [hep-ph/9709356]

[181] W. Buchmuller, V. Domcke and K. Schmitz, *Spontaneous B-L Breaking as the Origin of the Hot Early Universe*, Nucl.Phys. **B862** (2012) 587–632, [arXiv:1202.6679]

[182] W. Buchmuller, V. Domcke and K. Schmitz, *WIMP Dark Matter from Gravitino Decays and Leptogenesis*, Phys.Lett. **B713** (2012) 63–67, [arXiv:1203.0285]

[183] B. Moore, T. R. Quinn, F. Governato, J. Stadel and G. Lake, *Cold collapse and the core catastrophe*, Mon.Not.Roy.Astron.Soc. **310** (1999) 1147–1152, [astro-ph/9903164]

[184] K. Harigaya, M. Ibe and T. T. Yanagida, *A Closer Look at Gaugino Masses in Pure Gravity Mediation Model/Minimal Split SUSY Model*, JHEP **1312** (2013) 016, [arXiv:1310.0643]

[185] K. Ichikawa, M. Kawasaki, K. Nakayama, T. Sekiguchi and T. Takahashi, *Constraining Light Gravitino Mass from Cosmic Microwave Background*, JCAP **0908** (2009) 013, [arXiv:0905.2237]

[186] D. J. Bacon, R. J. Massey, A. R. Refregier and R. S. Ellis, *Joint cosmic shear measurements with the Keck and William Herschel Telescopes*, Mon.Not.Roy.Astron.Soc. **344** (2003) 673, [astro-ph/0203134]

[187] T. Hamana, S. Miyazaki, K. Shimasaku, H. Furusawa, M. Doi *et al.*, *Cosmic shear statistics in the Suprime-Cam 2.1 sq deg field: Constraints on Omega(m) and Sigma(8)*, Astrophys.J. **597** (2003) 98–110, [astro-ph/0210450]

[188] J. Benjamin, C. Heymans, E. Semboloni, L. Van Waerbeke, H. Hoekstra *et al.*, *Cosmological Constraints From the 100 Square Degree Weak Lensing Survey*, Mon.Not.Roy.Astron.Soc. **381** (2007) 702–712, [astro-ph/0703570]

[189] M. Kilbinger, L. Fu, C. Heymans, F. Simpson, J. Benjamin *et al.*, *CFHTLenS: Combined probe cosmological model comparison using 2D weak gravitational lensing*, Monthly Notices of the Royal Astronomical Society **430** (2013), no. 3, 2200–2220, [arXiv:1212.3338]

[190] M. Dine and W. Fischler, *A Phenomenological Model of Particle Physics Based on Supersymmetry*, Phys.Lett. **B110** (1982) 227

[191] C. R. Nappi and B. A. Ovrut, *Supersymmetric Extension of the SU(3) x SU(2) x U(1) Model*, Phys.Lett. **B113** (1982) 175

[192] L. Alvarez-Gaume, M. Claudson and M. B. Wise, *Low-Energy Supersymmetry*, Nucl.Phys. **B207** (1982) 96

[193] M. Dine and A. E. Nelson, *Dynamical supersymmetry breaking at low-energies*, Phys.Rev. **D48** (1993) 1277–1287, [hep-ph/9303230]

[194] M. Dine, A. E. Nelson and Y. Shirman, *Low-energy dynamical supersymmetry breaking simplified*, Phys.Rev. **D51** (1995) 1362–1370, [hep-ph/9408384]

[195] B. Allanach, *SOFTSUSY: a program for calculating supersymmetric spectra*, Comput.Phys.Commun. **143** (2002) 305–331, [hep-ph/0104145]

[196] H. Baer, P. G. Mercadante, F. Paige, X. Tata and Y. Wang, *LHC reach for gauge mediated supersymmetry breaking models via prompt photon channels*, Phys.Lett. **B435** (1998) 109–117, [hep-ph/9806290]

[197] H. Baer, P. G. Mercadante, X. Tata and Y.-l. Wang, *The Reach of the CERN large hadron collider for gauge mediated supersymmetry breaking models*, Phys.Rev. **D62** (2000) 095007, [hep-ph/0004001]

[198] ATLAS Collaboration Collaboration, G. Aad *et al.*, *Expected Performance of the ATLAS Experiment - Detector, Trigger and Physics*, [arXiv:0901.0512]

[199] ATLAS collaboration Collaboration, D. Ludwig, *Expected Performance of the ATLAS Detector in GMSB Models with Tau Final States*, PoS **HCP2009** (2009) 073, [arXiv:1002.0944]

[200] E. Nakamura and S. Shirai, *Discovery Potential for Low-Scale Gauge Mediation at Early LHC*, JHEP **1103** (2011) 115, [arXiv:1010.5995]

[201] ATLAS Collaboration Collaboration, G. Aad *et al.*, *Search for events with large missing transverse momentum, jets, and at least two tau leptons in 7 TeV proton-proton collision data with the ATLAS detector*, Phys.Lett. **B714** (2012) 180–196, [arXiv:1203.6580]

[202] ATLAS Collaboration Collaboration, G. Aad *et al.*, *Search for supersymmetry with jets, missing transverse momentum and at least one hadronically decaying τ lepton in proton-proton collisions at $\sqrt{s} = 7$ TeV with the ATLAS detector*, Phys.Lett. **B714** (2012) 197–214, [arXiv:1204.3852]

[203] ATLAS Collaboration Collaboration, G. Aad *et al.*, *Search for Supersymmetry in Events with Large Missing Transverse Momentum, Jets, and at Least One Tau Lepton in 7 TeV Proton-Proton Collision Data with the ATLAS Detector*, Eur.Phys.J. **C72** (2012) 2215, [arXiv:1210.1314]

[204] ATLAS Collaboration Collaboration, *Search for Supersymmetry in Events with Large Missing Transverse Momentum, Jets, and at Least One Tau Lepton in 21 fb^{-1} of $\sqrt{s} = 8$ TeV Proton-Proton Collision Data with the ATLAS Detector*, Tech. Rep. ATLAS-CONF-2013-026, CERN, Geneva, Mar, 2013.

[205] J. Hisano, M. Nagai, M. Senami and S. Sugiyama, *Stability of Metastable Vacua in Gauge Mediated SUSY Breaking Models with Ultra Light Gravitino*, Phys.Lett. **B659** (2008) 361–366, [arXiv:0708.3340]

[206] J. Hisano, M. Nagai, S. Sugiyama and T. Yanagida, *Upperbound on Squark Masses in Gauge-Mediation Model with Light Gravitino*, Phys.Lett. **B665** (2008) 237–241, [arXiv:0804.2957]

[207] T. Moroi, H. Murayama and M. Yamaguchi, *Cosmological constraints on the light stable gravitino*, Phys.Lett. **B303** (1993) 289–294

[208] E. Pierpaoli, S. Borgani, A. Masiero and M. Yamaguchi, *The Formation of cosmic structures in a light gravitino dominated universe*, Phys.Rev. **D57** (1998) 2089–2100, [astro-ph/9709047]

[209] J. Preskill, M. B. Wise and F. Wilczek, *Cosmology of the Invisible Axion*, Phys.Lett. **B120** (1983) 127–132

[210] L. Abbott and P. Sikivie, *A Cosmological Bound on the Invisible Axion*, Phys.Lett. **B120** (1983) 133–136

[211] M. Dine and W. Fischler, *The Not So Harmless Axion*, Phys.Lett. **B120** (1983) 137–141

[212] S. Dimopoulos, G. Giudice and A. Pomarol, *Dark matter in theories of gauge mediated supersymmetry breaking*, Phys.Lett. **B389** (1996) 37–42, [hep-ph/9607225]

[213] J. Fan, J. Thaler and L.-T. Wang, *Dark matter from dynamical SUSY breaking*, JHEP **1006** (2010) 045, [arXiv:1004.0008]

[214] T. T. Yanagida and K. Yonekura, *A Conformal Gauge Mediation and Dark Matter with Only One Parameter*, Phys.Lett. **B693** (2010) 281–286, [arXiv:1006.2271]

[215] T. T. Yanagida, N. Yokozaki and K. Yonekura, *Higgs Boson Mass in Low Scale Gauge Mediation Models*, JHEP **1210** (2012) 017, [arXiv:1206.6589]

[216] M. Bartelmann and P. Schneider, *Weak gravitational lensing*, Phys.Rept. **340** (2001) 291–472, [astro-ph/9912508]

[217] D. Munshi, P. Valageas, L. Van Waerbeke and A. Heavens, *Cosmology with Weak Lensing Surveys*, Phys.Rept. **462** (2008) 67–121, [astro-ph/0612667]

[218] D. N. Limber, *The Analysis of Counts of the Extragalactic Nebulae in Terms of a Fluctuating Density Field. II*, Astrophys.J. **119** (1954) 655

[219] N. Kaiser, *Weak gravitational lensing of distant galaxies*, Astrophys.J. **388** (1992) 272

[220] B. Jain, U. Seljak and S. D. White, *Ray tracing simulations of weak lensing by large scale structure*, Astrophys.J. **530** (2000) 547, [astro-ph/9901191]

[221] S. Hilbert, J. Hartlap, S. White and P. Schneider, *Ray-tracing through the Millennium Simulation: Born corrections and lens-lens coupling in cosmic shear and galaxy-galaxy lensing*, [arXiv:0809.5035]

[222] M. Sato, T. Hamana, R. Takahashi, M. Takada, N. Yoshida *et al.*, *Simulations of Wide-Field Weak Lensing Surveys I: Basic Statistics and Non-Gaussian Effects*, Astrophys.J. **701** (2009) 945–954, [arXiv:0906.2237]

[223] J. Peacock and S. Dodds, *Nonlinear evolution of cosmological power spectra*, Mon.Not.Roy.Astron.Soc. **280** (1996) L19, [astro-ph/9603031]

[224] Virgo Consortium Collaboration, R. Smith *et al.*, *Stable clustering, the halo model and nonlinear cosmological power spectra*, Mon.Not.Roy.Astron.Soc. **341** (2003) 1311, [astro-ph/0207664]

[225] K. Heitmann, M. White, C. Wagner, S. Habib and D. Higdon, *The Coyote Universe I: Precision Determination of the Nonlinear Matter Power Spectrum*, Astrophys.J. **715** (2010) 104–121, [arXiv:0812.1052]

[226] M. J. White and W. Hu, *A New algorithm for computing statistics of weak lensing by large scale structure*, Astrophys.J. **537** (2000) 1–11, [astro-ph/9909165]

[227] T. Hamana and Y. Mellier, *Numerical study of statistical properties of the lensing excursion angles*, Mon.Not.Roy.Astron.Soc. **327** (2001) 169, [astro-ph/0101333]

[228] V. Avila-Reese, P. Colin, O. Valenzuela, E. D'Onghia and C. Firmani, *Formation and structure of halos in a warm dark matter cosmology*, Astrophys.J. **559** (2001) 516–530, [astro-ph/0010525]

[229] T. Eifler, P. Schneider and J. Hartlap, *Dependence of cosmic shear covariances on cosmology - Impact on parameter estimation*, [arXiv:0810.4254]

[230] A. Cooray and W. Hu, *Power spectrum covariance of weak gravitational lensing*, Astrophys.J. **554** (2001) 56–66, [astro-ph/0012087]

[231] M. Sato and T. Nishimichi, *Impact of the non-Gaussian covariance of the weak lensing power spectrum and bispectrum on cosmological parameter estimation*, [arXiv:1301.3588]

[232] M. Takada and . White, Martin J., *Tomography of lensing cross power spectra*, Astrophys.J. **601** (2004) L1, [astro-ph/0311104]

[233] S. Miyazaki, T. Hamana, K. Shimasaku, H. Furusawa, M. Doi *et al.*, *Searching for dark matter halos in the Suprime-CAM 2 Sq Deg Field*, Astrophys.J. **580** (2002) L97–L100, [astro-ph/0210441]

[234] R. Mandelbaum, U. Seljak, G. Kauffmann, C. M. Hirata and J. Brinkmann, *Galaxy halo masses and satellite fractions from galaxy-galaxy lensing in the sdss: stellar mass, luminosity, morphology, and environment dependencies*, Mon.Not.Roy.Astron.Soc. **368** (2006) 715, [astro-ph/0511164]

[235] A. Lewis and S. Bridle, *Cosmological parameters from CMB and other data: A Monte Carlo approach*, Phys.Rev. **D66** (2002) 103511, [astro-ph/0205436]

[236] J. Bond, G. Efstathiou and J. Silk, *Massive Neutrinos and the Large Scale Structure of the Universe*, Phys.Rev.Lett. **45** (1980) 1980–1984

[237] S. Saito, M. Takada and A. Taruya, *Impact of massive neutrinos on nonlinear matter power spectrum*, Phys.Rev.Lett. **100** (2008) 191301, [arXiv:0801.0607]

[238] J. Brandbyge and S. Hannestad, *Grid Based Linear Neutrino Perturbations in Cosmological N-body Simulations*, JCAP **0905** (2009) 002, [arXiv:0812.3149]

[239] J. Brandbyge, S. Hannestad, T. Haugbolle and B. Thomsen, *The Effect of Thermal Neutrino Motion on the Non-linear Cosmological Matter Power Spectrum*, JCAP **0808** (2008) 020, [arXiv:0802.3700]

[240] M. Viel, M. G. Haehnelt and V. Springel, *The effect of neutrinos on the matter distribution as probed by the Intergalactic Medium*, JCAP **1006** (2010) 015, [arXiv:1003.2422]

[241] S. Saito, M. Takada and A. Taruya, *Neutrino mass constraint with the Sloan Digital Sky Survey power spectrum of luminous red galaxies and perturbation theory*, Phys.Rev. **D83** (2011) 043529, [arXiv:1006.4845]

[242] G.-B. Zhao, S. Saito, W. J. Percival, A. J. Ross, F. Montesano *et al.*, *The clustering of galaxies in the SDSS-III Baryon Oscillation Spectroscopic Survey: weighing the neutrino mass using the galaxy power spectrum of the CMASS sample*, [arXiv:1211.3741]

[243] S. Matsumoto and T. Moroi, *Studying Very Light Gravitino at the ILC*, Phys.Lett. **B701** (2011) 422–426, [arXiv:1104.3624]